X-ray study of the dark matter distribution in clusters of galaxies

（銀河団における暗黒物質分布のＸ線による研究）

片山　晴善

大阪大学　大学院理学研究科　宇宙地球科学専攻

大阪大学大学院理学研究科

X-ray study of the dark matter distribution in clusters of galaxies

Haruyoshi Katayama

Department of Earth and Space Science, Graduate School of Science,
Osaka University, Japan

March 6, 2003

Abstract

Clusters of galaxies are the largest gravitationally bound systems in the universe. Clusters contain not only galaxies and X-ray emitting hot gas, but also a huge amount of dark matter that, though not seen, is needed to bind the galaxies and hot gas in clusters. Although the origin of the dark matter is still an open question, the Cold Dark Matter (CDM) model has become a standard paradigm for explaining observations on the large-scale structure of the universe. The central region of clusters is one of the most important fields in which to examine the CDM model, and X-ray observation of hot gas is the most powerful tool to probe it.

We study the total gravitating mass distribution in the central region of 23 clusters of galaxies with *Chandra*. Using a new deprojection technique, we measure the temperature and gas density in the very central region of the clusters as a function of radius without assuming any particular models. Under the assumptions of hydrostatic equilibrium and spherical symmetry, we obtain the deprojected mass profiles of these clusters.

The mass profiles are nicely scalable with a characteristic radius (r_{200}) and mass (M_{200}) on the large scale of $r > 0.1r_{200}$. In contrast, the central ($r < 0.1r_{200}$) mass profiles have a large scatter even after the scaling. The core radii of the total mass density profiles are systematically larger than those of the gas density profiles, suggesting that gas is more concentrated than dark matter.

The inner slope α of the total mass density profile ($\rho(r) \propto r^{\alpha}$) is derived from the slope of the integrated mass profile. The values of the inner slope α at the radius of $0.02r_{200}$ (α_0) span a wide range from 0 to 2.3. For 6 out of 20 clusters, α_0 is lower than unity at a 90 % confidence level. CDM simulations predict that the inner slope α is in the range $1 < \alpha < 2$, which is inconsistent with our results.

Density profiles flatter than those expected from CDM simulations are also seen in galaxies, and are considered to represent a serious problem for the standard CDM model. We investigate three alternative theories that have been proposed to resolve this problem: Modified Newtonian Dynamics (MOND), the Self-Interacting Dark Matter (SIDM) model, and the Dynamical Friction (DF) model. The MOND fails to reproduce the observed temperature profile. The SIDM predicts that core radii comparable to those observed, but some of our results are not consistent with the SIDM predictions. On the other hand, the DF model accounts not only for the flat slope we observed but also for the negative correlation we obtained between the inner slope α_0 and the gas fraction within the framework of the CDM model.

Contents

List of Tables

List of Figures

Chapter 1

Introduction

The Cold Dark Matter (CDM) model has become the standard paradigm for explaining observations of the large-scale structure of the universe. In the CDM model, dark matter consists of non-baryonic, collisionless, cold particle. The properties of dark matter density profiles in the CDM model have been investigated extensively through numerous N-body simulations. Navarro, Frenk, & White (1997) (hereafter NFW) claimed that the dark matter density profiles in the CDM model are reasonably approximated by a universal form with singular behavior in its central region. Several N-body simulations predict that the density of dark matter increases as a power law $\rho(r) \propto r^{\alpha}$, with α in the range of 1 to 2, in the central region (e.g., $\alpha = 1$ by NFW; $\alpha = 1.5$ by Moore et al. (1998)). Measurements of the inner slope α of dark matter density profiles offer a powerful test of the CDM model.

The observational efforts in this respect have been in the form of dynamical studies of low surface brightness and dwarf galaxies. The observations obtained in those studies suggest the presence of a relatively flat core: $0 < \alpha < 1$ (e.g. Firmani et al. 2001). Gravitational lensing has made some observational constraints available at the scale of galaxy clusters. For instance, Sand, Treu, & Ellis (2002) showed that steep inner slopes ($\alpha > 1$) are ruled out at better than 99 %, for the lensing cluster MS2137-23. Although gravitational lensing studies provide a unique and important probe of dark matter profiles, they generally can be applied only to a limited sample of clusters that satisfy a specific lensing condition. X-ray observations of the density and temperature of a hot intracluster medium (ICM), on the other hand, probe the mass of a cluster of galaxies under the assumption of hydrostatic equilibrium. This could be a powerful tool to investigate dark matter profiles in the central regions of clusters. However, for previous X-ray satellites, such as *ROSAT* and *ASCA*, the detailed study of ICM temperature and density profiles at small scales has been difficult because of limitations on the performance of imaging or

spectroscopic instruments. The high spatial resolution imaging spectroscopy of *Chandra* enables the measurement of mass profiles in the very central regions of clusters of galaxies. Several groups have obtained X-ray constraints on the dark matter profiles of some clusters. These results are apparently consistent with the CDM model (e.g. David et al. 2001; Arabadjis, Bautz, & Garmire 2002). However, Ettori, Fabian, Allen, & Johnstone (2002) showed that the mass profile of A1795 flattens within 100 kpc. Systematic studies are thus required for a large sample of clusters.

In this thesis, we systematically study the mass profiles of 23 clusters of galaxies. In Chapter 2 we briefly review the current understanding of galaxy clusters. Chapter 3 describes the details of the *Chandra* X-ray observatory and its main instruments utilized in this analysis. Chapter 4 presents the sample selection and our deprojection technique. We show our main results (the temperature, density, and mass profile of each of the 23 sample clusters and the inner slope of each mass profile) in Chapter 5. In Chapter 6, we summarize our results and discuss the cause of the flattening of the mass profiles in the central region. We assume $\Omega_m = 1$, $\Omega_\lambda = 0$, and $H_0 = 50$ km s^{-1} Mpc^{-1} throughout this paper. Unless otherwise noted, all errors are 1σ (68.3 %) confidence intervals.

Chapter 2

Overview of Clusters of Galaxies

2.1 Clusters of galaxies

Clusters of galaxies contain about ten to thousands of galaxies within a radius of several Mpc, so they are usually observed as regions which show an enhancement of the surface galaxy number density over the empty field. Clusters of galaxies are the largest gravitationally bound systems in the universe, therefore they set clear constraints on the formation of the structure and composition of the universe.

Optically, clusters of galaxies are classified according to the number of member galaxies. Clusters containing many galaxies, up to a few thousands, are called rich, while those with fewer members, ten or so, are called poor. The most extensive and often cited catalogs of rich clusters are those of Abell (1958) and Zwicky et al. (1961–1968). They used the *Palomar Observatory Sky Survey* (POSS) plates for the northern sky and searched for the galaxy enhancements by eye, using somewhat different criteria to identify the clusters. Later, Abell's catalogue was extended to the southern sky by his co-workers (Abell, Corwin, & Olowin 1989). For example, Abell cataloged systems which contain more than 50 galaxies in the magnitude range of $[m_3,\ m_3 + 2]$ (where m_3 is the magnitude of the third brightest galaxy) within a circular region of radius $R_A = 1.7/z$ arc minutes (referred to as "Abell radius") as a cluster of galaxies. These large catalogs enabled us to make a statistical study of clusters of galaxies and large scale structures in the universe.

Clusters of galaxies often contain a particularly large, bright elliptical galaxy at the center. Dynamically, the heliocentric velocity of such a giant elliptical galaxy usually agrees with that of the cluster mean redshift. Therefore, it is believed to sit at the bottom of the cluster potential well. Such a galaxy is identified as a cD or D galaxy. cD galaxies are also embedded in an extended stellar halo of low surface brightness. About 20 % of all rich clusters have cD galaxies (Sarazin 1988).

Since galaxies in a cluster are bounded by the cluster's gravitational potential, their line-of-sight velocities exhibit a noticeable scatter around a mean recession velocity. This scatter, called the velocity dispersion σ, is typically in the order of several hundreds km/s in poor clusters, and exceeds 1000 km/s in rich clusters. The total mass of the cluster is estimated by the virial assumption, $GM/R_G \sim \sigma^2$, to be $M \sim 1.5\times10^{14}(\sigma/10^3 \text{ km/s})^2(R_G/1 \text{ Mpc})M_\odot$. It is an order of magnitude larger than the total mass of individual galaxies. This is known as the "missing mass" problem, and clearly indicates the necessity of non-luminous matter, namely dark matter. Indeed, the nature of dark matter has long been one of the fundamental unsolved problem in astrophysics.

2.2 X-ray observations of clusters of galaxies

2.2.1 X-ray emission from a cluster of galaxies

It was one of the most surprising discoveries in the history of X-ray astronomy that clusters of galaxies are powerful X-ray emitters. In the 1960's, X-ray emissions from clusters of galaxies were detected from the Virgo cluster, the Coma cluster (Byram, Chubb, & Friedman 1966), and the Perseus cluster (Fritz, Davidsen, Meekins, & Friedman 1971) using a sounding rocket. The launch of the first X-ray astronomy satellite *Uhuru* established that most clusters are generally bright X-ray sources with an X-ray luminosity of 10^{44}–10^{45} erg sec^{-1}. The X-ray emissions from clusters are extended, so that there are two alternative explanations; thermal bremsstrahlung from hot plasma, or inverse Compton of cosmic micro-wave background by high-energy electrons. In 1976, He-like Fe-K line emissions were detected from the Perseus cluster (Mitchell, Culhane, Davison, & Ives 1976), which revealed that X-ray emissions are emitted from a hot intracluster medium (ICM) with a temperature of 10^{7-8} K.

2.2.2 X-ray spectrum from the ICM

Since the ICM is low density ($\sim 10^{-3}$ cm^{-3}) and high temperature ($\sim 10^8$ K) plasma, the main radiation mechanism of the continuum emission is thermal bremsstrahlung (free-free radiation) and various atomic emission lines. The emissivity, which is the energy emitted from the unit volume during the unit time per unit frequency, is given by

$$\epsilon_\nu^{ff} = 6.8 \times 10^{-38} \sum_i Z_i^2 n_e n_i T_g^{-1/2} e^{-h\nu/kT_g} \overline{g_{ff}} \quad (\text{erg s}^{-1} \text{ cm}^{-3} \text{ Hz}^{-1}) \qquad (2.1)$$

where Z_i and n_i are the charge and number density of the iron i, n_e is the electron number density in cgs units, and $\overline{g_{ff}}$ is the Gaunt factor which is weakly dependent on

the temperature and frequency (Rybicki & Lightman 1979). The bolometric emissivity is then

$$\begin{aligned} \epsilon^{ff} &= \int_0^\infty \epsilon_\nu^{ff} d\nu \\ &\sim 1.4 \times 10^{-27} n_e n_i T_g^{-1/2} \sum_i Z_i^2 \overline{g_B} \ \ (\mathrm{erg\ s^{-1}\ cm^{-3}}) \end{aligned} \tag{2.2}$$

where the averaged Gaunt factor $\overline{g_B}$ is 1.1–1.5. The X-ray luminosity in a given bandpass, $\nu_1 \leq \nu \leq \nu_2$, is obtained by integrating Equation (2.1) over the frequency and the cluster volume;

$$L_X = \int dV \int_{\nu_1}^{\nu_2} \epsilon_\nu^{ff}\, d\nu. \tag{2.3}$$

Emission of atomic lines becomes significant when the ICM temperature falls below a few keV. Since the temperature of the ICM is of the same order as the K-shell ionization potentials of heavy elements such as O, Ne, Mg, Si, S, and Fe, these elements become mainly He/H-like ions and are completely ionized. These ions are collisionally excited, and then emit their resonance K-lines. In lower temperature clusters, in which Fe ions are not only He-like or H-like but also of a low ionization status, the spectrum exhibits resonance L-lines at $\sim$ 1 keV. The emission line spectra from the ionization equilibrium plasma have been calculated by various authors, e.g. Raymond & Smith (1977), Kaastra & Mewe (1993), and so on. In this thesis, we use the MEKAL code, which is based on the model calculations of Mewe, Lemen, & van den Oord (1986) and Kaastra & Mewe (1993) with Fe L calculations by Liedahl, Osterheld, & Goldstein (1995), in the XSPEC data analysis package.

2.3 Mass distribution in a cluster of galaxies

2.3.1 Hydrostatic equilibrium

Sound crossing time in the ICM is given by

$$t_{cross} \sim 6.6 \times 10^8\ yr\ (\frac{T_g}{10^8\ \mathrm{K}})(\frac{D}{\mathrm{Mpc}}). \tag{2.4}$$

Since this sound crossing time is considerably shorter than the age of the Universe, We can assume the ICM is in hydrostatic equilibrium. The force balance between the gas pressure P_g and the gravitational force, both acting on the ICM, is expressed as:

$$\nabla P_g = -\rho_g \nabla \phi \tag{2.5}$$

where ϕ is the gravitational potential and ρ_g is the gas density which can be written as $\rho_g = \mu n_g m_p$. Here n_g is the number density including electron and ions, $\mu(\sim 0.6)$ is the mean molecular weight, and m_p is the proton mass.

If we assume spherically symmetry, the above equation is reduced

$$\frac{dP_g}{dr} = -\mu n_g m_p \frac{d\phi}{dr}. \tag{2.6}$$

where r is the three dimensional radius. Because of the low density ($n_g < 10^{-2}$ cm^{-3}), the ICM can be treated as an ideal gas that follows the equation of state as

$$P_g = n_g k T_g. \tag{2.7}$$

Let $M(< r)$ denote the total gravitating mass within a radius r. Then combining Newton's equation

$$\frac{d\phi(r)}{dr} = \frac{GM(< r)}{r^2} \tag{2.8}$$

with 2.6, we can express $M(< r)$ as

$$M(< r) = -\frac{1}{\mu n_g(r) m_p} \frac{r^2}{G} \frac{dP_g(r)}{dr} = -\frac{kT_g(r)r}{\mu m_p G}\left(\frac{d\ln T_g(r)}{d\ln r} + \frac{d\ln n_g(r)}{d\ln r}\right). \tag{2.9}$$

Therefore, we can obtain the mass profile $M(< r)$ from the measurements of the density distribution $n_g(r)$ and the temperature distribution $T_g(r)$. Furthermore, knowledge of $n_g(r)$ readily allows us to estimate the ICM mass profile $M_g(r)$, which is written as

$$M_g(r) = \int_0^r 4\pi r'^2 \mu m_p n_g(r') dr'. \tag{2.10}$$

Thus, we can estimate the baryonic fraction as a function of r by incorporating optical data on the galaxy distribution.

2.3.2 King profile

We consider a cluster of galaxies to be a self-gravitational system consisting of collisionless particles of a single species, although a cluster is in fact a multi-component system consisting of at least galaxies, hot ICM, and dark matter. We assume the particles to have a mass m, a density profile $n(r)$, and an isotropic-uniform velocity dispersion of σ_r.

The hydro-static equation for the particles can be written as:

$$\frac{d\phi(r)}{dr} = -\sigma_r^2 \frac{d\ln n(r)}{dr} \tag{2.11}$$

which may be integrated and solved for n(r) as

$$n(r) = n_0 \exp[-\frac{\phi(r)}{\sigma_r^2}]. \tag{2.12}$$

We may combine this with the Poisson equation

$$\nabla^2\phi(r) = 4\pi G m n(r) \tag{2.13}$$

to determine $n(r)$ and $\phi(r)$, where G is the constant of gravity.

Although Equation (2.12) and Equation (2.13) do not give a trivial solution, King (1962) derived an approximate solution for $n(r)$ and $\phi(r)$ as

$$\phi(r) = -4\pi G n_0 m r_c^2 \frac{\ln(x + (1+x^2)^{(1/2)})}{x} \tag{2.14}$$

and

$$n(r) = n_0(1+x^2)^{(-3/2)}. \tag{2.15}$$

where r_c is a characteristic radius called the core radius, and $x \equiv r/r_c$. These two expression satisfy the Poisson equation (Equation (2.13)) exactly, while they only approximately satisfy the hydrostatic equilibrium equation (Equation (2.11)). The mass enclosed within a radius r in the King profile is given by

$$\begin{aligned} M_{\rm King}(<r) &= \int_0^r 4\pi r'^2 \rho(r) dr' \\ &= 4\pi\rho_0 r_c^3 (\ln[x + \sqrt{1+x^2}] - \frac{x}{\sqrt{1+x^2}}). \end{aligned} \tag{2.16}$$

2.3.3 Isothermal β model

We next consider the ICM density profile in the King potential. For simplicity we may approximate the ICM to be isothermal (T_g =constant). Then, as the hot ICM and the particles considered in the previous subsection must obey the same gravitational potential $\phi(r)$, we can equate Equation (2.9) and Equation (2.11) as

$$\frac{kT_g}{\mu m_p} \frac{d\ln n_g(r)}{dr} = \sigma_r^2 \frac{d\ln n(r)}{dr} \tag{2.17}$$

or

$$\frac{d\ln}{dr}[n_g(r) - n(r)^\beta] = 0 \tag{2.18}$$

with

$$\beta \equiv \frac{\mu m_p \sigma_r^2}{kT_g}. \tag{2.19}$$

Integrating Equation (2.18), we get

$$n_g(r) = n_{g0} \exp(-\beta[\phi(r) - \phi(0)]), \tag{2.20}$$

where n_{g0} is the central density of the ICM. Substituting Equation (2.14) for Equation (2.20), $n_g(r)$ can be approximately expressed only at small radii ($r < 6r_c$) as

$$n_g(r) = n_{g0}\ (1+x^2)^{-\frac{3}{2}\beta} \tag{2.21}$$

Equation (2.21) is called the β model.

When the ICM density is given by the β model, from Equation (2.9) we readily get

$$M(< r) = \frac{3kT_g\beta r}{\mu m_p G}\frac{x^2}{(1+x^2)}. \tag{2.22}$$

2.3.4 NFW density profile

Present cosmology predicts that dark matter consists of non-baryonic, collisionless particles, so called Cold Dark Matter (CDM). Recent high resolution N-body/hydrodynamical simulations in the CDM model have strongly suggested that the dark matter halos of cluster scales are described by a family of fairly universal density profiles. Navarro, Frenk, & White (1996, 1997, hereafter NFW) proposed a profile,

$$\rho_{NFW}(r) = \frac{\delta_c \rho_{\rm crit}}{(r/r_s)(1+r/r_s)^2} \tag{2.23}$$

where $\rho_{\rm crit} = 3H(z)^2/8\pi G$ is the critical density of the universe at a redshift z; r_s is a scaled radius; and δ_c is the concentration parameter, which can be expressed in terms of the concentration parameter ($c = r_{200}/r_s$, where r_{200} is the radius within which the mean halo density is $200\rho_{\rm crit}$) as

$$\delta_c = \frac{200}{3}\frac{c^3}{[\ln(1+c) - c/(1+c)]}. \tag{2.24}$$

The NFW density profile varies from $\rho_{NFW} \propto r^{-1}$ to $\rho_{NFW} \propto r^{-3}$. For a given cosmology, the concentration parameter decreases with an increase of the halo mass.

Although the density is diverse at the center, the mass enclosed within a radius r,

$$M_{NFW}(< r) = 4\pi\delta_c\ \rho_{\rm crit}\ r_s^3\ [\ln(1+x) + \frac{x}{1+x}] \tag{2.25}$$

converges to 0 as $r \rightarrow 0$.

2.3.5 Gas distribution in the NFW density profile

We can analytically calculate properties of an isothermal gas sphere hydrostatically confined in a NFW halo given by Equation (2.23). Assuming that the masses of gas and galaxies are negligibly small compared to the dark matter, the ICM density can be derived as

$$\rho_{gas}(r) = \rho_{gas0}\ \exp[-B(1 - \frac{\ln(1+x)}{x})] \tag{2.26}$$

where B is a constant defined by

$$B \equiv \frac{4\pi G\mu m_p \delta_c \rho_{\rm crit} r_s^2}{kT_g} \tag{2.27}$$

(Makino, Sasaki, & Suto 1998). Then the mass of the gas within a radius r is given by

$$M_{gas}(< r) = 4\pi\rho_{gas}(0)e^{-B}r_s^3 \int_0^x x^2(1+x)^{B/x}dx. \tag{2.28}$$

2.3.6 Other profiles

Several CDM simulations result in density profiles, for masses in the range $10^7 M_\odot$ – $10^{15} M_\odot$, that agree with a density profile of the general form,

$$\rho(r) = \frac{\rho_0}{(r/r_s)^\alpha[1+(r/r_s)^\beta]^{(\gamma-\alpha)/\beta}} \tag{2.29}$$

where ρ_0 is the characteristic density of the halo, and r_s is its characteristic scale radius. For example, the King profile and the NFW profile correspond to $(\alpha, \beta, \gamma) = (0, 2, 3)$ and $(\alpha, \beta, \gamma) = (1, 1, 3)$, respectively. Here, we show other profiles proposed by some authors.

Moore profile

Higher resolution simulations followed the NFW simulation found a somewhat steeper profile. Moore et al. (1998) and Moore et al. (1999) showed that the density profile can be described $\rho(r) \propto [(r/r_s)^{1.5}(1+(r/r_s)^{1.5})]^{-1}$, which corresponds to $(\alpha, \beta, \gamma) = (1.5, 1.5, 3)$ (in Moore et al. (1998), $\alpha = 1.4$). A similar steeper profile is also reported by other authors (Fukushige & Makino 1997; Ghigna et al. 2000; Fukushige & Makino 2001).

Hernquist profile

Hernquist (1990) derived the analytic mass profile for elliptical galaxies. This density profile is described as $\rho(r) \propto [(r/r_s)(1+(r/r_s))^3]^{-1}$, which corresponding to $(\alpha, \beta, \gamma) = (1, 1, 4)$. Hernquist profile decreases $\rho(r) \propto r^{-4}$ in the outer regions.

Burkert profile

Burkert (1995) proposed empirical density profile from the observed mass profiles of dwarf spiral galaxies. The Burkert profile is given by

$$\rho_{burkert}(r) = \frac{\rho_0 r_s^3}{(r+r_s)(r^2+r_s^2)} \tag{2.30}$$

where ρ_0 and r_s represent the central density and a scale radius, respectively. As well as the King profile, the Burkert profile has a core and is flat in the central region.

In Figure 2.1, all dark matter density profiles shown in this section are plotted in arbitrary units. As shown in Figure 2.1, the main difference of these profiles is the inner slope α. Most CDM simulations predict that α is in the range from 1 to 2.

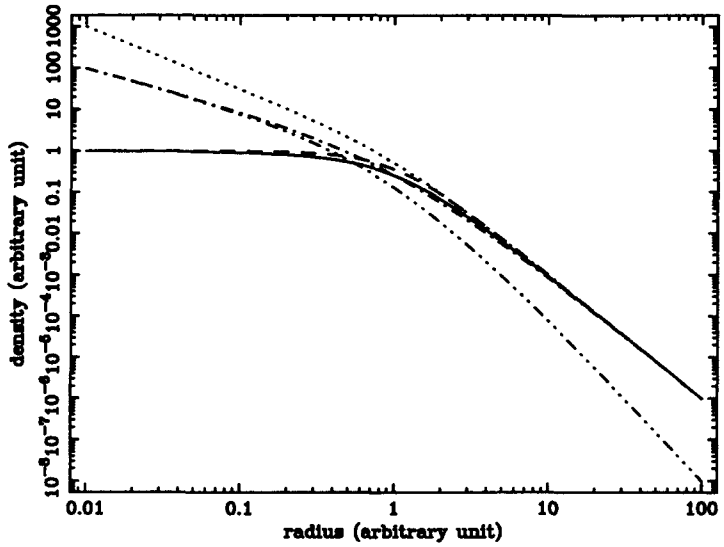

Figure 2.1: Dark matter density profiles shown in this section. The solid line, dashed line, dash-dotted line, dotted line, and dash-three-dotted line represent the King profile, the NFW profile, the Moore profile, the Hernquist profile and the Burkert profile, respectively

2.4 Cooling flow

2.4.1 Cooling flow studies before *Chandra* and *XMM-Newton*

Some clusters of galaxies show a strongly peaked emission exceeding the conventional β profile in the central several tens kpc. The presence of such a central excess X-ray emission has usually been interpreted as evidence of cooling flow at the cluster center. The basic idea of the cooling flow is straightforward: the cooling time of the ICM near the cluster center is much less than the Hubble time H_0^{-1}. As the gas cools off, the reduction of the pressure would cause the overlying gas to drop slowly if no extra heat source is present.

The mass deposition rate, $\dot{M}$ can be estimated from the imaging observation if we assume that the central excess emission arises from cooled material accreting toward the center. We assume spherical symmetry and a steady state flow. If the flow speed v is much slower than the sound speed of the ICM, the ICM is approximately in hydrostatic equilibrium. For the mass accretion rate $\dot{M}$, the mass conservation law is written as

$$\dot{M} = 4\pi r^2 \rho_g v. \tag{2.31}$$

The hydrostatic equilibrium can be written in Equation (2.6). The energy conservation law (The Beroulli theorem) is

$$\rho_g v \frac{d}{dr}\left(\frac{v^2}{2} + \frac{P_g}{\rho_g} + \frac{3}{2}\frac{kT_g}{\mu m_p} + \phi\right) = n_e n_p \Lambda(T_g) \tag{2.32}$$

Because the flow speed v is much slower than the sound speed of the ICM ($\sim \sqrt{P/\rho_g}$), we can neglect the term $v^2/2$ in Equation (2.32). If we assume constant pressure of the ICM, we get from Equation (2.6)

$$\frac{d\phi}{dr} = 0. \tag{2.33}$$

Therefore, using Equation (2.31) and Equation (2.32) becomes

$$\frac{\dot{M}}{4\pi r^2}\frac{5k}{2\mu m_p}\frac{dT_g}{dr} = n_e n_p \Lambda(T_g). \tag{2.34}$$

The ICM between r and $r + dr$, which has a temperature in the range T_g to $T_g + dT_g$, emits a luminosity of excess component $dL_{\rm excess}$:

$$\begin{aligned} dL_{\rm excess} &= n_e n_p \Lambda(T_g) \times 4\pi r^2 dr \\ &= \frac{5}{2}\frac{\dot{M}}{\mu m_p} k dT_g \end{aligned} \tag{2.35}$$

for steady-state isobaric cooling flow, where μ and m_p are the mean atomic weight and proton mass, respectively. The $\dot{M}$ has been estimated for hundreds of clusters, White, Jones, & Forman (1997) compiled *Einstein* data of 201 clusters and revealed that 63^{+12}_{-15}% of their sample had a cooling flow whose mass deposition rate was up to $\dot{M} \sim 740 M_\odot$ year^{-1} . *ROSAT* observation revealed more massive cooling flows (Allen 2000).

A significant advance in the understanding of cool gas has been brought by *ASCA*. *ASCA* has enabled a wide energy (0.5–10 keV) band, moderately high resolution ($E/\Delta E \sim$ 45 at 5.9 keV) spectroscopic observations and has revealed that at least two temperature components are needed to explain the spectra in cooling flow clusters. The observed spectra for several clusters suggest that the cool gas has a temperature of typically 1 keV, and luminosity of the cool gas is estimated to be less than 10 % of the total X-ray luminosity of the cluster (Fukazawa et al. 1994).

Ikebe et al. (1995) carefully analyzed *ASCA* data of the Centaurus cluster, which is a well studied cooling flow cluster, and showed that its X-ray spectra were expressed by the two temperature Raymond-Smith model. The temperature of each component stays almost constant from the center to a radius of 40′, not showing a gradual decrease. The fraction of emission measure of the cool component is larger in the inner $\sim 2'$ region ($\sim$ 50%) and then rapidly decreases to 10 % in the outer region. The latter result indicates that the hot component of the ICM is still present at the very center of the cluster. The continuous decrease of the temperature toward the cluster center is seen in a single temperature fitting for *ROSAT*/PSPC spectrum should be the result of the relative amount of two temperature components and it seems natural to interpret that the ICM in the Centaurus cluster is really two-phase and the cool component is rather restricted within the center.

2.4.2 Current status of cooling flow studies

New X-ray observations with *Chandra* and *XMM-Newton* have revised the conventional picture of cooling flow. The high resolution spectroscopy with *XMM-Newton* has shown a lack of emission lines from gas cooling below 1–2 keV (e.g. A1795 (Tamura et al. 2001), A1835 (Peterson et al. 2001)). The cooling rates found by *Chandra* and *XMM-Newton* are much smaller than previously reported.

These results suggest a heating mechanism is required in the central regions of cooling flow clusters. One of the heating source candidates is a central radio source. The high resolution X-ray image with *Chandra* has revealed a remarkable structure in the cores of cooling flow clusters (e.g. Hydra A (McNamara et al. 2000), the Perseus cluster (Fabian et al. 2000), the Centaurus cluster (Sanders & Fabian 2002; Taylor, Fabian, & Allen 2002)). X-ray cavities in the central region of cooling flow clusters (see Figure 2.2) is clear evidence of the interactions between the ICM and the powerful radio source. Using simulations of jets expanding into the ICM, Heinz, Reynolds, & Begelman (1998) argued that the cavities were caused by strong shock waves generated by relativistic jets. However, a problem with this scenario is the large energy input required (Fabian et al. 2001). An alternative heating source is a magnetic field near the cD galaxies. Makishima et al. (2001) suggested that motions of the member galaxies cause magnetohydrodynamics (MHD) turbulence and frequent magnetic reconnection as suggested by Norman & Meiksin (1996).

Although cooling flow studies with *Chandra* and *XMM-Newton* are still in progress, and several interpretations still contain some problems, further investigation with high resolution spectroscopy with *ASTRO-EII* should clear this cooling flow problem.

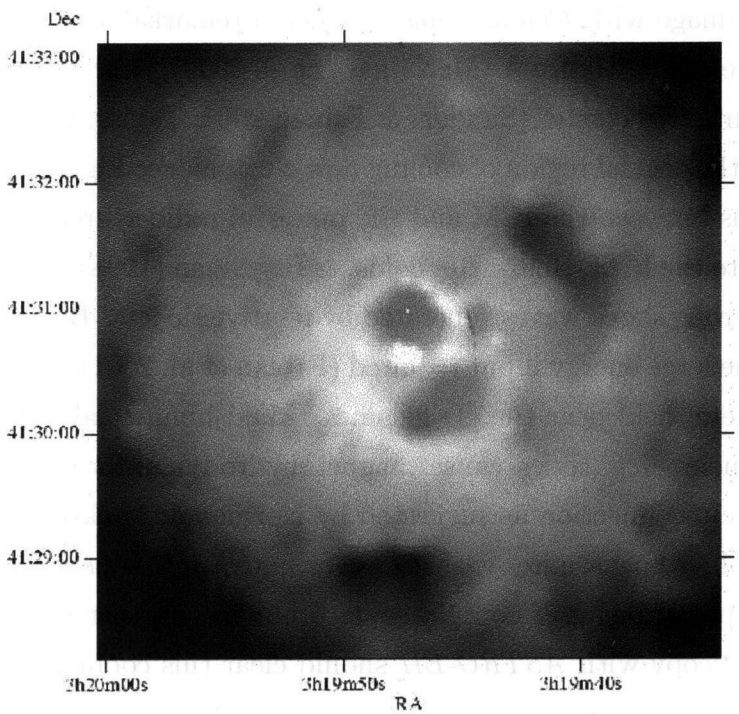

Figure 2.2: Adaptively smoothed 0.5–7 keV image of the core of the Perseus cluster observed with *Chandra* (Fabian et al. 2000). The X-ray cavities in the emission associated with the inner radio lobes of 3C84 are clearly seen.

Chapter 3

The *Chandra* X-ray Observatory

This chapter gives a brief description of the *Chandra* X-ray observatory, and the on-board instruments utilized in our observations, the High Resolution Mirror Assembly (HRMA) and the Advanced CCD Imaging Spectrometer (ACIS). It begins with an overview of the *Chandra* mission. In §3.2 and §3.3, we describe the characteristics of the HRMA and the ACIS, respectively. More details can be found in *Chandra* Proposers' Observatory Guide 2002[1].

3.1 *Chandra* X-ray Observatory

3.1.1 Mission overview

The *Chandra* X-ray Observatory (Weisskopf et al. 2000), named in honor of Dr. Subrahmanyan Chandrasekhar, is the X-ray component of *NASA*'s four Great Observatories, including the Hubble Space Telescope, the Compton Gamma-Ray Observatory, and the Space Infra-Red Telescope Facility. *Chandra* was launched and deployed by *NASA*'s Space Shuttle *Columbia* on July 23, 1999.

. *Chandra* was launched into an elliptical orbit, as of November 1999 the apogee was ~138,800 km and the perigee was ~10,100 km, allowing for uninterrupted observing intervals of more than 170 ks due to its orbital period of 63.5 hours. An outline drawing of *Chandra* is shown in Figure 3.1. The dry weight and size are approximately 4790 kg, 14 m long × and 19.5 m wide (solar arrays deployed), respectively.

[1]http://asc.harvard.edu/udocs/docs/POG/MPOG/index.html

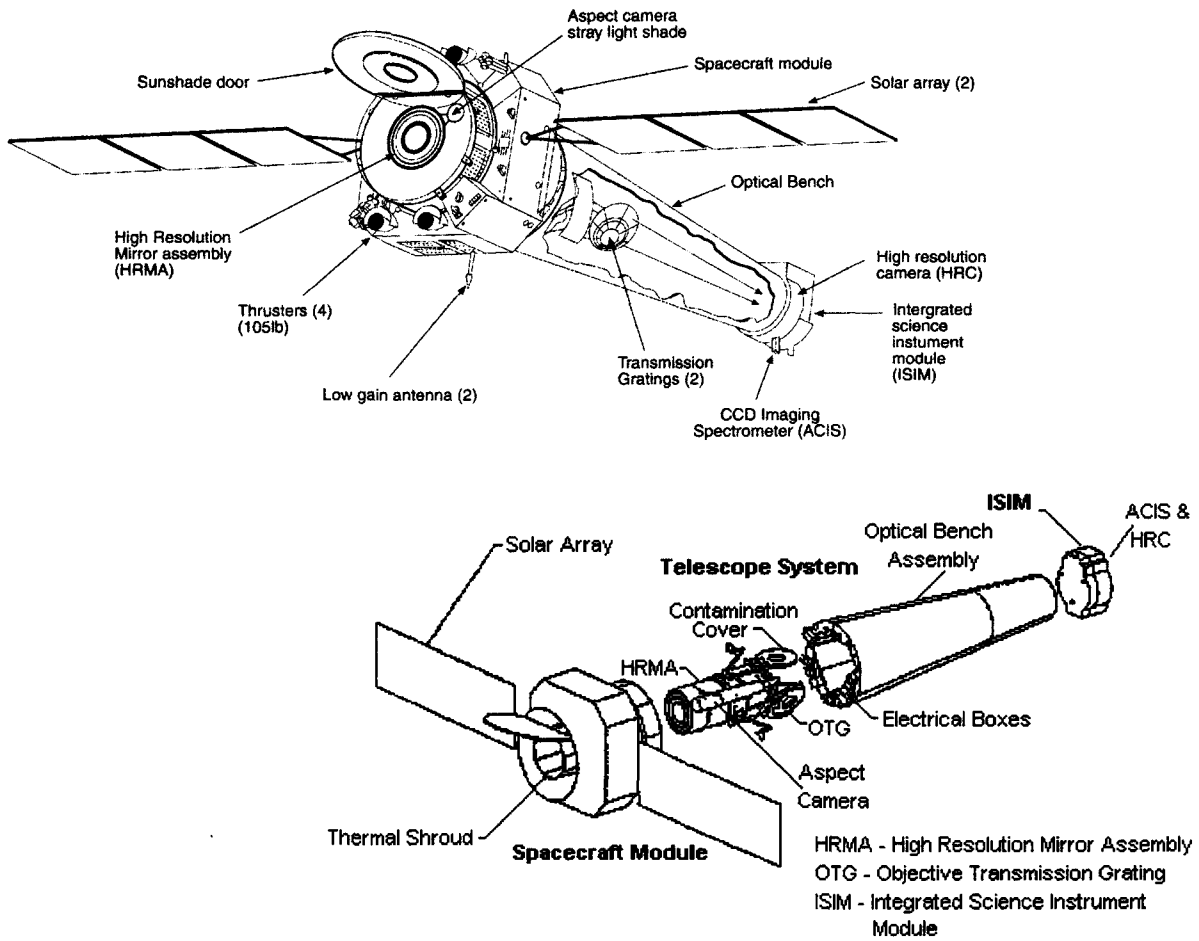

Figure 3.1: A schematic (top) and expanded (bottom) view of *Chandra* X-ray observatory. §3.1.2 gives the descriptions of each of the scientific instruments.

3.1.2 Scientific instruments

Chandra's X-ray telescope consists of four pairs of concentric mirrors, denoted as the High Resolution Mirror Assembly (HRMA; van Speybroeck et al. 1997; Weisskopf & O'dell 1997; Zhao, Cohen, & van Speybroeck 1997). Located at the aft of the HRMA are two objective transmission gratings (OTG), the High Energy Transmission Grating and (HETG; Canizares er al. 2001) the Low Energy Transmission Grating (LETG; Brinkman et al. 2000). On the focal plane, there are two sets of detectors, one being the imaging spectroscopic CCD arrays, the Advanced CCD Imaging Spectrometer (ACIS; Garmire et al. 2001), and the other being the imaging microchannel plate, the High Resolution Camera (HRC; Murray et al. 1998). Both detectors are housed in the scientific instrumental module (SIM). The SIM is a movable bench to adjust the detector position.

The HRMA's unprecedented spatial resolution, with a half-power diameter (HPD) of the point spread function (PSF) of $< 0\farcs5$, characterizes the *Chandra* mission, representing an order-of-magnitude advance over previous X-ray astronomy missions.

The use of the OTG is selective among HETG, LETG, or none. The high spectral resolving power (i.e. $E/\Delta E$ up to 1000) is suitable for studies of plasma through emission lines, absorption lines and absorption edges. Since the OTG was developed for point sources, observations of extended sources, especially in cases of sources with spatial-spectral variations, adds complexity.

Two focal plane detectors are distinguished by their unique capabilities. The HRC was designed to have better spatial resolution, $0\farcs132$ pixel size (span of electronic readout), than the ACIS whose CCD pixel size is $0\farcs492$. The time resolution of the HRC is 16 μsec, while that of the ACIS is limited by the frame time, 3.2 seconds is nominal. On the other hand, the ACIS offers much better spectral resolution and higher detective efficiency than the HRC. Only one device may be selected at a time.

3.2 High Resolution Mirror Assembly (HRMA)

3.2.1 Overview

The HRMA are four pairs of concentric thin-walled, grazing-incidence Wolter Type-I mirrors. Given the tendency of X-rays to either penetrate or be absorbed by materials, the most efficient optical configuration for X-ray imaging consists of grazing incidence optics where X-ray photons experience total internal reflection. The Wolter Type-I mirror consists of a primary paraboloid and a secondary hyperboloid surface to reduce aberrations. Figure 3.2 illustrates the geometry of the Wolter Type-I optics as it pertains to the

HRMA.

The mirror pair diameters range from 0.65 to 1.23 meters. The focal point is 10 meters behind the HRMA center separating the paraboloid and hyperboloid mirrors. Some other characteristics are given in Table 3.1.

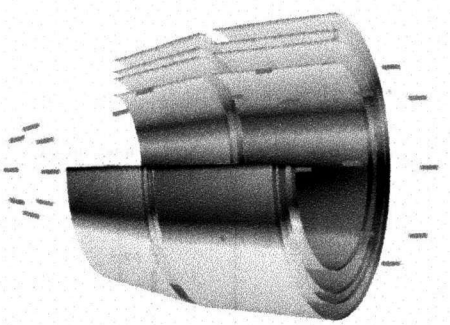

Figure 3.2: The geometry of the Wolter Type-I optics as it pertains to the HRMA.

Table 3.1: Design parameters of the HRMA.

Mirror Substrate	Zerodur[a]
	(23.6, 18.3, 16.5, and 15.9 mm[b])
Mirror Surface	Iridium (330 Å)
Mirror Length (primary or secondary)	0.84 m
(pre-collimator to post-collimator)	2.76 m
Mirror Diameter	1.23, 0.99, 0.87, 0.65 m[b]
Mirror Weight	1484 kg
Focal Length	10.066 ± 0.002 m
Unobscured clear aperture	1145 cm^2
Grazing Angle Range	52, 42, 37, and 27 arcminutes[b]
Field of View (Ghost-free)	30 arcminuts diameter

[a] glass ceramic made by Schott in Germany

[b] from outer to inner

3.2.2 Effective area

Since the X-ray reflectivity depends on both the energy and grazing angle, the HRMA throughput varies with the X-ray energy and source off-axis angle. Figure 3.3 shows the dependence of effective area on the energy and off-axis angle. The effects of both the energy variation and off-axis vignetting are strongly coupled.

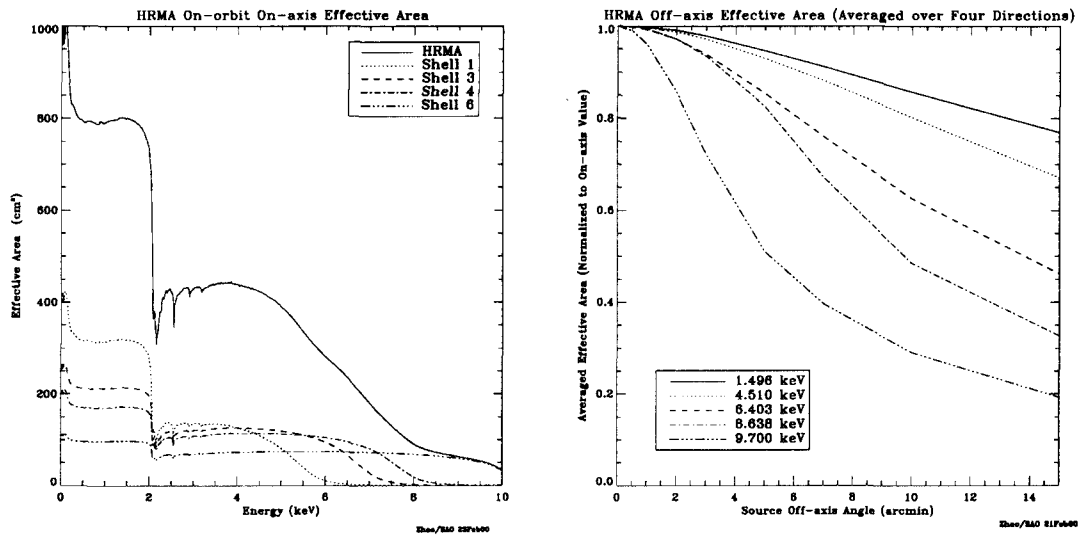

Figure 3.3: **Left**: The HRMA effective area versus energy. The solid line is the total effective area and the other four lines indicate the contributions from each mirror. The outer mirror pair is number 1, and, progressing inwards, 3, 4, and 6. (The original design had six mirror pairs; numbers 2 and 5 were eliminated.) The outer mirror has a larger effective area of soft energies resulting from its larger diameter, while the inner mirror is responsible at hard energies resulting from its small grazing angle. The structure near 2 keV is due to the iridium M-edge. **Right**: The HRMA effective area versus off-axis angle, averaged over the 4 mirror pairs and azimuth. The curves show the off-axis behavior at four selected energies, with the values being normalized to the on-axis value at that energy. Note that the effective area decreases sharply at large off-axis angles and its slope steepens as a function of energy.

Figure 3.3 are based upon the raytrace simulation. The deviation between the effective area predicted for the ground calibration using the simulation and the actual measurement are less than a few percent. A comparison of data from the ground calibration with those obtained in orbit was performed via a Flux Contamination Monitor (FCM), a system of 16 radioactive calibration sources that were exposed immediately prior to opening the sun-shade door. The FCM is installed in the contamination cover of the HRMA (Figure 3.1). No change in performance was detected.

3.2.3 Point Spread Function (PSF)

As with the effective area, the point spread function (PSF) also depends upon the energy and off-axis angle, due to larger X-ray scattering as the X-ray energy increases and mirror aberrations, respectively. Figure 3.4 shows these dependences. To demonstrate these dependencies, Figure 3.4 shows the encircled energy fraction (the two-dimensional integral of the PSF) as a function of radius from the image center.

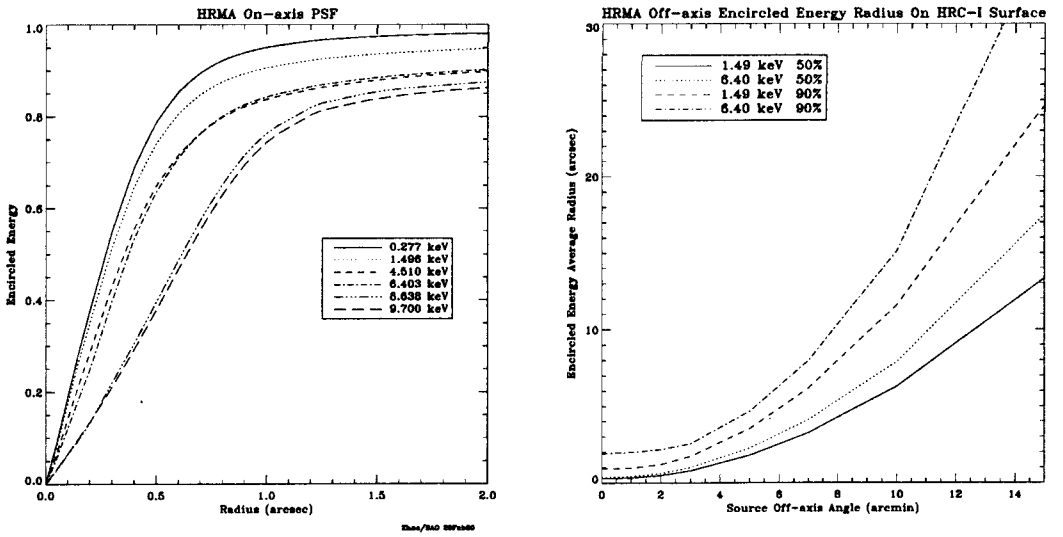

Figure 3.4: **Left**: The encircled energy fraction as a function of radius from the image center. Shown is the behavior for an on-axis point-source over a range of selected X-ray energies. The curves are the combined response of the four mirror pairs. At high energies, the encircled energy fraction decreases due to larger scattering. **Right**: The 50% and 90% encircled energy radius at 1.5 and 6.4 keV as a function of off-axis angle. The encircled energy radius increases as a function of the increasing off-axis angle, with higher energies requiring a larger radius.

The PSF is sharply peaked and has a low-level, long tail wing (Jerius et al. 2000). On-axis, the normalized flux levels of wing (arcsec^{-2}s^{-1} / s^{-1}) are approximately 10^{-5} and 10^{-7} at 10 and 100 arcsec from the image center, respectively. Thus these low-level

wings are only a concern for bright sources, and especially those with hard spectra, when there are enough counts to adequately fill the PSF.

3.3 Advanced CCD Imaging Spectrometer (ACIS)

3.3.1 Overview

The ACIS contains ten MIT Lincoln Laboratory CCID17 charge coupled devices (CCDs). The CCID17 is a three-phase, frame transfer imager (Burke et al. 1997). Four of the ten chips are abutted into a 2×2 array (ACIS-I) used for imaging, and the other six chips are arranged in a 1×6 array (ACIS-S) used either for imaging or as a grating readout. The configuration of ACIS chips are shown in Figure 3.5. Two of ACIS-S CCDs are back-illuminated (BI), while the rest of ACIS-S and all of ACIS-I are front-illuminated (FI). There are two choices for the on-axis position of the HRMA, one is ACIS-S3 and another is ACIS-I3. Due to the telemetry limits, only six chips can be activated in observation. There are particular observational advantages to using the ACIS-I and ACIS-S. ACIS-I has a larger field of view ($17' \times 17'$) and lower background. Since the BI chip has superior low-energy quantum efficiency and is positioned at the nominal aim point of ACIS-S, ACIS-S has the benefit to observe a target whose spectrum is dominated by low energy emission. Other characteristics are summarized in Table 3.2.

Table 3.2: Design parameters of the ACIS.

Architecture	3-phase, frame-transfer, 3-side-abuttable
CCD Format	1024×1024 pixels
Pixel Size	24.0 microns (0.492 ± 0.0001 arcsec)
Array Size	16.9×16.9 arcmin (ACIS-I)
	8.3×50.6 arcmin (ACIS-S)
Nominal Frame Time	3.2 sec (full frame)
Operating Temperature	-120 degrees
Readout Noise (system)	2-3 e^- RMS
Charge Transfer Inefficiency	$< 3 \times 10^{-6}$ per pixel transfer (FI)
	$<$ 1-3 $\times 10^{-5}$ per pixel transfer (BI)
Mean Dark Current	$< 5 \times 10^{-2} e^- s^{-1}$pixel^{-1}

After the contamination cover was opened and the ACIS was exposed, the charge transfer inefficiency (CTI) of the FI CCDs increased in a few passages through the radiation belts which is considered due to the radiation damage by low energy protons (see

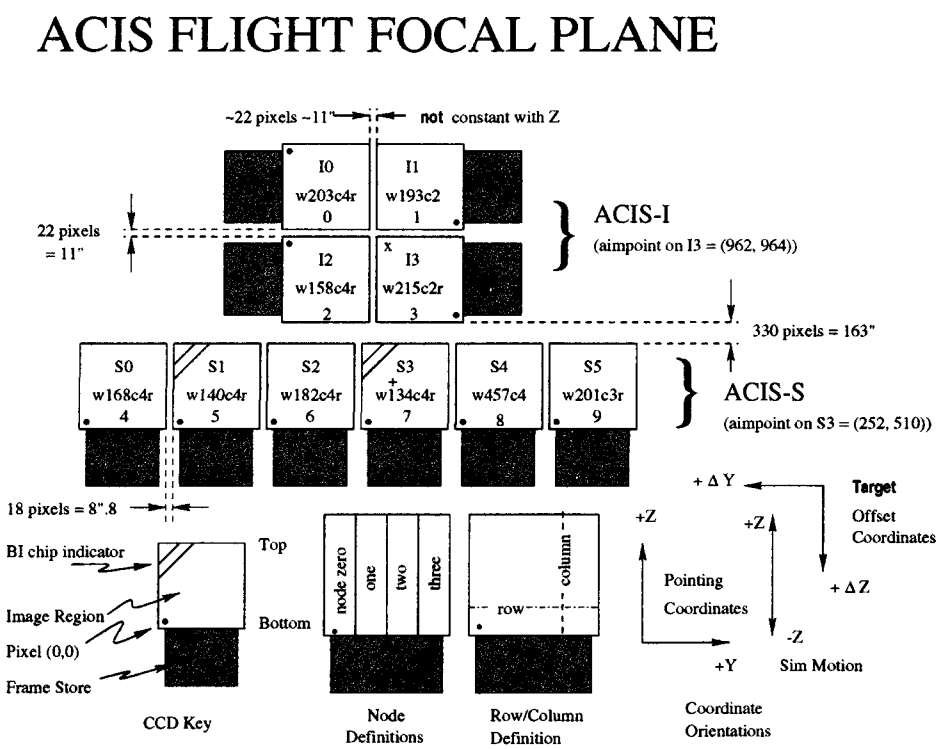

Figure 3.5: A schematic drawing of the ACIS configuration. The view is along the optical axis, from the source towards the detectors. A guide to the terminology is given at the bottom. The nominal aim points are plotted as × and + on I3 and S3, respectively. The node numbering scheme is illustrated in the lower center. Since ACIS-S chips are also used for readout of the HETG observation, the arrangement is along the direction of dispersion.

§3.3.6). Since the ACIS is no longer left at the focal plane position during the radiation belt passage, no further degradation in performance has been encountered. The BI CCDs were almost unaffected, because the buried channels of the BI CCDs face in the direction opposite to the HRMA.

3.3.2 Basic principle of event detection

A CCD is a pixel array of Metal-Oxide Semiconductor capacitors composed primarily of silicon. Photoelectric absorption of an incident X-ray photon in silicon results in the liberation of a proportional number of electrons (an average of one electron-hole pair for each ~3.71 eV of photon energy absorbed; Canali et al. (1972)). The charge cloud is drawn toward the electrode along the electric field and collected in a potential well. After exposure for a fixed amount of time (full frame ~3.2 sec), the charge is then transferred from pixel to pixel into the frame store (~40 msec total).

Since the charge cloud size (a few μm) is smaller than the pixel size (24μm) (Tsunemi et al. 1999) and does not split into more than four pixels, an "event" is identified within 3×3 pixel island centered on the local charge maximum. First, the on-board processor examines every pixel in the full CCD image and selects pixels as events with bias-subtracted values that both exceed the event threshold and are greater than all of the touching or neighboring pixels (i.e., a local maximum). Next, the surrounding 3×3 neighboring pixels are then compared to the bias-subtracted split-event threshold. Those that are above the threshold establish the pixel pattern. On the basis of this pattern, the event is assigned a "grade". The grade information is helpful in distinguishing between X-ray events and non-X-ray events. This way to recognize events using grades was originally adopted by *ASCA* satellite. Whole event patterns are divided into eight *ASCA* grades. The ACIS follows the *ASCA* grade standard, but the ACIS has its own grade, where events are assigned to one of 256 ACIS grades. The calibration of the ACIS is based on a specific subset of the grades comprising the *ASCA* grade 0, 2, 3, 4, and 6, because it is likely that other grades do not originate from a single X-ray photon. Figure 3.6 and Table 3.3 provide a definition of the *ASCA* grade set.

3.3.3 Telemetry formats

There are three telemetry formats available. The number of bits per event depends on which operating mode and which telemetry format is selected. The number of bits per event determines the threshold of event rate at which the telemetry will saturate and data will be lost until the onboard-buffer empties. The formats are described in the following

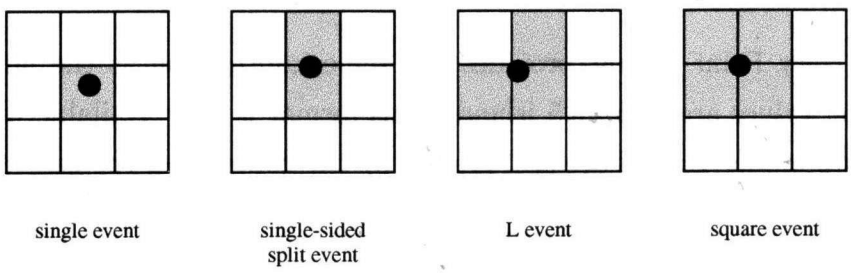

Figure 3.6: The X-ray event pattern of the CCDs.

Table 3.3: definition of the ASCA grade set.

grade	name	split pattern
0	single	center
1	single+	center (+ detouched corner(s))
2	vertical split	center + top or bottom (+ detouched corner(s))
3	left split	center + left (+ detouched corner(s))
4	right split	center + right (+ detouched corner(s))
5	single-sided+ (+ detouched corner(s))	single-sided split + touched corner pixel(s)
6	L or square	L or square split (+ detouched corner(s))
7	Others	all others

paragraphs.

Faint Faint format provides the event position in detector coordinates, an arrival time, an event amplitude, and the contents of the 3×3 island that characterizes the event grade.

Very Faint Very Faint format provides the same information as the faint format but the pixel values are in a 5×5 island. This format is only available with the Timed Exposure mode. Events are still graded by the contents of the central 3×3 island.

Graded Graded format provides event position in detector coordinates, an event amplitude, the arrival time, and the event grade.

3.3.4 Dither

The spacecraft is dithered during observations to provide some exposure in the gaps between the CCDs and to smooth out pixel-to-pixel variations in the response. The dither pattern is a Lissajous figure and spans 16 arcsec peak to peak. The sub-pixel offsets due to dither motion results in an image with higher spatial resolution compared to one without dither.

3.3.5 Combined HRMA/ACIS spatial resolution

The HPD of the PSF of the *Chandra* mirror is comparable to the pixel size of the CCD of the ACIS, and thus the spatial resolution for on-axis imaging is limited by ACIS. Furthermore, since chip coordinate values are randomized uniformly by ± 0.5 pixel size when they are transformed to sky coordinate values, this can also affect the overall spatial resolution. Figure 3.7 shows an on-orbit encircled energy fraction as a function of radius from the image center. A comparison with Figure 3.4 shows such effects.

3.3.6 Energy resolution

The energy resolution of an X-ray CCD is characterized by three factors: statistical fluctuation in the number of primary electrons, the thermal noise, and the pre-amplifier read-out noise. The thermal noise is negligible at the ACIS operating temperature of −120°C. Thus, the energy resolution can be expressed as following,

$$\Delta E(\mathrm{FWHM}) = 3.71\sqrt{8\ln 2}\sqrt{\sigma_N^2 + F \times \frac{E}{W}} \qquad (\mathrm{eV}) \qquad (3.1)$$

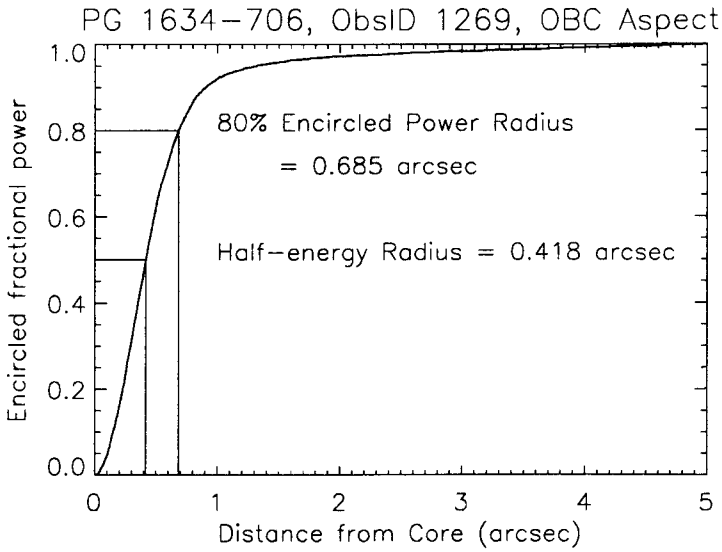

Figure 3.7: The on-orbit encircled energy fraction as a function of radius for an ACIS observation of point source PG1634-706. The effective energy is 1keV.

Here σ_N is equivalent pre-amplifier read-out noise (in electrons rms), F is a Fano factor which is 0.135 for crystalline silicon, E is the energy of the incident X-ray photon, and W is the mean ionization energy of silicon, 3.71 eV/e^- at the CCD operating temperature of −120°C (Canali et al. 1972).

Figure 3.8 shows the pre-launch energy resolution as a function of energy. The BI CCDs exhibited poorer resolution. Due to the radiation damage, the energy resolution of the FI CCDs has become a function of the row number, being near pre-launch values close to the frame store region and substantially degraded in the farthest row, while the BI CCDs were not impacted. Such effects are illustrated in Figure 3.9.

3.3.7 Quantum efficiency and combined HRMA/ACIS effective area

The quantum efficiencies for the ACIS CCDs for the standard grade set (*ASCA* grade .02346), including the optical blocking filters which are placed over the CCDs between the chips and the HRMA, are shown in Figure 3.10. In the case of the FI CCDs, the gate structure faces in the direction of the HRMA and functions as a "dead" layer which limits the quantum efficiency at low energies. Since the BI CCDs' gate structures are mounted in the direction opposite to the HRMA, the BI is more sensitive at low energies than FI. In contrast, FI is sensitive at high energies because of its thicker depletion region versus that of the BI. The combined HRMA/ACIS on-axis effective areas are shown in Figure

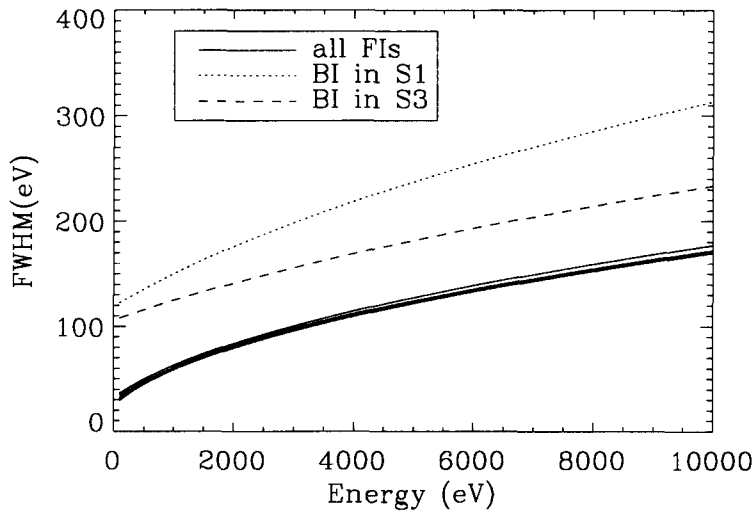

Figure 3.8: The ACIS pre-launch energy resolution as a function of energy. The FI CCDs approached the theoretical limit for the energy resolution at almost all energies, while the BI CCDs exhibited poorer resolution.

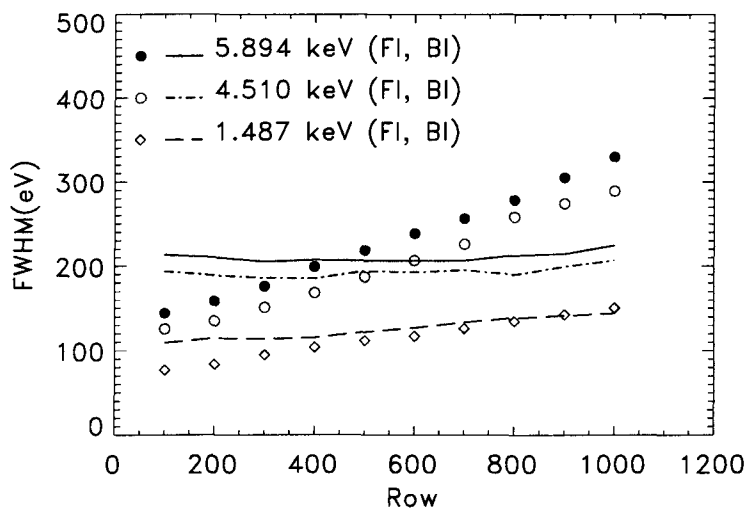

Figure 3.9: The energy resolution of S3 and I3 as a function of row number. The row number dependency of I3's energy resolution is illustrated.

3.11.

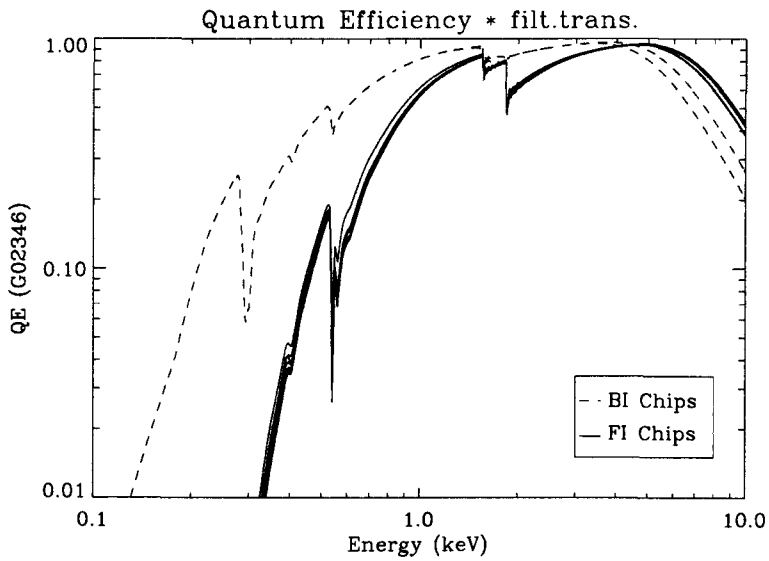

Figure 3.10: The quantum efficiency, convolved with the transmission of the appropriate optical blocking filter of the FI CCDs (from a row nearest the readout) and the two BI CCDs as a function of energy. The FI and BI CCDs have higher efficiency at high and low energies, respectively.

3.3.8 On-orbit background of ACIS

The ACIS background consists of a relatively soft Cosmic X-ray Background (CXB) contribution and cosmic ray-induced events with a hard spectrum. There is an occasional strong third component producing background flares. The flares are thought to be caused by proton scatter through the mirror system. During the flare, the count rate of the background increases by two orders of magnitude. Figure 3.12 shows a comparison of two background spectra during the flaring and quiescent period. Since the nature of the flaring component is still unknown, the quiescent periods are used for the analysis, especially for the diffuse source.

Figure 3.13 shows the quiescent background spectrum for an FI CCD (S2) (left) and a BI CCD (S3)(right). The cosmic ray component dominates above 5 keV. The background count rate of the BI is about three times higher than that of the FI in 0.3–10 keV. This is due to the difference of the depletion layer of the BI and FI. The charge cloud generated by particles hit into the FI largely diffracts until it reaches the electrode. Most of these events end up as *ASCA* grade 7, and are thus rejected with high efficiency. On the other hand, for the BI, the charge cloud does not diffract largely in comparison with the FI,

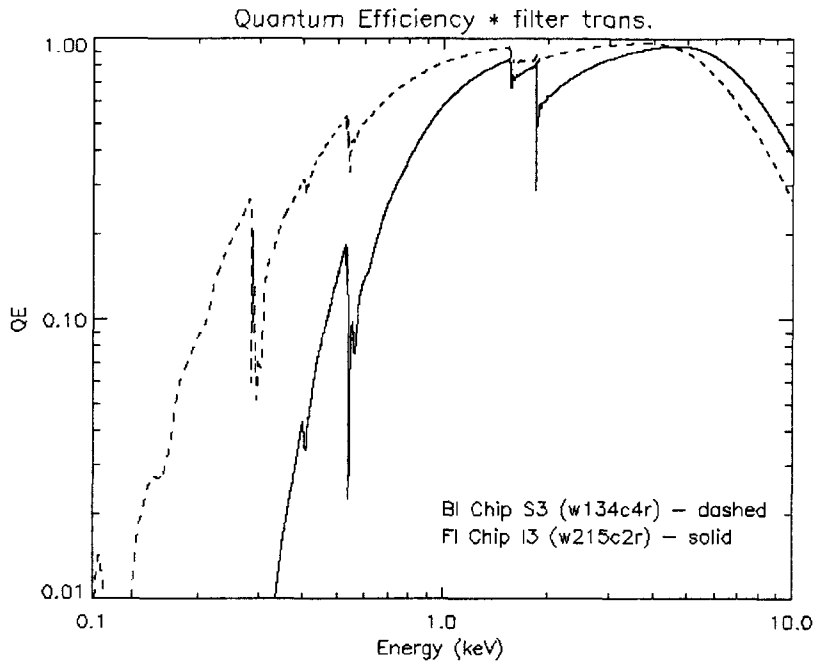

Figure 3.11: The HRMA/ACIS predicted effective area as a function of energy on a log scale. The solid line is for the FI CCD I3, and the dashed line is for the BI CCD S3.

since these are generated near the electrode. It is thus difficult to remove these events as backgrounds.

Markevitch (2001) shows the time dependence of the background count rate. Figure 3.14 shows the quiescent background count rates in different observations vs. time, for the ACIS-I and ACIS-S3 in soft (0.3–5 keV) and hard (5–10 keV) energy bands. The background count rate was almost constant within 10 % during the ACIS operation temperature −110°C. However, it declined about 20 % during the −120°C period until Fall 2000, after which it leveled off and started increasing.

3.3.9 Low energy quantum efficiency degradation in ACIS

An examination of archived astronomical observations and data acquired from the on-board ACIS calibration source (55Fe) shows that there has been a slow continuous degradation in the ACIS quantum efficiency since launch. This is considered due to molecular contamination building up on the cold optical blocking filter, and/or the CCD chips. This degradation is the most severe at low energies. Above 1 keV, the degradation is less than 10%. Analysis of the on-board calibration source shows that the L-complex (about half Mn-L and half Fe-L lines) to Mn-Kα line ratio has decreased at a steady rate since launch corresponding to a decrease in the quantum efficiency at 670 eV of about 10% per year.

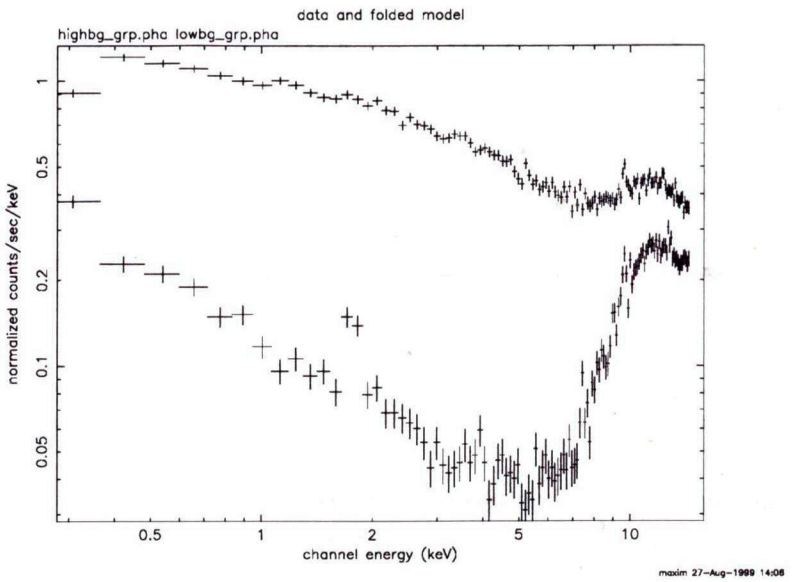

Figure 3.12: ACIS background spectra during flaring and quiescent period.

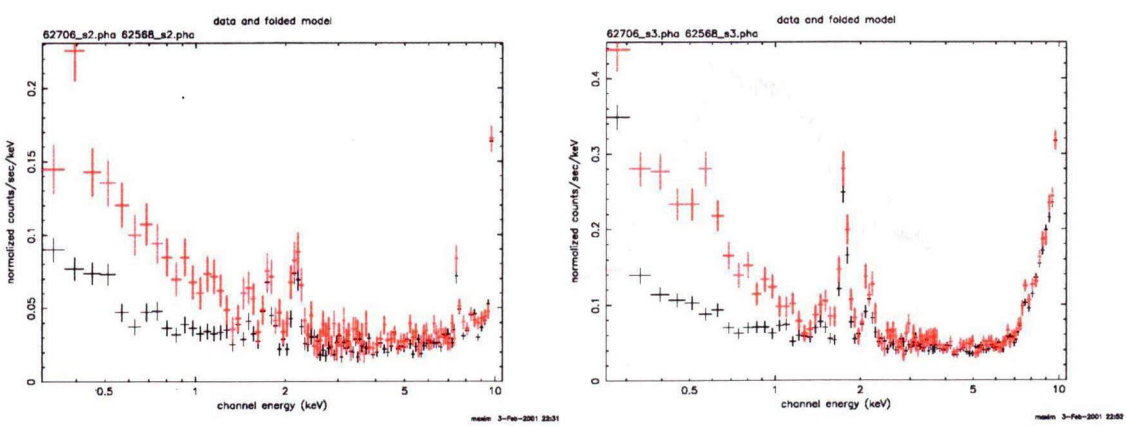

Figure 3.13: Quiescent background spectrum for an FI CCD (S2) (**left**) and a BI CCD (S3)(**right**). The cosmic ray component dominates above 5 keV. The background count rate of the BI is about three times higher than that of the FI in 0.3–10 keV.

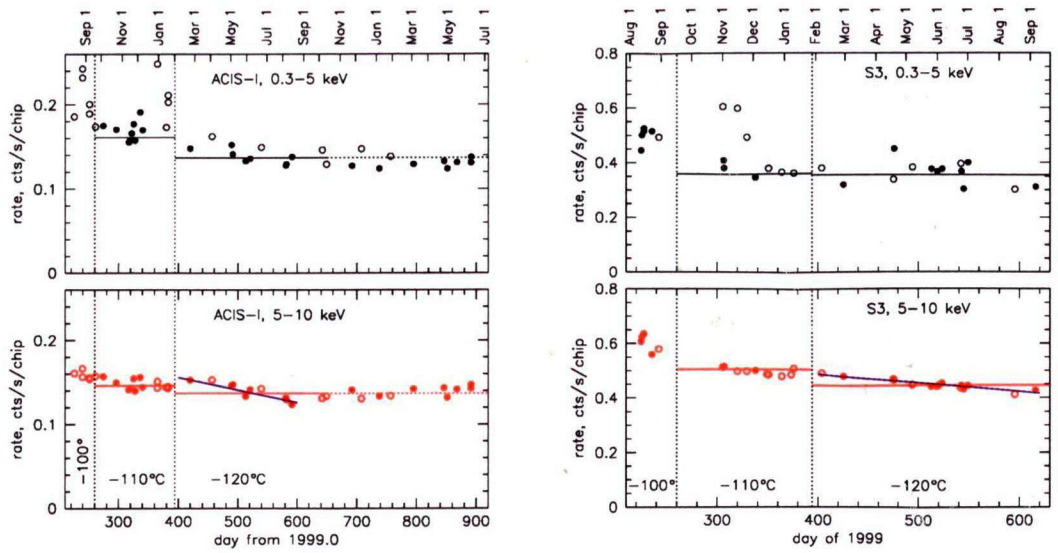

Figure 3.14: Time dependence of quiescent background count rates, for the ACIS-I (**left**) and ACIS-S3 (**right**) in the soft (0.3–5 keV) and hard (5–10 keV) energy bands.

In Figure 3.15, we show a comparison of the spectra of A1795 observed with ACIS-S in April 2000 and in June 2002. The C K-edge (284 eV) is clearly detected. Since the contamination rate well constrained, we can correct the effective area file based on the observing date.

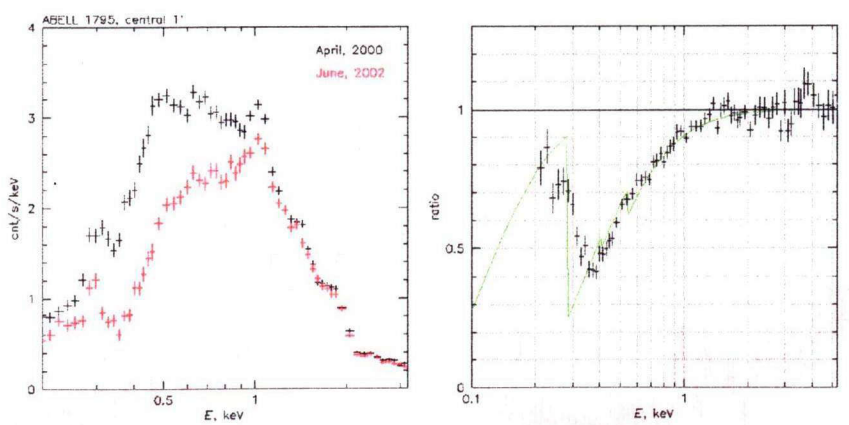

Figure 3.15: (**left**) ACIS-S spectra of A1795 from observations in April 2000 (black) and June 2002 (red). (**right**) Ratio of the June 2002 to the April 2000 spectrum of A1795.

Chapter 4

Observations and Data Analysis

4.1 Observations and Sample Selection

We selected our sample from *Chandra* archival data of galaxy clusters. To obtain spatially resolved spectra, we restricted the observations to those in which ACIS were employed without gratings. By the end of September 2002, the archive contained observation data for about 150 clusters ($\sim$ 200 pointings) that met this criterion. Among the 150 clusters, 7 clusters were observed as calibration (CAL) targets; of the remainder, half were done as Guaranteed Time Observer (GTO) targets and the other half as General Observer (GO) targets.

We applied the following criteria for further selection of the data in order to meet our main concern, investigation of the central mass profiles of galaxy clusters. First, clusters must be bright enough to provide spatially resolved spectra with good statistics. For this we referred to the catalog of Reiprich & Böhringer (2002), which consists of 106 bright clusters compiled from several catalogs based on the *ROSAT* All-Sky X-ray Survey (Voges et al. 1999). The minimum X-ray flux among the Reiprich samples is 0.234×10^{-11} ergs s^{-1} cm^{-2} (0.1–2.4 keV). This is bright enough for our analysis under typical observational conditions. Among the 106 clusters in Reiprich sample, 43 clusters are included in the *Chandra* data archive. Secondly, clusters should be spherically symmetric as our deprojection analysis assumes the spherical symmetry. We thus excluded merging clusters like A754 (Henriksen & Markevitch 1996). Although this second criterion is somewhat ambiguous, we will examine how this spherical symmetry assumption affects the final result in Chapter 5. The last criterion is that the X-ray emission from the outer region of a cluster must be covered by the detectors used in the observations. This is because the deprojection analysis depends on accurate measurement of temperatures and densities of the outer regions of clusters. Data for 20 clusters met all of these criteria.

We also employed three distant clusters, A1835, A963, and ZW3146, that are bright and spherically symmetric but that are not included in Reiprich & Böhringer (2002).

The observation log and the properties of each cluster are summarized in Table 4.1 and Table 4.2, respectively. The redshifts of the 23 sample clusters range from 0.0110 to 0.2906, with a median of 0.0852.

4.2 Data reductions

Data reduction and analysis were performed with the *Chandra* Interactive Analysis of Observations package, CIAO-2.2, with calibration database CALDB-2.12, as provided by the *Chandra* X-ray Center (CXC). We started the reduction from the standard level 2 event files archived at CXC, which are the products of the pipeline processing. We adopted the standard reduction scheme by following the CIAO threads[1].

As shown in §3.3.8, the *Chandra* background is strongly affected by particle flare events. To remove the flare events, we performed lightcurve screening using the CIAO task *lc_clean*. We first made a background lightcurve, a time history of the event rate taken from a source-free region on the detector, with a time bin size of 259.28 s using the CIAO task *lightcurve*. Figure 4.1 shows an example of the lightcurve screening for the A2199 observation. During the first part of the observation, the background was stably low. The last 2 ks, however, was heavily affected by a flare. In order to exclude flare events like this, we discarded the data taken at the time the count rate deviates from the mean by $\pm 3\sigma$, where the mean value is defined during the quiescent period.

4.3 Analysis

4.3.1 Spectra and backgrounds

Using the event file filtered by the lightcurve screening described in the §4.2 above, we extracted spectra in concentric annuli centered on the peak of the X-ray emission through the following steps.

1. Removal of point sources

   Many point sources, such as active galactic nuclei, galaxies, and stars, are detected in the X-ray images of target clusters. We removed the contamination of these sources by setting excluded areas on the X-ray images. Point source detection

[1] http://asc.harvard.edu/ciao/threads

Table 4.1: Observation log of the sample clusters.

ID	Cluster	Obs. ID	Ra (deg)[a]	Dec (deg)[a]	Observation date	Exp. (ks)	Screened[b] Exp. (ks)	ACIS[c] chip
1	A1060	2220	159.073	-27.569	2001-06-04 04:43:23	31.9	30.0	I
2	A133	2203	15.689	-21.882	2000-10-13 22:27:02	35.5	34.5	S
3	A1795	493	207.205	26.608	2000-03-21 07:54:49	19.6	19.6	S
		3666	207.204	26.576	2002-06-10 16:21:19	14.4	13.8	S
		494	207.236	26.607	1999-12-20 05:00:57	19.5	17.6	S
4	A1835	495	210.272	2.895	1999-12-11 16:48:33	19.5	19.5	S
		496	210.222	2.867	2000-04-29 06:55:44	10.7	10.7	S
5	A2029	891	227.725	5.764	2000-04-12 06:38:56	19.8	19.8	S
6	A2052	890	229.182	7.012	2000-09-03 06:01:22	36.8	36.8	S
7	A2199	498	247.188	39.553	1999-12-11 10:47:37	18.9	18.9	S
		497	247.135	39.560	2000-05-13 17:36:15	19.5	17.9	S
8	A2204	499	248.185	5.557	2000-07-29 02:49:42	10.1	10.1	S
9	A2597	922	351.337	-12.135	2000-07-28 05:13:47	39.4	25.1	S
10	A401	518	44.727	13.579	1999-09-17 21:35:26	18.0	18.0	I
		2309	44.732	13.461	2000-11-03 19:10:36	11.6	11.6	I
11	A478	1669	63.362	10.436	2001-01-27 03:28:03	42.4	42.4	I
12	A644	2211	124.329	-7.543	2001-03-26 00:27:49	29.7	29.2	S
13	A85	904	10.442	-9.374	2000-08-19 07:06:52	38.4	38.4	I
14	A963	903	154.284	39.063	2000-10-11 00:01:18	36.3	36.3	S
15	AWM7	908	43.665	41.664	2000-08-19 18:30:01	47.9	47.9	I
16	Centaurus	504	192.207	-41.334	2000-05-22 00:33:17	31.7	28.8	S
		505	192.199	-41.334	2000-06-08 00:51:50	10.0	10.0	S
17	Hydra A	575	139.527	-12.091	1999-10-30 07:29:02	23.8	23.8	I
		576	139.527	-12.091	1999-11-02 11:31:54	19.5	19.5	S
18	MKW3S	900	230.488	7.757	2000-04-03 12:26:13	57.3	57.3	I
19	NGC5044	798	198.859	-16.378	2000-03-19 15:42:42	20.5	19.8	S
20	PKS0745-191	2427	116.860	-19.306	2001-06-16 05:32:52	17.9	17.9	S
		508	116.870	-19.277	2000-08-28 22:15:31	28.0	4.6	S
21	Sersic159-03	1668	348.515	-42.713	2001-08-13 16:41:20	9.9	9.9	S
22	ZW3146	909	155.905	4.166	2000-05-10 03:20:25	46.0	46.0	I
23	2A0335+096	919	54.666	10.008	2000-09-06 00:03:13	19.7	14.1	S

[a] Nominal pointing position of the observation in Equinox 2000.0

[b] Exposure time after lightcurve screening (see §4.2)

[c] Detector on the aim point

Table 4.2: Properties of the sample clusters. We show the redshifts, hydrogen column densities of the galactic absorption, temperatures, and X-ray fluxes of the sample clusters. The temperatures are referred to Reiprich & Böhringer (2002), Ota (2000), and Allen et al. (1996).

Cluster	redshift	$N_{\rm H}^{a}$	kT	$f_{\rm X}{}^{b}$	Ref. [c]
		[10^{20} cm^{-2}]	[keV]	[10^{-11} ergs s^{-1} cm^{-2}]	
A1060	0.0126	4.79	$3.24^{+0.06}_{-0.06}$	9.95	R
A133	0.0570	1.55	$3.80^{+2.00}_{-0.90}$	2.12	R
A1795	0.0622	1.20	$7.80^{+1.00}_{-1.00}$	6.27	R
A1835	0.2530	2.30	$7.42^{+0.61}_{-0.43}$	1.47	O
A2029	0.0780	3.07	$9.10^{+1.00}_{-1.00}$	6.94	R
A2052	0.0345	2.78	$3.03^{+0.04}_{-0.04}$	4.71	R
A2199	0.0310	0.87	$4.10^{+0.08}_{-0.08}$	10.64	R
A2204	0.1511	5.66	$7.21^{+0.25}_{-0.25}$	2.75	R
A2597	0.0822	2.50	$4.40^{+0.40}_{-0.70}$	2.21	R
A401	0.0748	10.3	$8.00^{+0.40}_{-0.40}$	5.28	R
A478	0.0881	14.8	$8.40^{+0.80}_{-1.40}$	5.15	R
A644	0.0704	6.95	$7.90^{+0.80}_{-0.80}$	4.02	R
A85	0.0557	3.37	$6.90^{+0.40}_{-0.40}$	7.43	R
A963	0.2057	1.40	$6.83^{+0.51}_{-0.51}$	0.59	O
AWM7	0.0172	9.91	$3.75^{+0.09}_{-0.09}$	1.58	R
Centraurus	0.0110	8.07	$3.68^{+0.06}_{-0.06}$	27.19	R
Hydra A	0.0538	4.90	$4.30^{+0.40}_{-0.40}$	4.78	R
MKW3S	0.0450	3.04	$3.70^{+0.20}_{-0.20}$	3.30	R
NGC5044	0.0089	5.03	$1.07^{+0.01}_{-0.01}$	5.51	R
PKS0745-191	0.1028	40.7	$7.21^{+0.11}_{-0.11}$	2.44	R
Sersic159-03	0.0580	1.76	$3.00^{+1.20}_{-0.70}$	2.49	R
ZW3146	0.2906	2.94	$6.10^{+0.30}_{-0.30}$	0.66	A
2A0335+096	0.0349	17.6	$3.01^{+0.07}_{-0.07}$	9.16	R

[a] Hydrogen column density of the galactic absorption.

[b] X-ray flux in units of 10^{-11} ergs s^{-1} cm^{-2}. The energy bands are 0.1-2.4 keV for R and 2-10 keV for O and A.

[c] References R:Reiprich & Böhringer (2002), O:Ota (2000), and A:Allen et al. (1996).

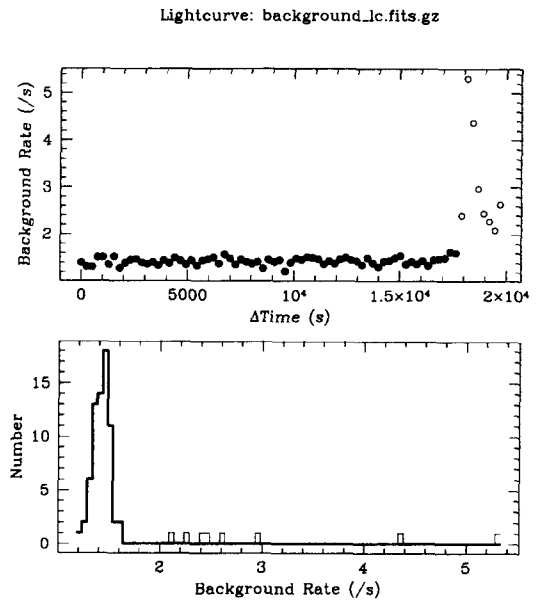

Figure 4.1: Example of lightcurve screening. The upper panel shows the background lightcurve in the A2199 observation (The observation ID is 497). The background increased significantly in the last 2 ks, owing to a flare event. The lower panel shows the histogram of the lightcurve count rate. In order to exclude all flare events, the time periods when the count rate deviates from the mean by $\pm 3\sigma$ are discarded, where the mean value is defined in the quiescent periods. Open circles and filled circles in the upper panel represent discarded portions and used portions of the lightcurve, respectively.

was performed with the CIAO wavelet source detection routine *wavdetect* with a significance parameter 10^{-6}. We made a 0.3–10 keV image binned by using a bin size of about $2 \times 2''$ (4×4 pixels). The area around the detected point sources was excluded in the following analysis. The upper panels of Figure 4.2 are the 0.3–10 keV images of MKW3S and A2029 from which point sources are removed. The overlaid contours indicate 0.1-2.0 keV images of *ROSAT* PSPC, in which the lowest contours are at the 4-σ background level.

2. Background estimation

   In order to estimate the background level to be subtracted from the X-ray spectra and images, we applied the blank-sky data compiled by Markevitch (2001) as background data. These background data are event files made with the same lightcurve screening process described in §4.2. These background event files are prepared with respect to each chip, aimpoint, and time of observation. Appropriate background files were selected with the script *acis_bkgrnd_lookup* provided by CXC. The background image was then mapped onto the sky with the same aspect solution as in the observation. The middle panels of Figure 4.2 show the background images for MKW3S and A2029.

3. Extraction of the source and background spectra

   The spectra were extracted in the concentric annuli centered on the X-ray peak with different widths to ensure similar statistics in the background-subtracted spectra. The X-ray peak was determined with the X-ray images from which point sources were removed. We examine what the appropriate setup is for the width of the annuli, or equivalently, the statistics of each spectrum, using the simulation in §4.3.3. The radius of the outermost annulus was determined to cover the 4-σ background level of the *ROSAT* PSPC image. The lower panels of Figure 4.2 show the adopted annuli. The background spectra were extracted from the background data with the same regions on the detector.

4. Building the instrumental response

   Redistribution Matrix Files (RMF) and Auxiliary Response Files (ARF) were made using the CIAO tasks of *mkrmf* and *mkwarf*. These tasks make a weighted RMF and a weighted ARF for the spectral analysis based on a 32×32 pixel grid of calibration files. This is because the RMF and ARF vary with detector location. To compensate for the degradation in low-energy efficiency shown in §3.3.9, we used the tool *corrarf* provided by CXC. The *corrarf* corrects the ARF according to the

observation date. In some cases, like A2029 in Figure 4.2, some annular regions stick out from the ACIS chip. We scaled the spectrum by the ratio of the covered region to the entire annular region.

4.3.2 Deprojection analysis

When we observe extended optically thin objects, we always measure the emission integrated along the line of sight. However, making some assumptions about three-dimensional structures, in which spherical symmetry is usually adopted as the simplest case, we can obtain a three-dimensional emissivity profile without assuming any particular model. Such a technique is called deprojection analysis or the deconvolution method, and it has been applied to cluster X-ray emission profiles (Fabian et al. 1980; Fabian, Hu, Cowie, & Grindlay 1981). As mentioned in (Sarazin 1988), if both spectral and spatial information is available, deprojection analysis will provide both the gas density profile $n_g(r)$ and the temperature profile $kT(r)$. However, in most of the previous deprojection analyses of cluster X-ray emissions, limited instrument capability allowed only X-ray spatial profiles and not spectral information. Therefore, a further assumption usually had to be made for either temperature profile $kT(r)$, gas density profile $n_g(r)$, or gravitational potential profile $\phi(r)$. New generation instruments, such as *Chandra* or *XMM-Newton*, enable us to utilize both spectral and spatial information, so no such additional assumption is necessary in deprojection analysis. Arabadjis, Bautz, & Garmire (2002) developed a new deprojection technique and applied it to *Chandra* data for the cluster EMSS 1358+6245. We principally follow the technique of Arabadjis, Bautz, & Garmire (2002), We introduce this deprojection analysis in this subsection.

A Schematic view of the deprojection analysis is shown in Figure 4.3. In this example, we extract spectra from N concentric annular regions. The projected luminosity S_j in a given energy band on the jth annulus is expressed by the integration of emissivities along the line of sight. The relationship between S_j and the volume emissivity e_i of the ith spherical shell is expressed as

$$S_j = \sum_{i=j}^{N} V_{ij} e_i. \tag{4.1}$$

where V_{ij} is the volume of the ith spherical shell intersected by a cylindrical shell whose radius equals the jth projected annulus. Note that we have to make sure, or make the assumption that, X-ray emission is negligible outside of the outermost annulus. V_{ij} is

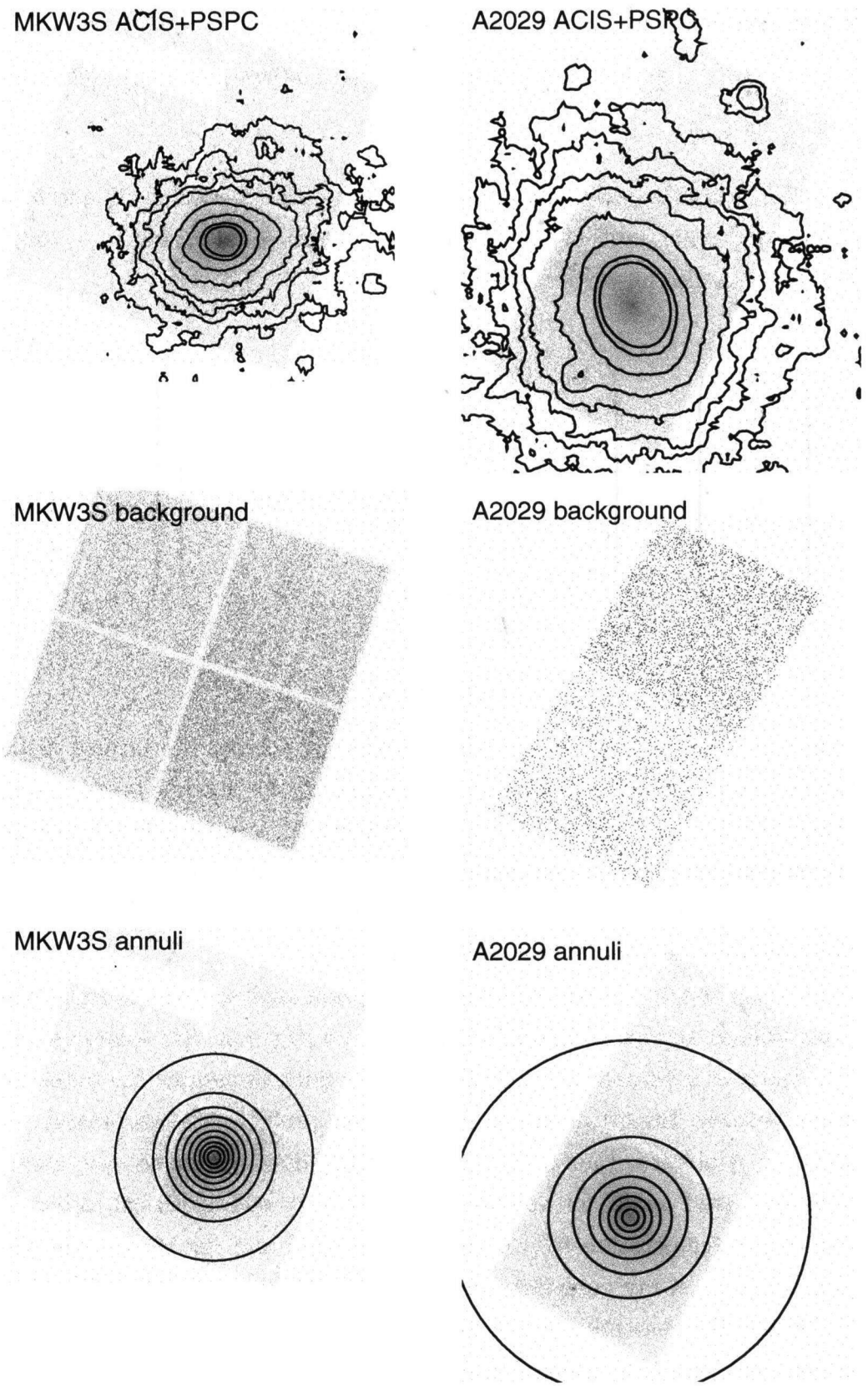

Figure 4.2: (**Top**) 0.3–10 keV *Chandra* images of MKW3S (**left**) and A2029 (**right**). The overlaid contours are the 0.1–2.0 keV ROSAT PSPC images. The contour levels correspond to n times the 1σ background levels for n = 4, 8, 12, 18, 36, 72, 144, and 200. (**Middle**) ACIS background images mapped onto the sky with the same aspect solution as in the observation. (**Bottom**) Annuli adopted in the spectral analysis.

geometrically calculated as

$$\begin{aligned} V_{ij} &= \frac{4}{3}\pi[(r_{i+1}^2 - b_j^2)^{3/2} - (r_{i+1}^2 - b_{j+1}^2)^{3/2} - (r_i^2 - b_j^2)^{3/2} + (r_i^2 - b_{j+1}^2)^{3/2}] \quad (i \leq j) \\ &= 0 \quad (i < j), \end{aligned} \tag{4.2}$$

where r_i and r_{i+1} are the inner and outer radii of the ith spherical shell, and b_j and b_{j+1} are the inner and outer radii of the jth annulus, which equal r_j and r_{j+1}, respectively. Equation (4.1) can also be written for all annuli as

$$\begin{pmatrix} S_0 \\ S_1 \\ \vdots \\ S_j \\ \vdots \\ S_{N-1} \end{pmatrix} = \begin{pmatrix} V_{00} & V_{01} & \cdots & V_{0j} & \cdots & V_{0N-1} \\ 0 & V_{11} & \cdots & V_{1j} & \cdots & V_{1N-1} \\ \vdots & & & \ddots & & \vdots \\ 0 & 0 & \cdots & V_{ij} & \cdots & V_{iN-1} \\ \vdots & & & \ddots & & \vdots \\ 0 & 0 & \cdots & 0 & \cdots & V_{N-1N-1} \end{pmatrix} \begin{pmatrix} e_0 \\ e_1 \\ \vdots \\ e_i \\ \vdots \\ e_{N-1} \end{pmatrix}, \tag{4.3}$$

that is,

$$\mathbf{S} = \mathbf{V} \cdot \mathbf{e}. \tag{4.4}$$

Since $\mathbf{V}$ is a triangle matrix, we can obtain the $\mathbf{e}$ by solving the inverse matrix $\mathbf{V}^{-1}$. Note that this equation is for luminosity and emissivity for a single energy band in this explanation, but the same equation with the same matrix $\mathbf{V}$ is valid for any energy band. Therefore, this equation means that a set of X-ray spectra from different projected annuli are determined by a set of X-ray emissivities at different spherical radii. The inverse is true if the spectral resolution is negligibly small.

As mentioned above, in most previous deprojection analyses, only X-ray spatial information was utilized and an additional assumption on $kT(r)$ or $\phi(r)$ was necessary. Even when both types of information are available, some authors assume the potential profile $\phi(r)$, or equivalently, the gravitational mass density profile $\rho(r)$, beforehand. However, the method by Arabadjis, Bautz, & Garmire (2002) does not make such assumptions. We first make a trial model for volume emissivity $\mathbf{e}$ at each spherical radius, which is a function of gas temperature $kT(r)$, gas density $n_g(r)$ and gas abundance $Z(r)$ when we employ some an X-ray emissivity model of thin thermal plasma. We adopted the MEKAL (Mewe, Gronenschild, & van den Oord 1985; Mewe, Lemen, & van den Oord 1986; Kaastra & Mewe 1993; Liedahl, Osterheld, & Goldstein 1995) model in the XSPEC data analysis package for our X-ray emissivity model, in which normalization K is used instead of gas density $n_g(r)$. Therefore, the number of free parameters to be determined is $3\times N$ except for an additional free parameter for the interstellar absorption. We can

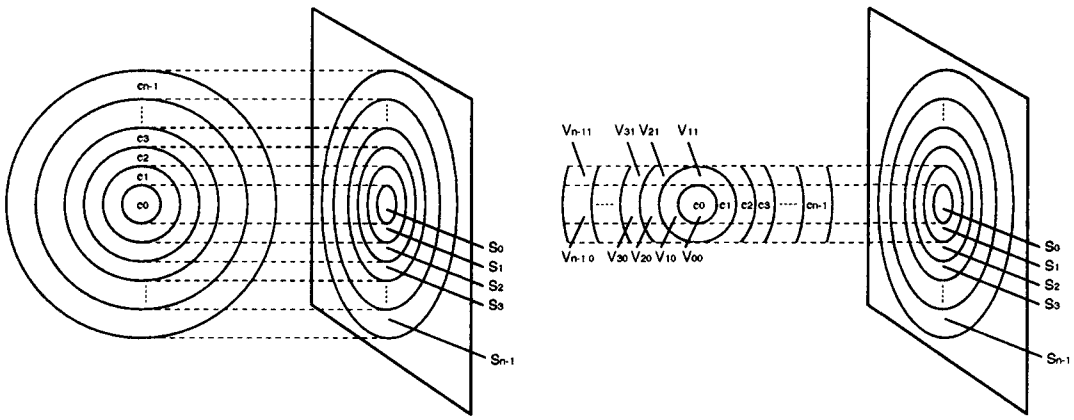

Figure 4.3: Schematic view of the deprojection analysis.

examine how this trial model fits the set of spectra by χ^2 value, and we can improve the fit by changing the parameter values $kT(r)$ and $n_g(r)$. This procedure is done with the XSPEC data analysis package as a simultaneous spectral fitting of N spectra.

In Figure 4.4, we show an example of the deprojection analysis in a case where spectra are extracted from 12 concentric annuli. Since the spectrum of the outermost annulus consists of the emission from only the outermost spherical shell, one MEKAL component is applied for the outermost spectrum. On the other hand, the rest of the spectra are superposed along the line of sight. Thus, the summation of multiple MEKAL components, which are weighted by the (fixed) ratio of V_{ij} to V_{0j}, is compared with the inner spectra. As mentioned above, the free parameters are temperature kT_i, normalization K_i, and abundance Z_i, where i indicates those values at each spherical radius. In addition to the MEKAL model, we take into account the interstellar photoelectric absorption model using Wisconsin (Morrison & McCammon 1983) cross-sections (WABS). The gas density $n_{g,i}$ is derived from the normalization K_i of the MEKAL model. K is defined as

$$K = \frac{10^{-14}}{4\pi(D_A(1+z))^2} \int n_e n_p dV, \tag{4.5}$$

where D_A is the angular size distance to the source, and n_e and n_p are the electron and proton densities. We assume $n_p = 0.82 n_e$ in the ionized ICM and $n_{g,i} = n_{e,i}$.

4.3.3 Simulation for deprojection analysis

In our deprojection analysis, limited photon counts in each spectrum sometimes cause spurious results in the numerical iterations in XSPEC (Arabadjis, Bautz, & Garmire 2002). We performed a simulation to estimate the photon counts needed to constrain the

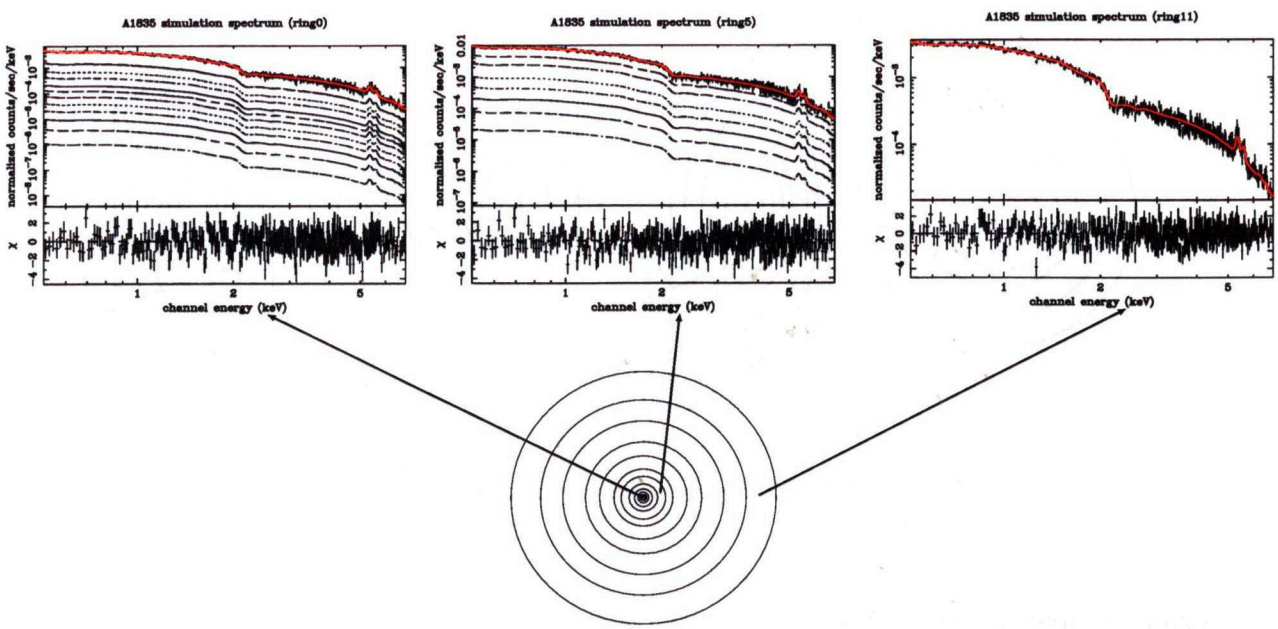

Figure 4.4: Models for the spectra extracted from $j = 0,5,11$ annuli in the case that the cluster consists of $N = 12$ shells.

temperature and density profiles, or, equivalently, to optimize the number of annuli to take for a given statistic of a spectrum.

We first constructed a model for the cluster consisting of $N = 8$ shells. We assumed the temperature is constant (kT=9keV) for all shells, and the gas density is described with the β model, of which $\beta = 0.6$ and the core radius $r_c = 35$ kpc. From these models, we created the spectra expected to be observed for the projected annuli with the XSPEC *fakeit* command. We simulated six cases, each for a projected spectrum containing a different number of photons: 5×10^3, 1×10^4, 2×10^4, 3×10^4, 4×10^4, or 5×10^4 photons.

The temperature and density profiles are obtained with the same deprojection technique shown in §4.3.2. Figure 4.5 shows the temperature and density profiles of the simulated spectra. The density profiles derived are well consistent with the input model within the range of error, while the temperature profiles show a "jog", especially in the spectra with lower counts. This kind of jog in temperature profiles is also reported in Arabadjis, Bautz, & Garmire (2002). They attributed the jogs to the unexceptional statistical fluctuation.

In order to examine the jogs, we simulated the case in which the cluster consists of various numbers of shells (N =6,8,12, and 24). Figure 4.6 shows the temperature profiles in these cases. Each spectrum has the same photon count (2×10^4 counts); that is, the total counts are 1.2×10^5, 1.6×10^5, 2.4×10^5, and 4.8×10^5, respectively. The amplitude of the jog is larger for a larger number of shells. This structure is probably due to the

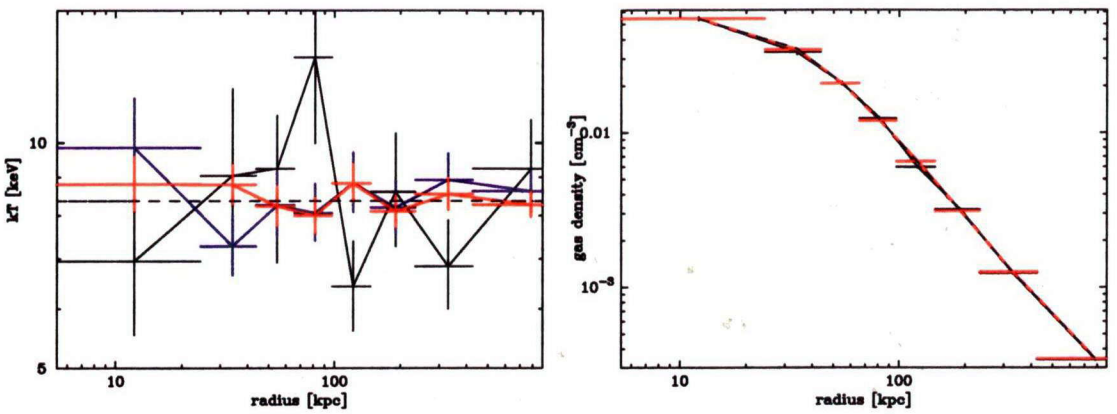

Figure 4.5: Temperature and density profiles of the simulated spectra. Black, blue, and red data represent projected spectra is containing 5×10^3, 2×10^4, and 5×10^4 photons, respectively. Black dashed lines represent the models assumed in the simulation.

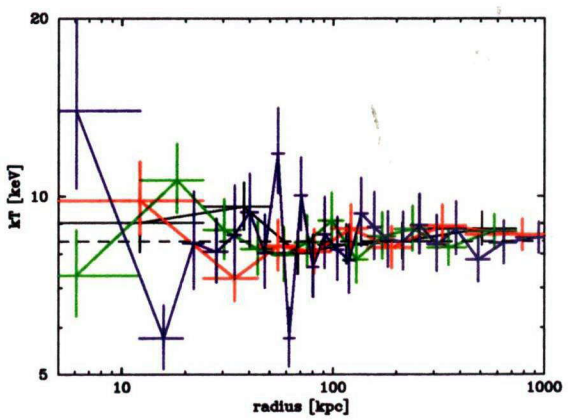

Figure 4.6: Simulated temperature profiles in cases with clusters consisting of consists various numbers of shells: $N = 6$ (black),8 (red), 12 (green), and 24 (blue).

interference between two neighboring spectra, since the jogs at two adjacent radius bins go in different directions. From these simulations, in order to suppress the jog in the temperature profile, we restricted the photon count per each annulus and the number of annuli, as follows: followings:

- The photon count per each annulus must be at least 1×10^4 , and
- The number of annuli N must be $5 \leq N \leq 10$.

In Table 4.3, we show the parameters we used in the extraction of spectra.

Table 4.3: Parameters used in the extraction of the spectra.

Cluster	X-ray center[a] (Ra, Dec)		Number[b] of annuli	Counts[c] /spectrum	Outermost radius (′)	(kpc)
A1060	159.178	-27.529	7	30000	16.4	353.3
A133	15.673	-21.883	7	20000	8.2	740.5
A1795	207.218	26.593	8	80000	12.3	1201.5
A1835	210.258	2.879	7	10000	2.7	801.6
A2029	227.732	5.744	7	43000	8.2	978.6
A2052	229.185	7.021	5	40000	6.9	391.0
A2199	247.160	39.551	10	60000	16.4	841.3
A2204	248.196	5.575	6	10000	4.1	844.8
A2597	351.332	-12.124	7	20000	6.6	819.5
A401	44.743	13.583	5	30000	9.0	1037.5
A478	63.354	10.465	9	40000	8.2	1087.3
A644	124.357	-7.511	6	30000	10.7	1162.8
A85	10.459	-9.302	8	40000	8.2	724.7
A963	154.266	39.047	5	10000	4.1	1059.8
AWM7	43.615	41.579	7	80000	16.4	478.2
Centaurus	192.203	-41.312	10	80000	18.9	355.3
Hydra A	139.524	-12.096	7	40000	8.2	702.6
MKW3S	230.466	7.709	8	25000	5.8	424.6
NGC5044	198.850	-16.386	10	20000	10.7	163.0
PKS0745-191	116.880	-19.295	6	25000	3.8	570.1
Sersic159-03	348.494	-42.726	5	10000	4.9	451.1
ZW3146	155.915	4.186	5	12000	3.3	1062.3
2A0335+096	54.671	9.967	7	40000	9.8	564.4

[a] Position of the center determined from the X-ray peak in Equinox 2000.0.

[b] Number of annuli adopted in the extraction of spectra.

[c] Total source photon counts per each annulus in 0.3–10 keV.

4.3.4 Fitting of the spectra

We extracted the X-ray spectra following the procedures show in §4.2. The spectra were grouped such that there were a minimum of 20 counts channel^{-1}. The simultaneous fit of the spectra was performed with the XSPEC, Version 11.2.0 package. Because the uncertainty in the instrumental response is relatively significant in the lower energy band, and the background is dominant in the higher energy band (see §3.3.8), we limited the energy band to be used in the fitting to 0.5-7.0 keV[2]. The hydrogen column density $N_{\rm H}$ was determined as a free parameter in the spectral fitting at the same time. However, for some clusters, the column density was poorly constrained. In such case, we fixed the absorption column to the Galactic value. The values of the hydrogen column density we measured or used in the fitting are listed in Table 5.1.

In Figure 4.7 and Figure 4.8, we show an example of the spectrum fitting. As mentioned in §4.3.2, the deprojected temperature kT, gas density $n_{\rm e}$, and abundance Z are obtained for each shell. Although the abundance profile, which concerns the metal enrichment process in the ICM, is an interesting topic on the X-ray study of clusters (see, e.g., Fukazawa 1997), we focus on the temperature and gas density profiles in this thesis to investigate the central mass profile of galaxy clusters.

[2]For Centaurus cluster, we also excluded 1.5-2.5 keV, because the calibration uncertainty is significant.

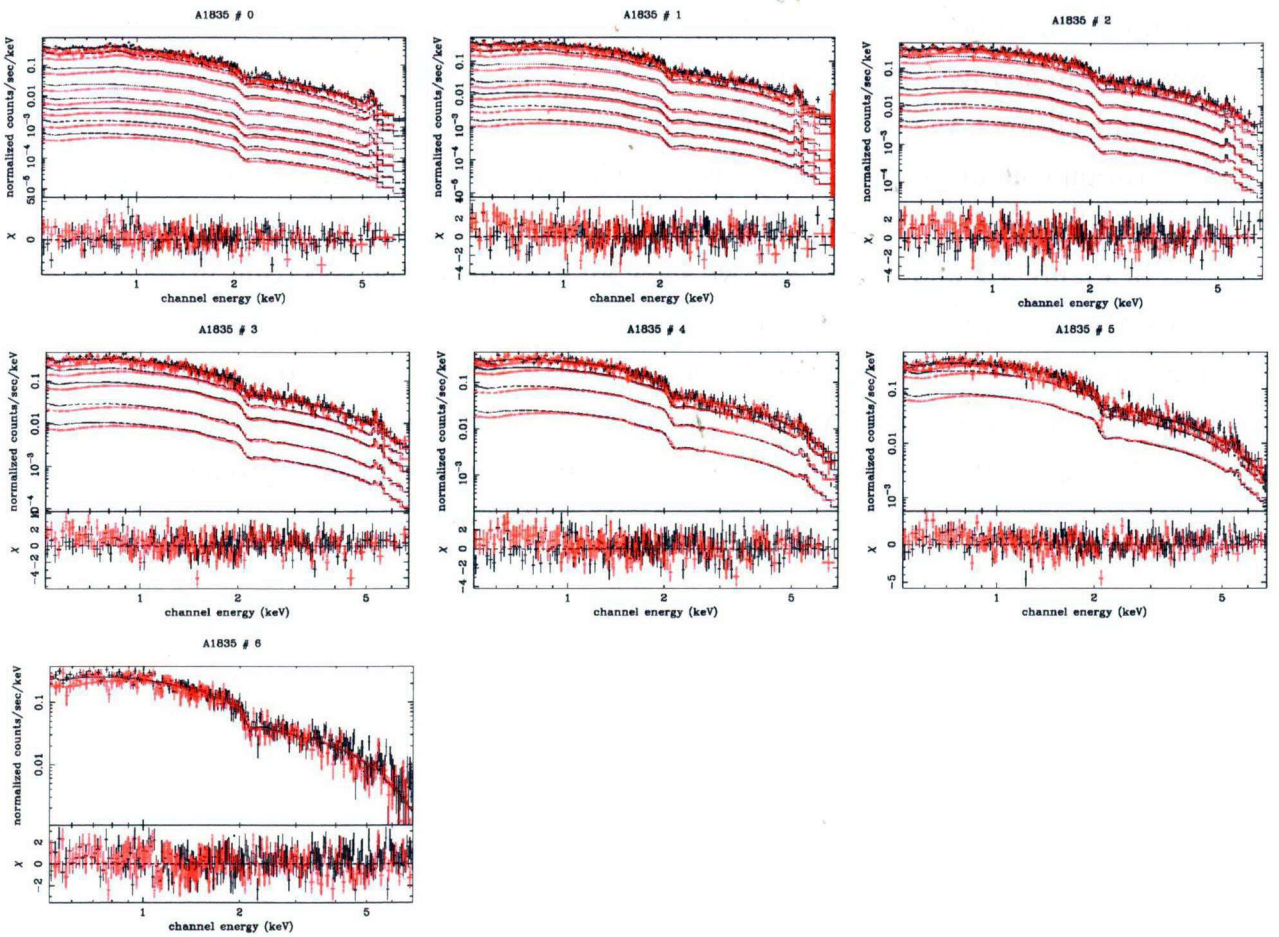

Figure 4.7: An example of the spectrum fitting. In this example (A1835), we fitted the $N = 7$ spectra for two data sets simultaneously. Observation IDs of each data set are 495 (red) and 496 (black).

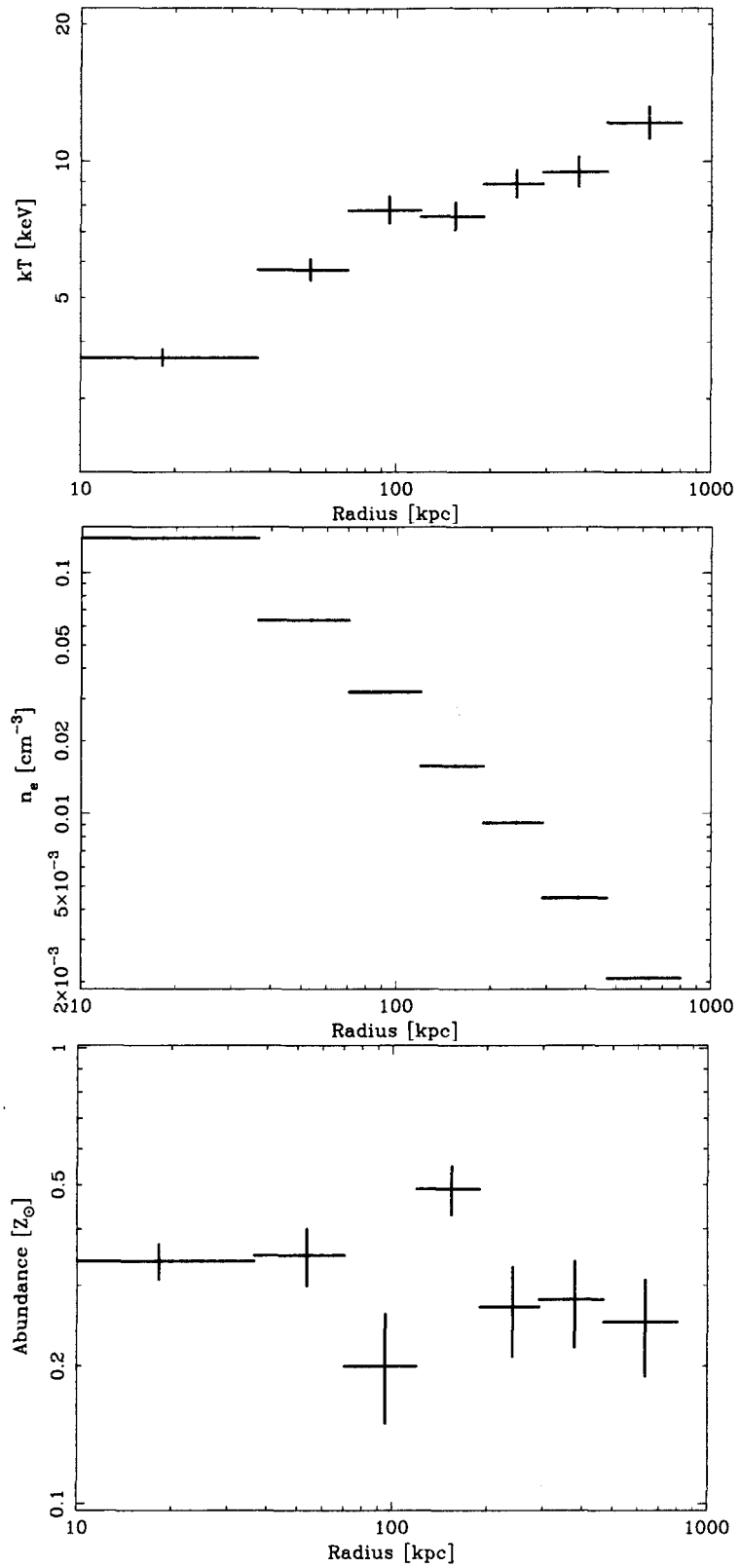

Figure 4.8: Deprojected temperature (**top**), gas (electron) density (**middle**), and abundance (**bottom**) profiles of A1835. we focus on the temperature and gas density profiles in this thesis.

Chapter 5

Results

5.1 Temperature and gas density profiles

Temperature and density profiles as a function of radius have been extensively studied since the discovery of X-ray emissions from clusters. Systematic studies for a large number of clusters using the X-ray data from previous missions, such as *ROSAT* or *ASCA* have been published by several authors (e.g. Markevitch et al. 1998; White & Buote 2000). However, the high spatial resolution imaging spectroscopy of *Chandra* enables us to measure both the temperatures and gas densities in the very central region of a cluster of galaxies. It also enables us to apply the new deprojection technique in which the temperature and density profiles are derived without assuming any particular models. In the next section, we focus on the spatial distribution of total gravitational mass, which is calculated directly from the temperature and gas density profiles we derived. In this section, we examine the temperature and gas density profiles themselves.

The temperature and gas (electron) density profiles of all sample clusters are shown in Appendix B. In each panel, we also show the pressure profile, which is simply derived from the temperature and gas density with the equation of the state of ideal gas: $P = n_e kT$. To examine the validity of our spectral analysis, we compare the spatially averaged temperatures of our results with the temperatures previously measured with *ASCA* or *ROSAT* (see Table 4.2). We defined the spatially averaged temperature as

$$T_{\rm average} \equiv \frac{\sum_{i=1}^{N} n_{ei}^2 V_i \sqrt{T_i} T_i}{\sum_{i=1}^{N} n_{ei}^2 V_i \sqrt{T_i}}, \tag{5.1}$$

where V_i, $n_{e,i}$, and T_i are the volume, gas density, and temperature of the ith spherical shell, respectively.

The spatially averaged temperatures calculated in this way are summarized in Table 5.1 and compared with the previous measurements in Figure 5.1. Note that each temper-

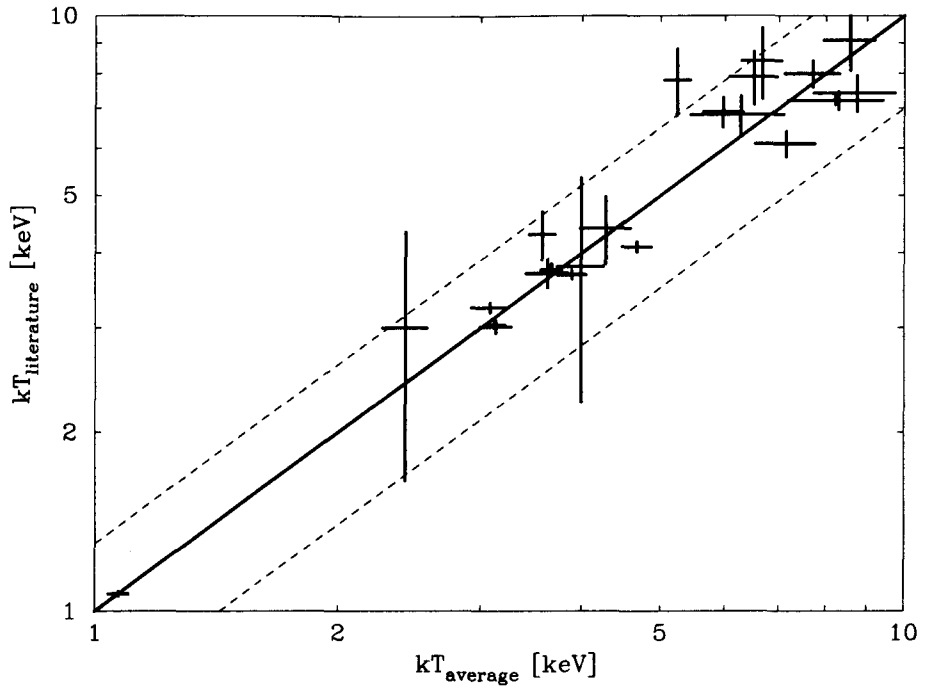

Figure 5.1: Comparison of the spatially averaged temperatures we derived with those in previous measurements reported in the literature. The temperatures from our measurement and those from previous reports are consistent within about 30 % (dashed lines).

ature value among the previous measurements is usually derived from an X-ray spectrum of the whole cluster region, which is not necessarily the same region as that used in our analysis. Nevertheless, our temperature values and the previous ones are consistent within about 30 %.

We attempted to model the temperature and density profiles with analytic functions. Note that the total mass profile can be calculated without employing such models, as shown in the next section. However, we investigated for another way to obtain the total mass profile, to which end such models are employed. We examined the following two empirical models for the temperature profiles: (1) exponential + constant model given by

$$T(r) = T_0 + T_1 \exp(-r/r_T); \tag{5.2}$$

and (2) simple power-law model given by

$$T(r) = T_0 (r/r_T)^{\alpha}. \tag{5.3}$$

The fitting results are summarized in Table 5.2 and Table 5.3. The averages of reduced χ^2 (χ^2/dof) were 16.7 for the exponential + constant model and 25.1 for the power-law model, indicating that neither model provides an acceptable fit for most clusters.

Table 5.1: Fitting results of the spectra of the sample clusters. The photon weighted average temperatures ($kT_{avarage}$), hydrogen column density N_H, and the χ^2 values with the number of degrees of freedom (dof) are shown.

Cluster	$kT_{avarage}$ [keV]	N_H [10_{20} cm_{-2}]	χ_2/dof
A1060	3.08 ± 0.16	$9.45^{+0.13}_{-0.13}$	2594.8/2188
A133	3.99 ± 0.26	1.55 (fixed)	2548.9/1718
A1795	5.24 ± 0.19	1.20 (fixed)	10070.6/7532
A1835	8.73 ± 1.00	$2.28^{+0.11}_{-0.11}$	2613.4/2251
A2029	8.57 ± 0.62	3.07 (fixed)	3310.2/2673
A2052	3.12 ± 0.09	$1.49^{+0.06}_{-0.06}$	3163.4/1652
A2199	4.67 ± 0.19	0.87 (fixed)	9142.0/6237
A2204	8.29 ± 1.11	$2.87^{+0.15}_{-0.15}$	1440.9/1185
A2597	4.28 ± 0.30	2.50 (fixed)	2406.1/1770
A401	7.71 ± 0.60	$14.09^{+0.16}_{-0.14}$	4091.1/2715
A478	6.67 ± 0.38	$25.96^{+0.08}_{-0.09}$	4942.8/3253
A644	6.51 ± 0.44	$13.94^{+0.15}_{-0.15}$	2493.5/2199
A85	5.97 ± 0.33	$4.52^{+0.09}_{-0.09}$	4384.0/2957
A963	6.27 ± 0.82	1.40 (fixed)	1221.3/1051
AWM7	3.67 ± 0.11	$13.82^{+0.07}_{-0.07}$	4291.1/2909
Centaurus	3.89 ± 0.16	$10.02^{+0.04}_{-0.06}$	6394.7/3741
Hydra A	3.57 ± 0.13	$7.29^{+0.11}_{-0.11}$	7277.9/3686
MKW3S	3.63 ± 0.22	$5.38^{+0.33}_{-0.03}$	3834.6/2863
NGC5044	1.07 ± 0.03	$11.52^{+0.09}_{-0.08}$	2604.9/1474
PKS0745-191	8.21 ± 0.53	$34.87^{+0.16}_{-0.17}$	3766.6/3014
Sersic159-03	2.42 ± 0.15	1.76 (fixed)	1079.0/831
ZW3146	7.15 ± 0.61	$5.46^{+0.20}_{-0.20}$	1512.7/1192
2A0335+096	3.13 ± 0.14	$22.05^{+0.10}_{-0.13}$	3331.4/1883

These large reduced χ^2 values are likely to be due to local fluctuations in the intrinsic temperature profiles or to unknown systematic errors in our analysis procedure. Note that we integrate the above model functions within one radius bin to obtain each model point. Thus, a coarse sampling is not the cause of the large χ^2 values. Although we could not determine which model is appropriate in either case, we adopted the exponential + constant model in the following analysis. One of the reasons to adopt this model is that the temperature profile is expected to asymptote to a certain temperature at large radii. Another reason is that recent *Chandra* and *XMM-Newton* observations of cooling flow clusters suggest that there are certain lower cut-off temperatures in the central region of the cluster (Tamura et al. 2001; Peterson et al. 2001).

Three parameters in the exponential + constant model were determined by the χ^2 fitting, but their error estimation was not trivial when the fitting was unacceptable. In order to estimate conservative errors for the parameters, we assigned a systematic error to each data point in the temperature profile. The systematic error of the temperature is assumed to be the constant fraction of the measured temperature for all the data points, where the fraction is determined so as to obtain the reduced χ^2 of unity in each temperature profile. Note that the total error is calculated to be the square root of the quadratic sum of the statistical and systematic errors. For some clusters, the original (i.e., before assignment of the systematic error) reduced χ^2 is small enough to accept the fit. We assigned the systematic error only for the clusters for which the original fitting was rejected by the χ^2 test with a significance level less than 1 %. In Table 5.3, we show the best fit values of the parameters and their 1σ errors obtained in this manner. The temperature profiles of A1060, A401, and A644 are almost constant, and we set the constant temperatures (isothermal) for these clusters in the following analysis.

AIn addition to fitting the temperature profiles, we fitted the density profiles with following two models: (1) isothermal β model given by Equation (2.21):

$$n_g(r) = n_{e0}\ (1 + (r/r_c)^2)^{-\frac{3}{2}\beta},$$

and (2) NFW gas density model given by Equation (2.26):

$$n_g(r) = n_{e0}\ \exp[-B(1 - \frac{\ln(1 + (r/r_s))}{(r/r_s)})].$$

The fitting results are summarized in Table 5.4 and Table 5.5. The averages of the original reduced χ^2 are 469.6 for the β model and 421.6 for the NFW gas density model, indicating that the fit is far from acceptable. In fact, the fitting models are rejected for all the clusters with a significance level less than 1 %. Hence, as was the case for the temperature profiles, we adopted the systematic error for all the clusters. The values and

Table 5.2: Fitting results of the temperature profiles with the power-law model.

Cluster	T_0 [keV]	r_T [kpc]	α	χ^2/dof
A1060	5.30±0.36	995.7±660.6	-0.11±0.01	69.3/5
A133	0.66±0.02	94.1±12.8	0.33±0.01	40.5/5
A1795	1.70±0.06	159.3±13.8	0.20±0.01	155.8/6
A1835	1.48±0.12	103.4±28.2	0.33±0.02	8.9/5
A2029	2.69±0.16	144.4±22.7	0.21±0.01	8.5/5
A2052	0.60±0.01	17.8±2.8	0.32±0.01	438.4/3
A2199	1.40±0.04	57.8±5.2	0.22±0.01	278.9/8
A2204	1.58±0.11	60.7±9.4	0.26±0.02	65.9/4
A2597	0.86±0.06	162.7±29.1	0.31±0.01	2.0/5
A401	13.63±2.60	13.1±718.1	-0.10±0.03	9.5/3
A478	1.71±0.06	50.8±7.9	0.24±0.01	131.2/7
A644	5.25±0.49	14.4±1.3	0.03±0.02	37.7/4
A85	1.54±0.06	70.0±8.4	0.23±0.01	110.3/6
A963	4.01±0.77	13.3±6.1	0.08±0.04	1.8/3
AWM7	2.44±0.08	7.1±0.1	0.08±0.01	222.3/5
Centaurus	0.48±0.01	87.6±4.2	0.41±0.00	1077.1/8
Hydra A	2.40±0.07	91.9±23.7	0.08±0.01	35.2/5
MKW3S	3.11±0.16	21.0±8.8	0.02±0.01	54.5/8
NGC5044	0.35±0.01	92.6±8.3	0.26±0.00	378.9/8
PKS0745-191	1.04±0.06	154.6±25.7	0.39±0.01	5.9/4
Sersic159-03	1.13±0.08	58.0±15.7	0.16±0.02	7.5/3
ZW3146	1.67±0.12	57.2±13.0	0.26±0.02	42.3/3
2A0335+096	0.44±0.01	106.8±7.7	0.39±0.01	96.5/5

Table 5.3: Fitting results of the temperature profiles with the exponential + constant model.

Cluster	T_0 [keV][a]	T_1 [keV][a]	r_T^a [kpc]	χ^2/dof[b]	Systematic error[c]
A1060	3.16 ± 0.22	-0.00 ± 0.80	850.0 ± 918.5	126.4/4	0.183
A133	4.52 ± 0.36	-3.45 ± 0.33	90.9 ± 28.5	20.7/4	0.082
A1795	6.03 ± 0.51	-3.36 ± 0.57	151.4 ± 63.1	105.1/5	0.099
A1835	10.10 ± 0.69	-7.60 ± 0.56	103.4 ± 28.2	10.2/4	..
A2029	9.89 ± 0.30	-5.73 ± 0.34	144.4 ± 22.7	3.9/4	..
A2052	3.20 ± 0.27	-5.67 ± 8.39	14.9 ± 22.4	24.8/2	0.734
A2199	4.92 ± 0.32	-3.34 ± 0.41	57.2 ± 22.2	97.3/7	0.093
A2204	8.45 ± 1.29	-7.21 ± 1.80	58.1 ± 34.0	26.1/3	0.235
A2597	6.02 ± 0.39	-4.33 ± 0.35	162.7 ± 29.1	6.6/4	..
A401	7.71 ± 0.62	0.00 ± 29.09	12.9 ± 0.1	19.0/2	0.170
A478	7.03 ± 0.35	-5.52 ± 0.78	48.4 ± 20.0	33.6/6	0.076
A644	6.47 ± 0.39	-28.72 ± 28.72	14.9 ± 27.3	27.6/3	0.128
A85	6.44 ± 0.27	-4.56 ± 0.46	78.4 ± 21.6	26.0/5	0.065
A963	6.22 ± 0.25	-29.78 ± 23.80	13.3 ± 6.1	1.5/2	..
AWM7	3.78 ± 0.10	-29.60 ± 27.94	7.2 ± 3.8	52.8/4	0.064
Centaurus	4.63 ± 0.90	-3.92 ± 0.86	78.0 ± 35.2	1167.4/7	0.215
Hydra A	3.80 ± 0.24	-0.95 ± 0.28	113.3 ± 95.0	33.4/4	0.064
MKW3S	3.71 ± 0.14	-1.10 ± 0.59	30.9 ± 23.2	42.3/7	0.078
NGC5044	1.65 ± 0.39	-1.10 ± 0.37	102.9 ± 54.5	168.6/7	0.065
PKS0745-191	11.16 ± 0.65	-8.89 ± 0.57	154.6 ± 25.7	9.9/3	..
Sersic159-03	2.69 ± 0.09	-1.31 ± 0.13	58.0 ± 15.7	1.8/2	..
ZW3146	8.04 ± 0.31	-6.86 ± 0.58	57.2 ± 13.0	0.6/2	..
2A0335+096	3.96 ± 0.40	-3.18 ± 0.35	97.1 ± 30.2	60.6/4	0.089

[a] Errors are estimated by including a systematic error (see text).

[b] Original reduced χ^2 before including a systematic error.

[c] Systematic error adopted so as to get the reduced χ^2 value of unity

errors in Table 5.4 and Table 5.5 were made considering the systematic errors. Of these two models, we selected the NFW gas density model for the following reason. The X-ray surface brightness profiles of some clusters show the central excess components. These are well described by a double β model in which another β-model component is incorporated (e.g. Mohr, Mathiesen, & Evrard 1999; Ota 2000). Thus, use of the single β model might allow us to miss a central excess component. On the other hand, the NFW gas density model shows a cuspy profile similar to that of the double β model and is a good alternative to it at the cluster center.

Suto, Sasaki, & Makino (1998) examined the gas distributions expected from the NFW profile. They fitted the simulated gas density profile with the NFW gas density model and found that the parameter B is in the range from 5 to 20. The parameter B we measured is consistent with Suto, Sasaki, & Makino (1998). We also investigated the relationship between the core radius r_c and the scale radius r_s. As shown in Figure 5.2, the relationship between r_s and r_c is well described by $r_s = (0.26 \pm 0.01) r_c$ except for A401. A similar correlation was obtained by Ota (2000) with the *ROSAT* observations, and was noted by Makino, Sasaki, & Suto (1998) in their simulation. Note that although A401 ($z = 0.0748$) shows a symmetric X-ray surface brightness profile, there is a neighboring cluster (A399) in the $\sim 40'$ southwest direction. Whether the A401 and A399 pair is pre-merger (Fujita, Koyama, Tsuru, & Matsumoto 1996) or post-merger (Fabian, Peres, & White 1997) is still an open question. The deviation of A401 may reflect such a peculiar condition.

5.2 Mass profiles

Under the assumptions of hydrostatic equilibrium and spherical symmetry, we can obtain the total gravitating mass profile as a function of radius using Equation (2.9):

$$\begin{aligned} \frac{dP_g}{dr} &= -\mu n_g m_p \frac{d\phi}{dr} \\ &= -\mu n_g m_p \frac{GM(<r)}{r^2}. \end{aligned} \tag{5.4}$$

We derived this mass profile by two different methods in order to check its consistency. The first method employs the temperature and density profile models obtained in §5.1. Substituting Equation (5.2) and Equation (2.26) for Equation (2.9), we obtain the mass profile in an analytic form. The second method does not employ the temperature and density profile models. Instead, the mass profile is derived by approximating Equation

Table 5.4: Fitting results of the gas density profiles with the β model.

Cluster	n_{e0} [10^{-2} cm^{-3}][a]	r_c [kpc][a]	β[a]	χ^2/dof[b]	Systematic error[c]
A1060	0.68±0.05	41.9±6.8	0.36±0.03	378.0/4	0.044
A133	3.78±0.70	21.6±5.2	0.43±0.02	1567.3/4	0.086
A1795	3.69±0.42	64.2±9.0	0.58±0.03	9422.3/5	0.085
A1835	17.50±0.99	30.6±2.1	0.49±0.01	153.4/4	0.031
A2029	4.47±0.43	55.2±7.5	0.50±0.02	1461.1/4	0.057
A2052	3.81±0.26	18.8±2.1	0.41±0.01	227.9/2	0.024
A2199	2.34±0.32	56.2±10.9	0.55±0.04	3695.6/7	0.109
A2204	17.90±2.09	22.7±3.2	0.49±0.02	344.7/3	0.057
A2597	5.99±0.19	43.0±1.7	0.62±0.01	100.6/4	0.022
A401	0.60±0.02	258.1±16.1	0.58±0.03	75.5/2	0.013
A478	5.00±1.48	75.3±27.8	0.63±0.08	5260.8/6	0.215
A644	1.25±0.05	128.1±8.1	0.56±0.02	160.7/3	0.025
A85	3.27±0.37	32.7±5.2	0.40±0.02	1897.4/5	0.055
A963	2.17±0.18	109.4±14.5	0.57±0.04	154.1/2	0.042
AWM7	1.11±0.13	33.2±7.3	0.33±0.02	1699.1/4	0.056
Centaurus	7.90±1.87	4.9±1.5	0.37±0.02	4418.3/6	0.104
Hydra A	5.93±1.18	22.4±5.6	0.46±0.03	5302.3/4	0.112
MKW3S	2.59±0.24	30.7±4.4	0.42±0.02	516.1/7	0.063
NGC5044	3.11±1.61	9.6±8.0	0.43±0.10	4220.4/7	0.156
PKS0745-191	9.38±0.57	39.5±3.4	0.51±0.02	282.9/3	0.031
Sersic159-03	4.05±0.41	47.9±7.5	0.64±0.05	207.8/2	0.054
ZW3146	11.20±2.74	59.9±18.3	0.63±0.07	1427.9/2	0.111
2A0335+096	7.07±0.79	25.9±3.6	0.52±0.02	1169.1/4	0.069

[a] Errors are estimated by including a systematic error (see text).

[b] Reduced χ^2 before including a systematic error.

[c] Systematic error adopted so as to make the reduced χ^2 value unity.

Table 5.5: Fitting results of the gas density profiles with the NFW gas density model.

Cluster	n_{e0} [10^{-2} cm^{-3}][a]	r_s [kpc][a]	B[a]	χ^2/dof[b]	Systematic error[c]
A1060	0.83±0.09	145.1±48.2	5.13±1.08	565.3/4	0.078
A133	4.21±0.80	91.6±21.9	6.40±0.37	1584.3/4	0.121
A1795	4.76±0.45	252.8±37.6	8.54±0.50	6460.0/5	0.084
A1835	22.10±1.52	112.1±9.3	7.04±0.16	257.3/4	0.051
A2029	5.84±0.08	193.7±4.5	7.11±0.06	31.9/5	0.011
A2052	4.74±0.24	64.5±5.3	5.72±0.13	144.1/2	0.029
A2199	3.00±0.26	235.1±40.6	8.52±0.66	5112.0/7	0.079
A2204	21.60±3.10	89.3±14.4	7.15±0.28	557.3/3	0.10
A2597	8.11±0.62	157.4±17.6	8.94±0.38	537.9/4	0.071
A401	0.71±0.03	2842.0±664.9	19.05±10.64	97.6/2	0.035
A478	6.46±1.25	338.3±118.0	9.99±1.53	13901.8/6	0.155
A644	1.63±0.17	493.6±125.8	8.30±1.05	972.4/3	0.085
A85	3.86±0.48	122.5±21.6	5.76±0.26	2246.4/5	0.081
A963	2.76±0.13	477.2±58.5	9.07±0.57	39.3/2	0.033
AWM7	1.26±0.14	140.7±17.7	5.00±0.26	2899.1/4	0.083
Centaurus	7.79±1.75	24.7±5.5	5.72±0.23	6499.1/7	0.143
Hydra A	7.03±1.53	87.9±22.7	6.67±0.43	6555.0/4	0.151
MKW3S	3.23±0.33	106.7±20.5	5.95±0.41	608.8/7	0.083
NGC5044	3.98±0.95	34.8±15.5	6.22±0.95	3186.8/7	0.163
PKS0745-191	12.00±0.38	145.6±8.1	7.39±0.16	72.3/3	0.022
Sersic159-03	5.14±0.40	240.5±54.8	11.08±1.46	101.5/2	0.057
ZW3146	14.30±1.99	258.2±63.0	9.74±1.00	473.6/2	0.096
2A0335+096	9.23±1.30	90.5±17.3	7.41±0.47	1887.5/4	0.111

[a] Errors are estimated by including a systematic error (see text).

[b] Reduced χ^2 before including a systematic error.

[c] Systematic error adopted so as to make the reduced χ^2 value unity.

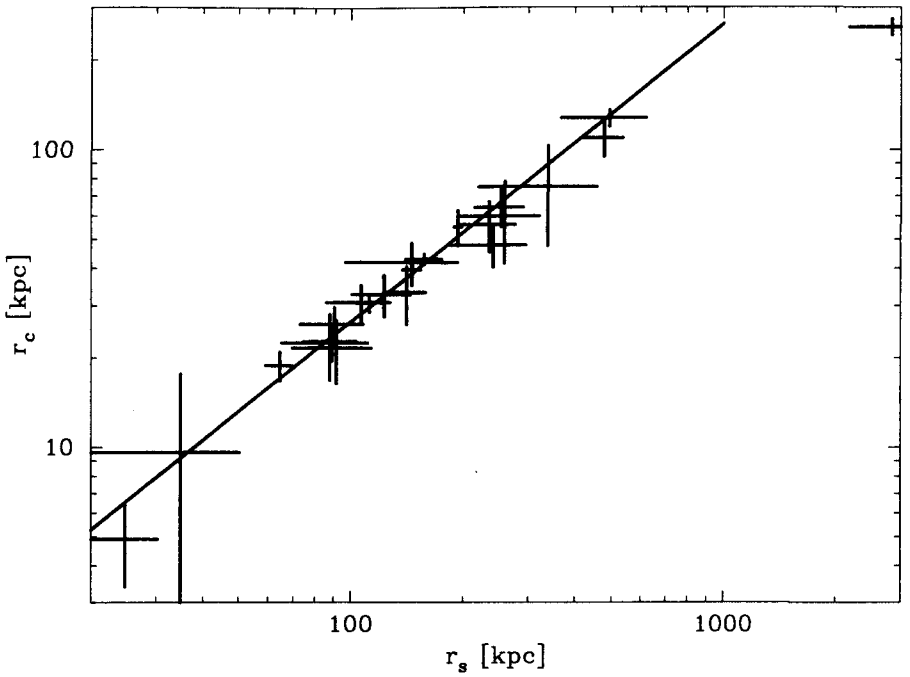

Figure 5.2: Relation between r_s and r_c. The solid line represents the best-fit relation $r_s = (0.26 \pm 0.01) r_c$ except for one deviant data of A401.

(2.9) as simple differences:

$$M(< r) \sim -\frac{1}{\mu n_g(r) m_p} \frac{r^2}{G} \frac{\Delta P(r)}{\Delta r}. \tag{5.5}$$

We calculated $\Delta P(r)/\Delta r$ as

$$\frac{\Delta P(r)}{\Delta r} = \frac{P_{i+1} - P_i}{r_{i+1} - r_i} \tag{5.6}$$

where P_i and r_i are the pressure and radius of the ith shell. The radius r and gas density $n_g(r)$ are given by $r = (r_{i+1} + r_i)/2$ and $n_g(r) = (n_{ei+1} + n_{ei})/2$, respectively.

Results of these two methods are shown in Appendix C for all the clusters. The plots also show the 1σ confidence levels for the analytic mass profile, which is derived by considering the errors of the parameters describing the temperature and density profile models. The mass profiles derived by the two different methods were consistent in most of the cases. Note that we could not constrain the 1σ confidence levels of the mass profile of A2052 due to the large uncertainty of the temperature profile. In the case that $P_{i+1} > P_i$ –, the pressure of the outer shell is larger than that of the inner shell, and the mass profile shows the negative mass $M < 0$. This is likely caused by the local temperature fluctuation intrinsic at some radius of the clusters or by systematic errors in our analysis, as described in the §4.3.3. We excluded these unphysical points in the analysis, though such points are only seen in NGC5044 (2nd point) and Centaurs (3rd point). Of the

two derivation methods, the first one using the modeled temperature and density profiles is easy to handle, but it involves sacrificing one important point of the deprojection analysis; i.e., no reliance on any particular profile models. On the other hand, the second method is more straightforward, but it suffers large error owing to local fluctuations in the temperature and density profiles. In the following analysis, we principally use the mass profiles from the second method unless noted.

5.3 Scaling of mass profiles

In the following sections, we discuss a comparison of the total mass profiles we derived with the results of CDM simulations. The total mass we dealt with included gas, stars in galaxies, and dark matter. Since clusters are dark matter dominant systems as described in Chapter 2, we neglect the contribution from masses other than dark matter, while we will examine its validity in Chapter 6. Assuming the cluster to be dominated by dark matter, the total mass profile we derived corresponds to an implicit dark matter density profile.

In Figure 5.3, we show the analytic mass profiles of 23 sample clusters in one plot, illustrating the scatters among them. CDM simulations predict that the density profiles of dark matter are universal in form across a wide range of mass scales (e.g., Navarro, Frenk, & White 1995, 1996). We scaled our analytic mass profiles with r_{200} and M_{200}, where r_{200} is the radius within which the mean halo density is 200 times the critical density of the universe, and M_{200} is the total mass enclosed within r_{200}. As shown by Navarro, Frenk, & White (1995, 1996), clusters of different mass are expected to show similar structures when scaled to such a characteristic radius and mass. For the calculation of r_{200}, we used the relation obtained from the numerical simulation by Evrard, Metzler, & Navarro (1996):

$$r_{200} = 3.690\ (T/10\mathrm{keV})^{0.5}\ (1+z)^{-1.5}\ \ [\mathrm{Mpc}], \tag{5.7}$$

where T is the emission-weighted temperature, and z is the redshift. We used the T_{average} in Table 5.1 as the emission weighted temperature. M_{200} is calculated by

$$M_{200} = \frac{4}{3}\pi(200\rho_{\mathrm{crit}}(z))\ r_{200}^3. \tag{5.8}$$

We show the scaled mass profiles in Figure 5.4. On a large scale ($r > 0.1r_{200}$), the scaled mass profiles agree with each other better than did the original mass profiles, except in the case of one deviant profile of A401. This findings suggest that the mass profiles have a similar form on a large scale; in other words, the scaling with r_{200} and M_{200} is effective at least on this scale. The standard deviation of the mass profiles is 41 % at 200 kpc

for the original mass profiles, and that for the scaled profiles is 21 % at $0.1r_{200}$, which corresponds to about 160–300 kpc. In contrast, the standard deviations on the small scale ($r < 0.1r_{200}$) are not significantly different: 55 % at 20 kpc for the original mass profiles, and 60 % at $0.01r_{200}$ for the scaled mass profiles.

When the density profile of dark matter is described with the power-law expression $\rho(r) = \rho_0(r/r_0)^\alpha$, the mass integrated over the volume is described by

$$M(< r) = \int_0^r 4\pi\rho(r')r'^2 dr' = \frac{4\pi\rho_0 r_0^3}{3-\alpha}(\frac{r}{r_0})^{3-\alpha}. \tag{5.9}$$

Therefore, when the logarithmic slope α is flatter than ($\alpha \to 0$), the integrated mass profile has a steeper slope. We overlaid the $M \propto r^{1.5}$ ($\alpha = 1.5$), $M \propto r^2$ ($\alpha = 1$) and $M \propto r^3$ ($\alpha = 0$) lines on the scaled mass profiles in Figure 5.4. It was found that the slope α was in the range of 0 to 1.5, and it was flatter (smaller) on the small scale. The slope α at the cluster center is quantitatively examined in §5.5

5.4 Comparison with theoretical models

In this section, we compare the measured mass profiles with the King and NFW profiles shown in Chapter 2. As described in §2.3.2, the King profile is an approximation of the equation of a self-gravitating sphere and is flat ($\alpha = 0$) in the central region, whereas the NFW profile, is an analytic formula obtained from CDM simulation, is cuspy ($\alpha = 1$) (see §2.3.4). We employ the discrete mass profiles, which were obtained from Equation (5.5) without using temperature and gas density profile models. The King density profile is given by

$$\rho(r) = \rho_0^{\rm King}(1 + (r/r_c)^2)^{(-3/2)},$$

where $\rho_0^{\rm King}$ is the central density and r_c is the core radius. The integrated mass profile is analytically given by Equation (2.16), to which we fit our measured mass profiles. The free parameters to be determined are $\rho_0^{\rm King}$ and r_c. On the other hand, the NFW density profile is given by Equation (2.23):

$$\rho(r) = \delta_c\rho_{\rm crit}[(r/r_s)(1 + r/r_s)^2]^{-1},$$

where

$$\delta_c = \frac{200}{3}\frac{c^3}{[\ln(1+c) - c/(1+c)]}$$

(see §2.3.4). The integrated mass profile is given by Equation (2.25), where the free parameters of the fitting are c and r_s. We limited the range of the concentration parameter $c \geq 1$ to prevent models in which the scale radius r_s was larger than r_{200}.

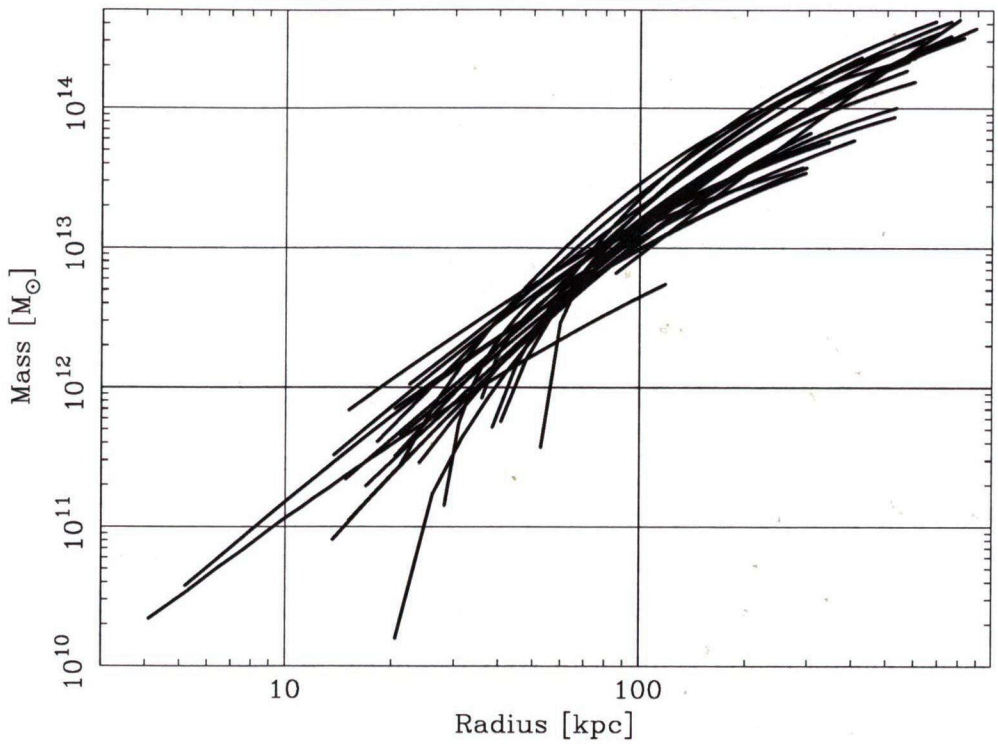

Figure 5.3: Mass profiles of 23 sample clusters obtained from the temperature and density profile models.

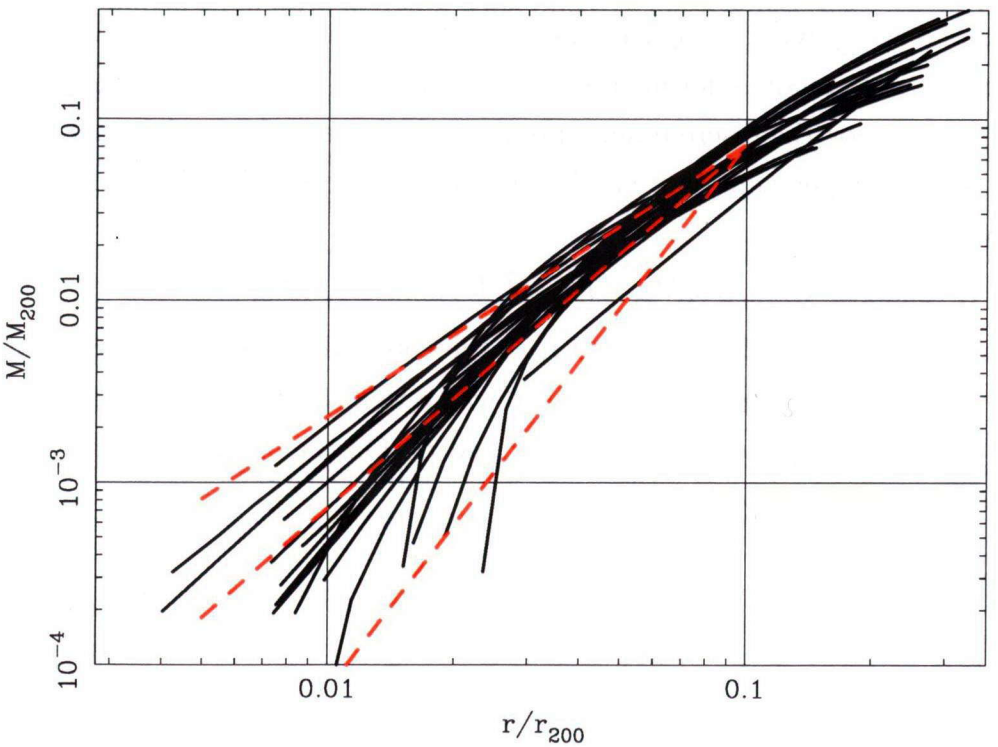

Figure 5.4: Mass profiles scaled by M_{200} and r_{200}. The red, dashed lines represent $M \propto r^{1.5}$ ($\alpha = 1.5$), $M \propto r^2$ ($\alpha = 1$) and $M \propto r^3$ ($\alpha = 0$), respectively.

The results of the fitting are summarized in Table 5.6 and Table 5.7. The best-fit mass profiles from the two density profile models are compared in Appendix D. When we consider only a statistical error for each data point of the measured mass profile, the fits are not acceptable at significance levels less than 1 % with either model, except in the case of PKS0745-191 and ZW3146 with the King profile, and in that of A2029 with the NFW profile. In addition to the fitting of the temperature and gas density profiles shown in §5.1, we assigned systematic errors of a constant fraction of the measured mass so as to obtain the reduced χ^2 of unity when the original fit is not acceptable. The parameter values and errors in Table 5.6 and Table 5.7 are those obtained considering the systematic error. Although introducing this systematic error prevented us from doing statistical tests to determine which model is preferable, some clusters showed a mass profile steeper (smaller α) than the NFW profile in the central region. This is clearly seen in A2597, PKS0745-191, ZW3146, and 2A0335.

The core radii of the King profile are in the range from 8.7 to 265.8 kpc with a median of 104.4 kpc, whereas the scale radii of the NFW profile were in the larger range from 25.0 to 4293.3 kpc, with a median of 1345.5 kpc. We compared the core radius of the gas density profile ($r_{\rm c,gas}$) in Table 5.4 with that of the mass profile ($r_{\rm c,mass}$) in Figure 5.5. The core radii of the mass profiles are systematically larger than those of the gas density profiles, suggesting that the gas is more concentrated than the total mass or dark matter. We also showed the relation of the scale radii of the gas profiles $r_{\rm s,gas}$ and those of the mass profiles in Figure 5.6.

We next compared the concentration parameters obtained from the NFW fit with those predicted by a CDM simulation. We employed a function that was derived by fitting the simulation data of Bullock et al. (2001) to approximate the concentration parameter $c_{\rm sim}$,

$$c_{\rm sim} = \frac{9}{1+z}\left(\frac{M_{\rm vir}}{1.5\times 10^{13}h^{-1}M_{\odot}}\right)^{-0.13}, \tag{5.10}$$

where $M_{\rm vir}$ is the virial mass of a cluster. In the evaluation of $c_{\rm sim}$, we used M_{200} calculated by Equation (5.8) as $M_{\rm vir}$. As shown in Figure 5.7, the numerical simulation by Bullock et al. (2001) predicted concentration parameters in the range of 4.2 to 7.2, whereas the concentration parameters observed were in the wider range of 1.00 to 15.29. Although the error for each data point is large, the concentration parameter observed is smaller than that in the CDM simulation for most of the clusters. We should note that the results of the NFW mass profile fit are consistent with previous measurements with *Chandra* by Schmidt, Allen, & Fabian (2001) (A1835; $r_{\rm s} = 640^{+210}_{-120}$ kpc and $c = 4.0^{+0.54}_{-0.64}$), by Lewis, Buote, & Stocke (2002) (A2029; $r_{\rm s} = 540 \pm 90h_{70}^{-1}$ kpc and $c = 4.1 \pm 0.8$), and by David et al. (2001) ($r_{\rm s} = 77 \pm 10h_{70}^{-1}$ kpc and $c = 12.3 \pm 0.18$) within errors.

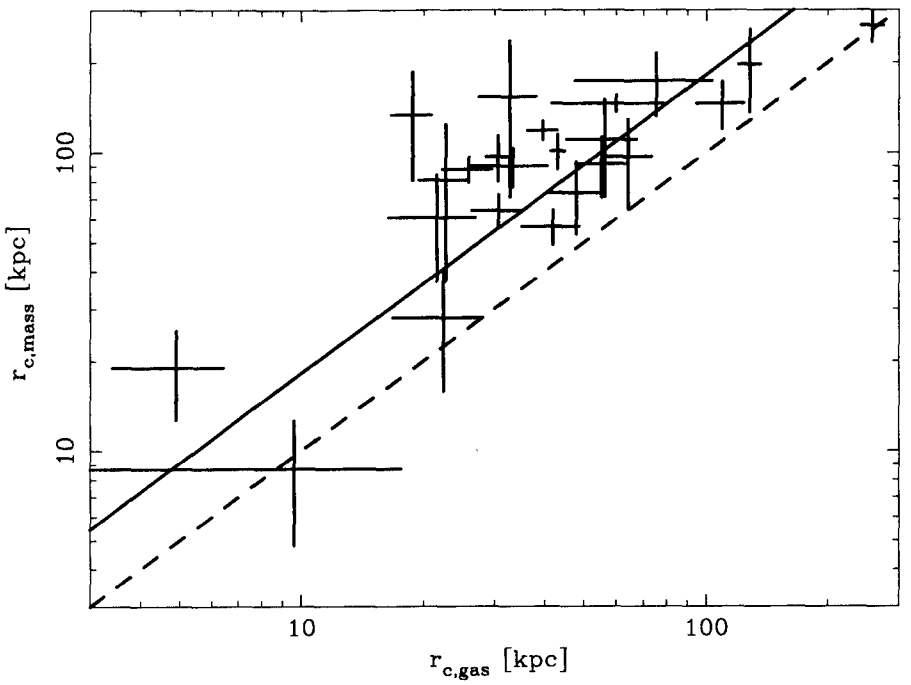

Figure 5.5: Comparison of the core radius of the gas profile and that of the mass profile. The dashed line represents $r_{c,mass} = r_{c,gas}$. The solid line represents the best-fit ($r_{c,mass} = 1.82 \pm 0.10 r_{c,gas}$).

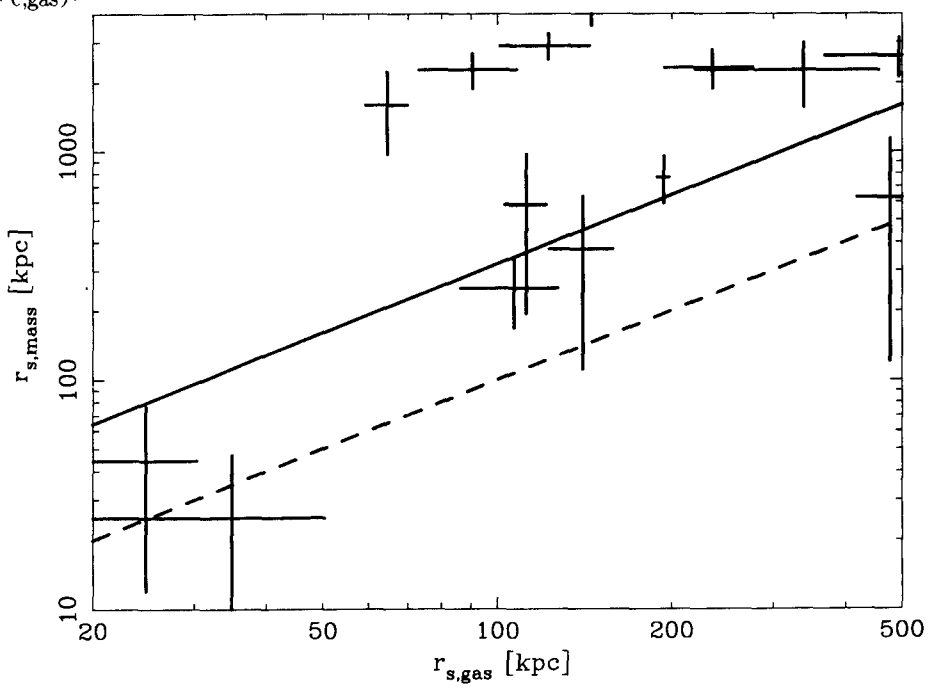

Figure 5.6: Comparison of the scale radius of the gas profile and that of the mass profile. The dashed line represents $r_{s,mass} = r_{s,gas}$. The solid line represents the best-fit ($r_{s,mass} = 3.20 \pm 0.50 r_{s,gas}$).

Table 5.6: Fitting results of the mass profiles with the King model.

Cluster	$\rho_0^{\rm King}$ [$M_\odot$ pc^{-3}][a]	r_c [kpc][a]	χ^2/dof[b]	Systematic error[c]
A1060	$1.01\pm2.19\times10^{-3}$	56.6±7.4	117.51/4	0.193
A133	$7.69\pm4.63\times10^{-3}$	60.5±23.5	101.53/4	0.430
A1795	$5.12\pm2.57\times10^{-3}$	96.9±32.4	425.34/5	0.481
A1835	$1.07\pm2.87\times10^{-3}$	96.8±16.9	14.22/4	0.242
A2029	$1.01\pm3.43\times10^{-3}$	91.6±20.9	43.02/5	0.260
A2052	$2.65\pm1.05\times10^{-3}$	133.4±52.8	267.00/2	0.460
A2199	$3.79\pm1.73\times10^{-3}$	110.7±39.5	110.43/7	0.415
A2204	$1.06\pm7.72\times10^{-3}$	80.8±43.6	48.21/3	0.553
A2597	$5.77\pm1.08\times10^{-3}$	101.0±13.2	27.57/4	0.194
A401	$1.47\pm2.29\times10^{-4}$	265.8±31.1	22.60/2	0.110
A478	$3.62\pm1.18\times10^{-3}$	173.9±41.3	93.79/6	0.406
A644	$2.18\pm9.62\times10^{-4}$	197.4±60.7	64.83/3	0.416
A85	$2.87\pm1.99\times10^{-3}$	153.8±82.8	116.91/5	0.432
A963	$3.81\pm1.12\times10^{-3}$	146.1±26.4	4.46/2	0.186
AWM7	$4.64\pm1.09\times10^{-3}$	90.1±13.4	57.98/4	0.241
Centaurus	$4.78\pm2.91\times10^{-2}$	19.0±6.3	580.93/5	0.571
Hydra A	$4.15\pm3.72\times10^{-2}$	28.0±12.1	481.84/4	0.505
MKW3S	$1.16\pm2.34\times10^{-3}$	63.9±8.1	30.22/7	0.165
NGC5044	$1.07\pm9.63\times10^{-2}$	8.7±3.9	185.19/6	0.344
PKS0745-191	$7.18\pm7.88\times10^{-4}$	118.7±8.6	4.09/3	...
Sersic159-03	$5.86\pm2.05\times10^{-3}$	73.3±19.9	17.94/2	0.282
ZW3146	$5.83\pm6.49\times10^{-4}$	146.2±9.2	0.03/2	...
2A0335+096	$5.33\pm6.71\times10^{-4}$	87.9±8.4	20.19/4	0.157

[a] Errors are estimated by including a systematic error (see text).

[b] Reduced χ^2 before including a systematic error.

[c] Systematic error adopted so as to make the reduced χ^2 value of unity.

Table 5.7: Fitting results of the mass profiles with the NFW model.

Cluster	c^a	r_s [kpc]^a	χ^2/dof^b	Systematic error^c
A1060	5.63±4.07	142.3±145.2	143.0/4	0.511
A133	3.52±2.46	313.2±335.5	37.2/4	0.360
A1795	3.17±2.28	439.2±479.4	211.0/5	0.442
A1835	3.34±1.40	582.9±387.9	291.0/4	0.319
A2029	3.04±0.48	768.0±178.8	7.0/4	...
A2052	1.00±2.76	1597.3±627.2	453.1/2	0.710
A2199	1.00±1.11	2323.7±447.2	41.9/7	0.444
A2204	1.55±11.86	2198.5±17554.4	9.3/3	0.433
A2597	1.08±12.64	2299.1±6777.9	64.8/4	0.431
A401	1.49±9.83	1446.1±6614.5	21.3/2	0.503
A478	1.00±1.05	2268.6±707.7	106.2/5	0.685
A644	1.00±6.23	2629.6±504.7	71.0/3	0.447
A85	1.00±2.80	2898.9±370.1	98.3/5	0.326
A963	2.72±1.51	627.6±507.3	11.7/2	0.284
AWM7	3.15±1.47	372.1±261.6	131.9/4	0.359
Centaurus	12.11±6.42	44.3±32.3	613.1/5	0.583
Hydra A	14.52±20.68	50.0±89.2	296.0/4	0.500
MKW3S	5.00±1.07	250.8±82.6	27.6/5	0.180
NGC5044	15.29±9.59	25.0±21.9	87.4/6	0.261
PKS0745-191	1.00±4.77	4293.3±733.3	30.0/3	0.361
Sersic159-03	1.51±5.48	1267.7±4728.8	19.5/2	0.307
ZW3146	1.59±1.55	1832.3±2946.3	16.6/2	0.300
2A0335+096	1.00±5.90	2276.3±393.8	152.0/4	0.418

[a] Errors are estimated by including a systematic error (see text).

[b] Reduced χ^2 before including a systematic error.

[c] Systematic error adopted so as to make the reduced χ^2 value unity.

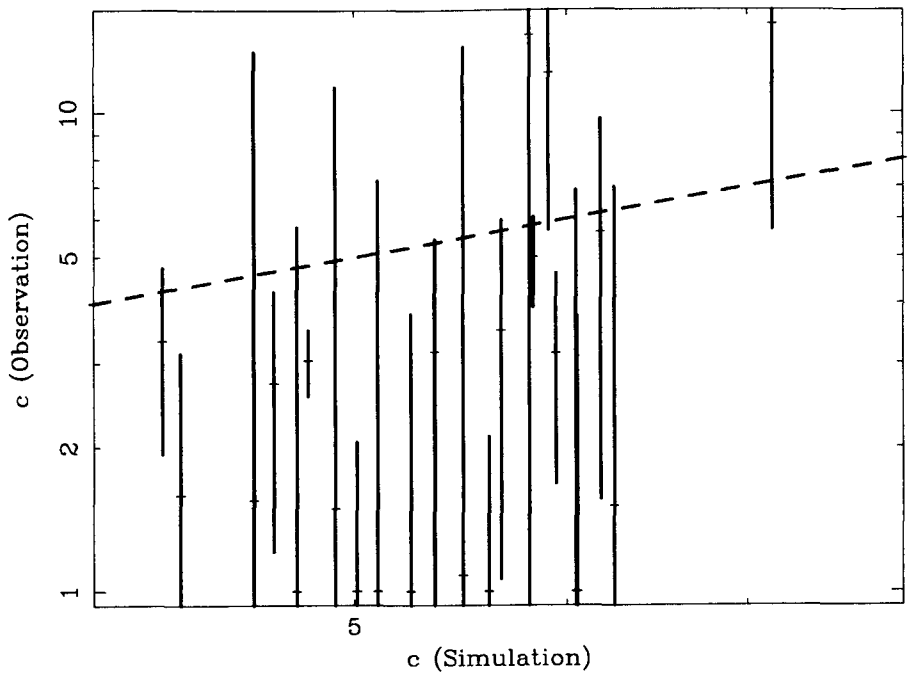

Figure 5.7: Concentration parameters predicted by the numerical simulation v.s. those we measured. The dashed line represents $c_{\rm sim} = c_{\rm obs}$.

5.5 Inner slope of dark matter distribution

As described in Chapter 2, the shape of the dark matter distribution near the center of a cluster is sensitive to the theoretical models adopted. In this section, we focus on the observed shape of the total mass distribution in terms of the slope of the density profile at the inner part of a cluster. The inner slope of the density profile is obtained by fitting the total mass profile we obtained with a model mass profile calculated from an assumed density profile. Although we employed the King and NFW profiles as density profile models in the previous section, a more generalized form is used in this section. That form was

$$\rho(r) = \frac{\rho_0}{(r/r_{\rm s})^{\alpha}(1+(r/r_{\rm s}))^{(3-\alpha)}}, \tag{5.11}$$

where ρ_0 is the central density, $r_{\rm s}$ is its scale radius, and α is the asymptotic slope of the profile at small radii. This form of density profile requires numerical integration to derive the integrated mass profile.

The asymptotic slope α in Equation (5.11) can be used as the inner slope. However, it was found that the α and the scale radius $r_{\rm s}$ are coupled strongly, and therefore difficult to determine independently. Thus, we focus on the slope of the density profile at a finite

radius and used it as the inner slope. The slope at a radius r_0, $\alpha_0(r_0)$ is given by

$$\alpha_0(r_0) \equiv -\frac{d\ln\rho(r)}{d\ln r} \mid_{r=r_0} . \tag{5.12}$$

Using Equation (5.11), we get

$$\alpha_0(r_0) = \frac{(\alpha + (r_0/r_s))}{(1 + (r_0/r_s))}. \tag{5.13}$$

We employ $\alpha_0(r_0)$ instead of α, in addition to ρ_0 and r_s, as a free parameter of the fitting. We fixed r_0 to $0.02r_{200}$, which corresponds to about 40 kpc. The choice of r_0 is not trivial, but we fix this value so that the radius is appropriate for a comparison of the theoretical models and is covered by observed data points in the mass profile. Nevertheless, A401, A644, and A963, due to a lack of data points within $0.02r_{200}$, were discarded from the following analysis.

The results of the fitting are summarized in Table 5.8, and the best-fit values and errors of the inner slope $\alpha_0(r_0)$ are plotted in Figure 5.8. We also show the total mass profiles with best-fit parameters for the general form of the density profile in Appendix E. The inner slope α_0 spans a wide range with $0 \leq \alpha_0 \leq 2.3$. We found that the 90% upper bound of α was lower than unity for 6/20 ($\sim$ 41 %) clusters (A2052, A2597, A478, PKS0745-191, ZW3146, and 2A0335+096), suggesting that the dark matter distribution in a significant fraction of clusters was flatter than that in CDM halo models such as the NFW profile or the Moore profile.

5.6 Examination of the systematic effects

We have demonstrated that the inner slope α_0 shows a large scatter and is less than unity for 30% of the clusters in our sample. Before discussing these results in greater detail, we would like to address their validity and the systematic effects that may affect the measured inner slope from various points of view.

The key assumptions of our analysis are hydrostatic equilibrium of the gas and spherical symmetry. Although the hydrostatic equilibrium assumption is difficult to confirm observationally, deviation from the spherical symmetry projected on the sky is measurable in terms of eccentricity or substructures of the X-ray emission. We evaluated those systematic effects by examining the possible dependence of the deviations from the spherical symmetry on the inner slope α_0. We also assume that the hot gas is in the single phase (i.e., single temperature at one radius). However, there are indications that some clusters have two-phase gas with different temperatures. Although examination of the two-temperature model for all the sample clusters is beyond the scope of this paper, we

Table 5.8: Fitting results of the mass profile with the general form of density profile given by Equation (5.11). The errors are 90 % confidence intervals. ρ_0 and r_s

Cluster	ρ_0 $[M_\odot$ pc$^{-3}]^a$	r_s [kpc]^a	$\alpha_0(0.02r_{200})$ ^{a}	χ^2/dof^b	Systematic error^c
A1060	12.5±25.7	6.0±4.2	1.17±0.38	120.3/3	0.225
A133	0.87±3.15×10^{-5}	3483.6±6825.6	1.34±0.34	31.8/3	0.398
A1795	0.89±2.65× 10^{-5}	4171.5±8738.0	1.34±0.35	194.2/4	0.482
A1835	0.14±1.45	51.1±200.1	0.81±0.47	13.9/3	0.278
A2029	0.35±4.33× 10^{-3}	760.0±8648.0	1.20±0.45	7.0/3	...
A2052	1.43±9.07× 10^2	3.4±8.1	-0.14±0.94	176.4/1	0.524
A2199	0.61±0.51× 10^{-2}	163.3±8.2	0.64±0.50	36.8/6	0.440
A2204	0.99±10.7× 10^{-5}	10671.3±67949.5	1.16±0.50	19.0/2	0.525
A2597	0.84±7.98	21.8±76.6	0.52±0.33	20.9/3	0.192
A478	5.36±16.2× 10^2	3.1±3.5	0.17±0.46	23.8/4	0.308
A85	0.64±0.16× 10^{-4}	2602.0±66453.9	0.99±0.37	95.6/4	0.365
AWM7	13.3±45.2	7.1±8.1	0.48±0.57	70.7/3	0.290
Centaurus	0.53±3.04	10.0±20.8	2.28±0.46	549.7/4	0.640
Hydra A	0.10±0.48× 10^{-4}	1203.8±2394.9	1.85±0.50	237.3/3	0.556
MKW3S	0.17±0.50× 10^{-1}	86.4±101.8	1.14±0.14	17.1/4	...
NGC5044	0.25±0.61× 10^{-5}	1812.0±2488.6	1.75±0.21	32.8/5	0.217
PKS0745-191	3.12±3.28	17.4±6.6	0.68±0.18	2.3/2	...
Sersic159-03	0.25±0.09× 10^{-1}	64.5±25.0	0.71±0.58	15.1/1	0.378
ZW3146	0.10±0.04	69.4±9.0	0.19±0.20	0.3/1	...
2A0335+096	1.44±9.11	15.4±35.3	0.56±0.10	11.9/3	...

[a] Errors are estimated by including a systematic error (see text).

[b] Reduced χ^2 before including a systematic error.

[c] Systematic error adopted so as to make the reduced χ^2 value unity.

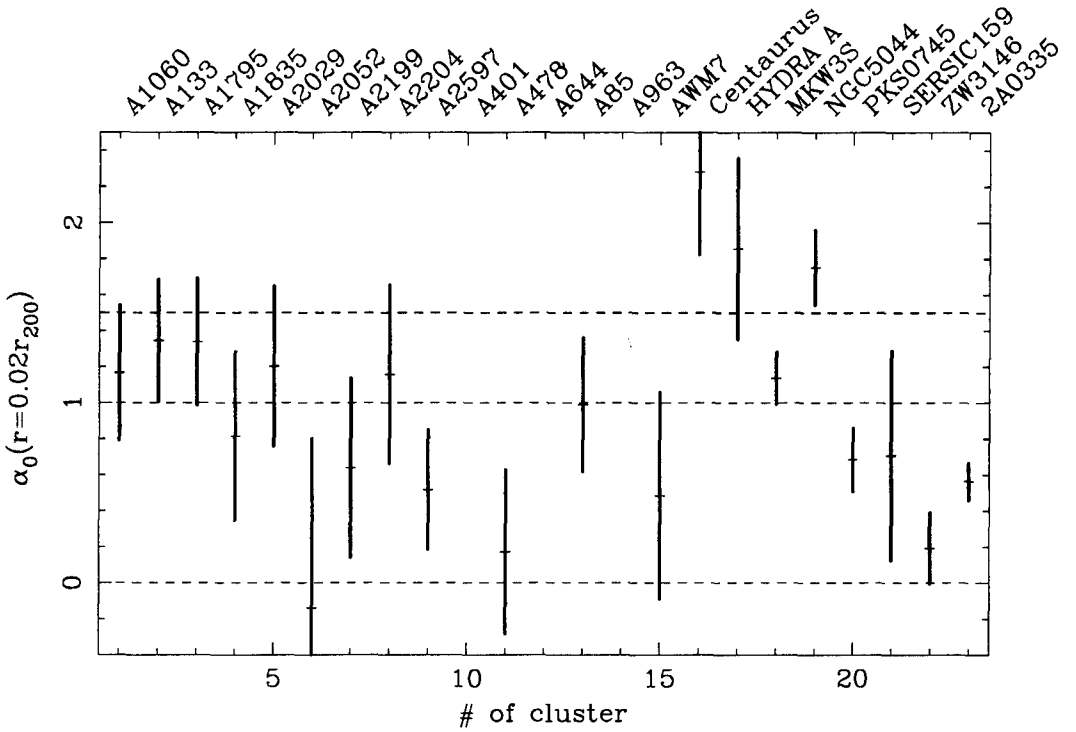

Figure 5.8: Values of the Inner slope α_0 at the radius of $0.02r_{200}$ for 20 clusters in Table 5.8. A401, A644, and A963 were removed due to a lack of data points within $0.02r_{200}$. The horizontal dashed lines represent $\alpha = 1.5$ (Moore), $\alpha = 1.0$ (NFW), and $\alpha = 0.0$ (King). Error bars are shown at 90 % confidence level.

apply the model to one cluster. Even when the spherical symmetry holds, observational uncertainty in determining the center of a cluster remains. In this section, we also evaluate this uncertainty. Furthermore, we compare our results with those in previous reports for some clusters included in our sample.

5.6.1 Center position

We can define three types of positions as the center of a cluster: (1) the X-ray emission peak of cluster hot gas; (2) the X-ray centroid; and (3) the position of the Brightest Cluster Galaxy (BCG). We chose the X-ray emission peak as the center of the annuli to extract spectra (see §4.3.1). Since these three positions are slightly different, the selection of the center position may affect our results.

We first examined the position of the BCG in our sample clusters. The BCG is defined as the brightest galaxies among the member galaxies of a cluster. Since the BCGs are usually located at the center of a cluster and have velocities very near the mean velocity of galaxies in the cluster, they are considered to sit at the bottom of the cluster gravitational potential well.

In Table 5.9, we show the position of the BCG in 23 sample clusters. The positions of BCGs were taken from the NASA/IPAC Extragalactic Database (NED)[1]. We calculated the offset between the X-ray peak shown in Table 4.3 and the position of the BCG. When the offset was larger than or comparable to the radius of the innermost annulus, the temperature or density profiles will be affected by the selection of the center. In Figure 5.9, the offsets of the BCG are plotted against the radii of the innermost annulus. The offsets of the BCG are smaller than the radius of the innermost annulus ($\sim$ 30 % at the maximum) except for 2A0335, suggesting that the difference in cluster center between these two definitions did not affect our results significantly.

Katayama et al. (2003) found that the offset of the BCG is correlated with the virial density $\rho_{\rm vir}$, which represents the formation epoch of a cluster. The small offsets of our sample clusters thus suggest that these clusters are a well relaxed system (see also Hashimotodani 1999).

We next examined the offset between the X-ray peak and the X-ray centroid. To derive the X-ray centroid, we used the X-ray images in which point sources were removed following the procedures shown in §4.3.1. We replaced each embedded source with the local diffuse X-ray emission surrounding the source by using the CIAO task *dmfilth*. This task replaces the counts within the source regions with the values sampled from the

[1]http://nedwww.ipac.caltech.edu

Table 5.9: Positions and optical magnitudes of the BCG of 23 sample clusters

Cluster	BCG position		Offset[a]		m_B^b	Name of the BCG[c]
	ra	dec	["]	[kpc]		
A1060	159.179	-27.527	6.5	2.3	12.08	NGC 3311
A133	15.674	-21.882	4.4	6.7	14.27	ESO 541- G 013
A1795	207.218	26.593	1.8	2.9	14.67	CGCG 162-010
A1835	210.258	2.879	2.3	11.3	···	MAPS-NGP O_560_1447890
A2029	227.734	5.745	6.5	12.8	14.30	IC 1101
A2052	229.185	7.021	0.5	0.4	13.76	UGC 09799
A2199	247.159	39.551	0.6	0.5	···	NGC 6166 NED01
A2204	248.196	5.576	1.8	6.3	···	TXS 1630+056
A2597	351.333	-12.124	1.8	3.7	···	NPM1G -12.0625
A401	44.741	13.583	7.4	14.1	···	UGC 02450
A478	63.355	10.465	2.9	6.4	···	PGC 014685
A644	124.356	-7.512	6.4	11.6	···	PGC 023233
A85	10.459	-9.303	3.6	5.3	14.71	MCG -02-02-086
A963	154.265	39.047	2.0	8.7	···	2MASXi J1017036+390249
AWM7	43.615	41.578	3.0	1.5	13.03	NGC 1129
Centaurus	192.205	-41.311	6.5	2.0	10.85	NGC 4696
Hydra A	139.524	-12.096	1.7	2.5	13.46	MCG -02-24-007
MKW3S	230.466	7.709	0.4	0.5	14.68	NGC 5920
NGC5044	198.850	-16.385	0.4	0.9	···	NGC5044
PKS0745-191	116.881	-19.294	2.3	5.7	···	PKS 0745-19
Sersic159-03	348.495	-42.727	6.2	9.5	14.34	PGC 070747
ZW3146	155.915	4.187	2.6	13.9	···	ZwCl 1021.0+0426
2A0335+096	54.669	9.970	13.9	13.3	···	PGC 013424

[a] Offset between the X-ray peak and the BCG.

[b] B-band magnitude taken from "The Third Reference Catalogue of Bright Galaxies" by de Vaucouleurs et al. (1991).

[c] Name in the NED.

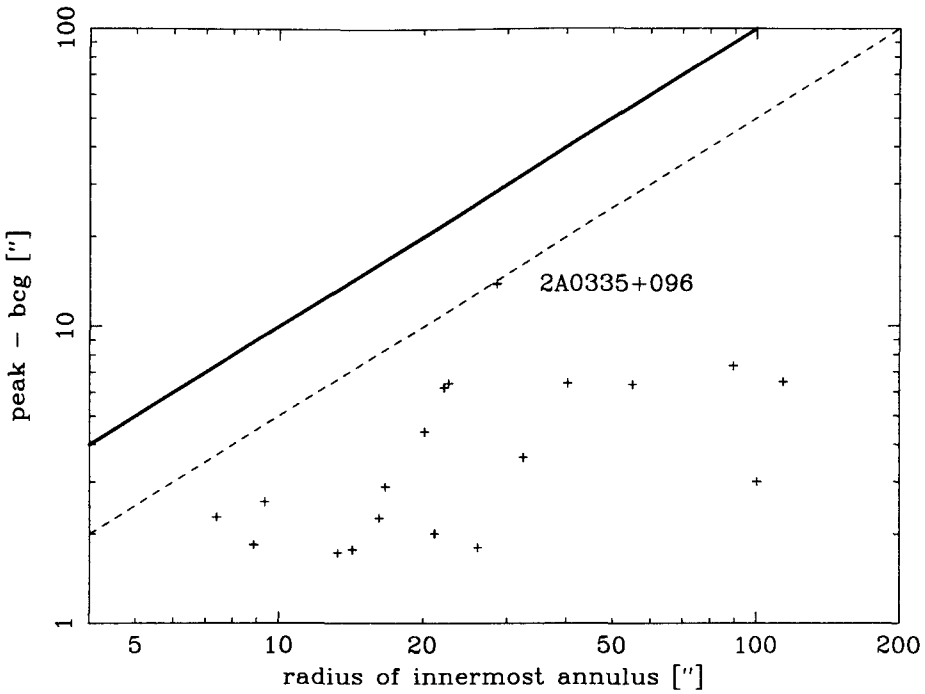

Figure 5.9: Radius of the innermost annulus vs. offset between the X-ray peak and the BCG. The dashed line represents 50 % of the radius of the innermost annulus.

background regions. As shown in Appendix A, the ACIS CCDs do not cover the entire X-ray emission for most clusters. We thus define the X-ray centroid within a circular region that is centered on the X-ray peak and has a radius that is tangent to the detector edge. The X-ray centroid, offset, and radius used in deriving the centroid are summarized in Table 5.10. The offsets between the X-ray peak and the X-ray centroid are plotted against the radii of the innermost annulus in Figure 5.10. The offsets of the X-ray centroid are slightly larger than the offsets of the BCG but are smaller than the radii of the innermost annulus. The offset is at most 74 % (for A644) of the radius of the innermost annulus, suggesting that the difference in these definitions of a cluster center does not significantly affect the results.

To estimate the effect of cluster center selection on the resultant mass profiles, we explicitly derived the mass profiles of PKS0745-191 (offset $= 8.5 \pm 0.2$) and 2A0335+096 (offset $= 13.5 \pm 0.2$) from the spectra extracted from the concentric annuli centered on the X-ray centroid. The mass profiles derived from the X-ray peak and the X-ray centroid are compared in Figure 5.11. The two mass profiles are consistent within the error bars. In the innermost radius, the differences between these two mass profiles are 15 % and 26 % for PKS0745-191 and 2A0335+096, respectively. In Table 5.11, we show the inner slope α_0 at a radius of r_0 for these mass profiles. The inner slopes are also consistent within

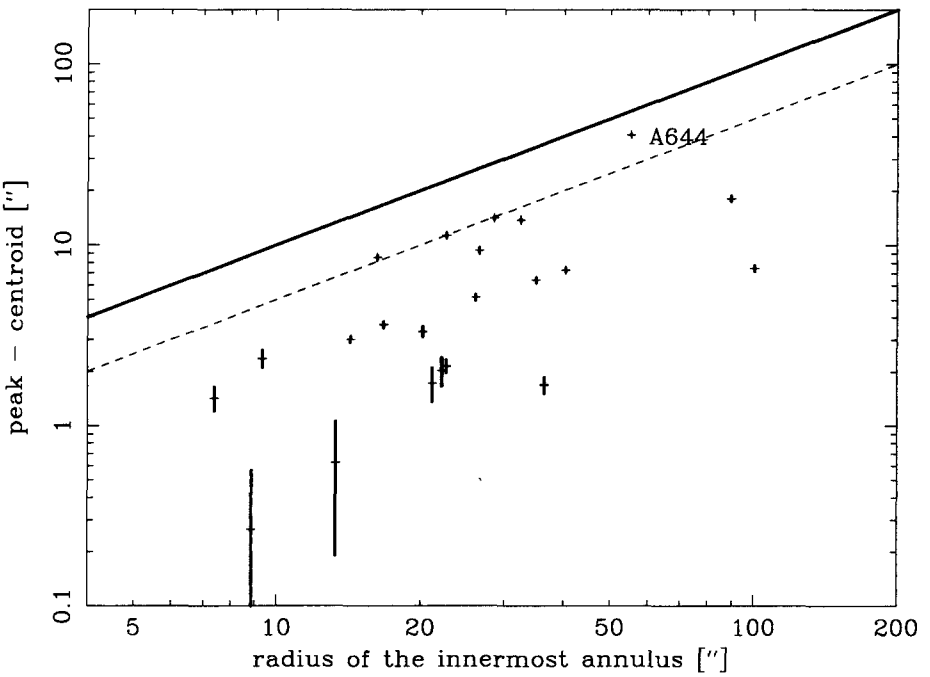

Figure 5.10: Radius of the innermost annulus vs. offset between the X-ray peak and the X-ray centroid. The dashed line represents 50 % of the radius of the innermost annulus.

the 90 % confidence error. We thus conclude that the selection of the cluster center did not significantly affect our results of the inner slope.

5.6.2 Spherical symmetry

As described in §4.2, we identified by eye a number of spherically symmetric clusters to use as our sample clusters. To quantify the spherical symmetry, we measured the ellipticity (ϵ) and the position angle (PA) from the projected X-ray image. We used an iterative moment technique derived from the treatment of the dispersion ellipse of the bivariate normal frequency function of position vectors used by Carter & Metcalfe (1980). We first calculated the moments of the observed X-ray images. From an image of P pixels having n_i counts in pixel i, we computed the moment

$$\mu_{mn} = \frac{1}{N}\sum_{i=1}^{P} n_i (x_i - \bar{x})^m (y_i - \bar{y})^n \quad (m, n \leq 2), \tag{5.14}$$

where $N = \sum_{i=1}^{P} n_i$, and $(\bar{x},\bar{y})$ is the centroid. Then ellipticity ϵ is

$$\epsilon = 1 - \frac{\Lambda_-}{\Lambda_+}, \tag{5.15}$$

Table 5.10: Centroid positions of the 23 sample clusters.

Cluster	Centroid position		Offset[a]		Radius[b]
	ra	dec	["]	[kpc]	["]
A1060	159.174	-27.535	8.0 ± 0.5	2.9±0.2	216.8
A133	15.674	-21.881	3.3 ± 0.2	5.0±0.3	157.5
A1795	207.219	26.594	5.1 ± 0.2	8.4±0.3	196.8
A1835	210.258	2.878	5.3 ± 0.2	26.4±1.1	196.8
A2029	227.733	5.744	2.1 ± 0.2	4.2±0.4	196.8
A2052	229.185	7.021	1.7 ± 0.2	1.6±0.2	157.4
A2199	247.158	39.550	6.4 ± 0.2	5.5±0.2	196.8
A2204	248.196	5.576	0.3 ± 0.3	0.9±1.0	196.8
A2597	351.332	-12.125	3.0 ± 0.1	6.3±0.2	78.7
A401	44.740	13.576	18.1 ± 0.7	34.7±1.2	393.6
A478	63.355	10.466	3.6 ± 0.1	8.0±0.3	196.8
A644	124.354	-7.515	40.7 ± 0.4	74.1±0.8	354.2
A85	10.461	-9.306	13.7 ± 0.3	20.2±0.4	275.5
A963	154.265	39.047	1.7 ± 0.4	7.4±1.6	196.8
AWM7	43.617	41.580	7.4 ± 0.3	3.6±0.1	236.2
Centaurus	192.202	-41.310	7.3 ± 0.2	2.3±0.1	196.8
Hydra A	139.523	-12.096	0.6 ± 0.4	0.9±0.6	393.6
MKW3S	230.464	7.706	11.3 ± 0.3	13.7±0.4	354.2
NGC5044	198.850	-16.388	9.3 ± 0.3	20.8±0.6	196.8
PKS0745-191	116.881	-19.296	8.5 ± 0.2	21.5±0.5	177.1
Sersic159-03	348.494	-42.727	2.0 ± 0.4	3.1±0.6	196.8
ZW3146	155.915	4.187	2.4 ± 0.3	12.7±1.4	196.8
2A0335+096	54.669	9.970	14.1 ± 0.2	13.5±0.2	236.2

[a] Offset between the X-ray peak and the X-ray centroid.

[b] Radius used to derive the centroid.

Table 5.11: Inner slope α_0 of mass profiles derived from the X-ray peak and the X-ray centroid for PKS0745-191 and 2A0335+096.

Cluster	X-ray peak	X-ray centroid
PKS0745-191	0.68±0.18	0.72±0.25
2A0335+096	0.56±0.10	0.35±0.18

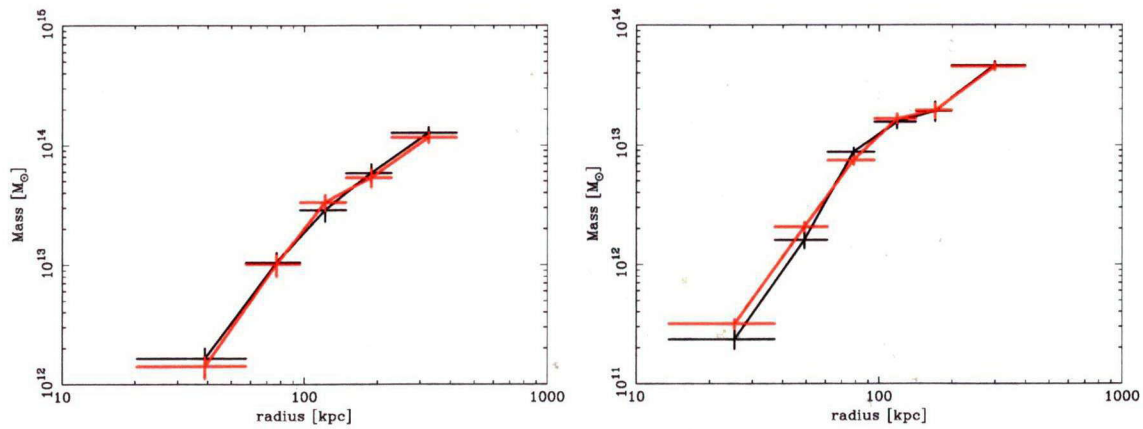

Figure 5.11: Comparison of the mass profiles of PKS0745-191 (**left**) and 2A0335+096 (**right**) derived from the X-ray peak (red) and X-ray centroid (black).

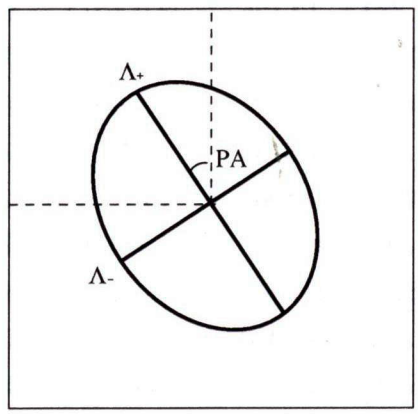

Figure 5.12: Definition of the ellipticity and position angle.

and the position angle of the major axis measured north through east in celestial coordinates (see Figure 5.12) is

$$PA = \tan^{-1}\left(\frac{\mu_{11}}{\Lambda_+^2 - \mu_{02}}\right) + \frac{\pi}{2}, \tag{5.16}$$

where $\Lambda_\pm$ ($\Lambda_+ \geq \Lambda_-$) are the positive roots of the quadratic equation

$$\begin{vmatrix} \mu_{20} - \Lambda^2 & \mu_{11} \\ \mu_{11} & \mu_{02} - \Lambda^2 \end{vmatrix} = 0. \tag{5.17}$$

As in the case of the determination of the X-ray centroids, we used the X-ray images from which point sources were removed and replaced with local diffuse X-ray emission surrounding the source. We also employed the *ROSAT* images to determine the ellipticities and position angles in outer regions of clusters. From the *ROSAT* image, the point sources were removed but the holes were not replaced with the background. We show the

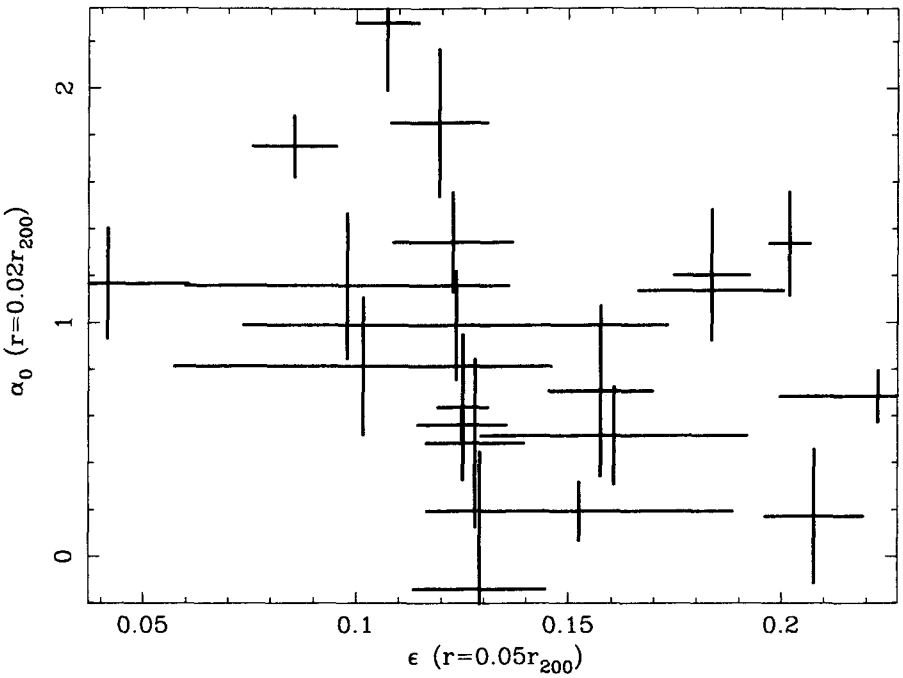

Figure 5.13: Ellipticity ϵ vs. central slope α_0. The errors are 1σ (68.3 %) confidence level.

ellipticities and position angles as a function of the radius scaled with r_{200} in Appendix F. The ellipticities and position angles derived from the *Chandra* and *ROSAT* images are almost consistent.

In Table 5.12, we show the ellipticity averaged over all radii, which includes that at $r = 0.05r_{200}$ and at $r = 0.1r_{200}$. The averaged ellipticities range from 0.042 to 0.223 with a median of 0.139. The ellipticity increases in the outer region for some clusters (A1795, A2029, A478, A644, AWM7, MKW3S, and Sersic159-03). We consider that if the ellipticity of a cluster affects the inner slope α_0, the ellipticity ϵ and the inner slope α will show some kind of relation. However, the plot in Figure 5.13 shows no correlation between the ellipticity ϵ and the central slope α_0 (the correlation coefficient is -0.31). We therefore conclude that there was no evidence that deviation from spherical symmetry affects the results on the inner slope α_0, although we obtain no evidence regarding symmetry along the line of sight.

5.6.3 Central structure

As described in §2.4.2, recent *Chandra* observations have revealed remarkable structures in the hot gas of the central region of some cooling flow clusters. These structures may have observably affected the temperature and gas density in our measurement. Furthermore, if these structures indicate a break of hydrostatic equilibrium, they may systematically

Table 5.12: Ellipticities of the sample clusters (averaged, $r = 0.05r_{200}$, and $r = 0.1r_{200}$).

Cluster	ϵ (averaged)[a]	$\epsilon(r = 0.05r_{200})$	$\epsilon(r = 0.1r_{200})$
A1060	0.042±0.019	0.036±0.016	0.036±0.008
A133	0.123±0.014	0.134±0.007	0.131±0.006
A1795	0.202±0.005	0.211±0.006	0.242±0.003
A1835	0.102±0.044	0.129±0.009	0.112±0.009
A2029	0.184±0.009	0.188±0.006	0.247±0.003
A2052	0.129±0.016	0.132±0.006	0.145±0.028
A2199	0.125±0.006	0.133±0.005	0.159±0.004
A2204	0.098±0.038	0.096±0.014	0.087±0.016
A2597	0.161±0.031	0.163±0.009	0.188±0.023
A401	0.165±0.017	0.131±0.014	0.188±0.010
A478	0.208±0.012	0.231±0.005	0.260±0.003
A644	0.169±0.020	0.127±0.007	0.189±0.006
A85	0.123±0.050	0.156±0.007	0.111±0.004
A963	0.095±0.054	0.093±0.021	0.120±0.010
AWM7	0.128±0.011	0.155±0.003	0.208±0.016
Centaurus	0.107±0.007	0.114±0.008	0.110±0.010
Hydra A	0.120±0.011	0.068±0.010	0.135±0.006
MKW3S	0.183±0.017	0.186±0.006	0.224±0.006
NGC5044	0.085±0.010	0.102±0.018	0.122±0.013
PKS0745-191	0.223±0.023	0.248±0.008	0.274±0.005
Sersic159-03	0.157±0.012	0.173±0.009	0.192±0.010
ZW3146	0.153±0.036	0.175±0.010	0.217±0.010
2A0335+096	0.125±0.010	0.126±0.006	0.122±0.006

Table 5.13: Remarkable structures in the central region of the sample clusters in literatures.

Cluster	Structure	Reference
A133	tongue	Fujita et al. (2002)
A1795	filament	Fabian et al. (2001)
A2052	holes	Blanton, Sarazin, McNamara, & Wise (2001)
A2199	depression	Johnstone, Allen, Fabian, & Sanders (2002)
A2597	cavities	McNamara et al. (2001)
Centaurus	plume	Sanders & Fabian (2002)
Hydra A	depression	McNamara et al. (2000)
NGC5044	hole	Buote et al. (2002)
MKW3S	filament & depression	Mazzotta et al. (2002)
2A0335+096	cavity	in this work

have affected the mass profile we obtained. In Appendix G, we show the central $5' \times 5'$ X-ray images of our sample clusters. For 10 clusters in our sample (A133, A1795, A2052, A2199, A2597, Centaurus, Hydra A, NGC5044, MKW3S, and 2A0335+096), the presence of central X-ray structures such as a cavity, hole, or plume has been reported with *Chandra* observations in the literature. We found a structure like a cavity in the X-ray image of 2A0335+096. This finding might be associated with the radio structure found by Sarazin, Baum, & O'Dea (1995).

In Figure 5.14, we show the inner slope α_0 again, indicating 10 clusters for which the central structure has been found by open circles. It is found that the three clusters in which α_0 is as steep as 2 have central structures, and the range of α_0 becomes narrower if we neglect them. However, the distribution of α_0 from 0 to 1.2 is similar for clusters with and those without central structures, though this is difficult to conclude quantitatively. Note that some of the central structures, such as those in A133, A2597, MKW3S, and 2A0335+096, are small enough to be removed from the analysis in the same way the point sources were. In order to evaluate the observational effect of these structures, we removed the region of these structures from those clusters and confirmed that the mass profiles were not significantly affected.

5.6.4 Test of the two temperature model

We have assumed that hot gas is in the single phase and has a single temperature within one spherical shell. However, for some clusters, the spatial co-existence of two distinct plasma components has been reported by the *ASCA* and *ROSAT* observations. Ikebe et al.

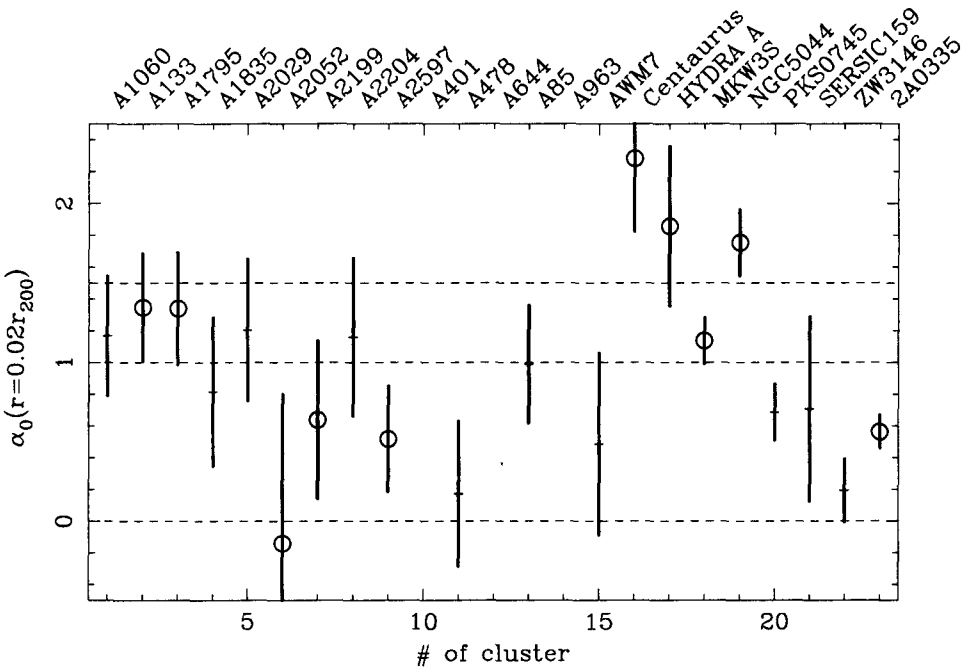

Figure 5.14: Central slope α_0 of mass profiles. The circles indicate 10 clusters n in the literatures to have the central structure (see Table 5.13).

(1995, 1999) found that the hot gas in the Centaurus cluster consists of two components, the cool component of $kT_c = 1.4 \pm 0.2$ keV and the hot component of $kT_h = 3.9 \pm 0.1$ keV, and that contributions of these two components vary as a function of radius. Similar results have been reported for the Hydra A cluster (Ikebe et al. 1997) and A1795 (Xu et al. 1998). Ikebe et al. (1999) also showed that the potential profile of the Centaurus cluster is deeper at the center than expected from the King profile, and is consistent with the NFW model. Although it is not certain that the two temperature model is better than the single temperature model for most of the clusters, we examine how our results would be affected if we employ the two temperature model.

We first apply the two temperature model to the *Chandra* data of the Centaurus cluster, for which Ikebe et al. (1999) presented the results from the *ASCA* and *ROSAT* data. In Figure 5.15, we present the spectra and the best-fit single temperature models for all annuli, and those of the innermost annulus. Large residuals remain below 1.5 keV, suggesting that more than one component is required. We then applied two kinds of two temperature models. In one model, we fixed T_c and T_h for all annuli. We call this model the "two temperature fixed model". In the other model, we fixed only T_c, and allowed T_h to vary as a function of radius. We call this model the "two temperature free model".

In Figure 5.16, we show the fitting results of these two models. The two temperature free model provides a χ^2/dof of 5594.7/3730, which is much smaller than that of the two

temperature fixed model (χ^2/dof of 8672.8/3739). Note that the value of χ^2/dof for the single temperature model is in the middle of the two at 6396.5/3741. Although neither of these two-temperature models is a statistically acceptable, their unacceptability is likely caused by systematic errors resulting from calibration uncertainty. We proceed, using the two temperature free model in the following analysis.

In the two temperature model, the volume filling factor of each component is needed to derive the density profile (see (Fukazawa et al. 1994; Ikebe et al. 1999)). Assuming the cool component is confined within a volume V with an average volume filling factor η, the emission integral of the hot component $EI_{\rm h}$ and that of the cool component $EI_{\rm c}$ can be written as

$$EI_{\rm h} = n_{\rm h}^2(1-\eta)V \quad \text{and} \quad EI_{\rm c} = n_{\rm c}^2\eta V, \tag{5.18}$$

where $n_{\rm h}$ and $n_{\rm c}$ are the gas densities of the hot and cool components, respectively. Employing the assumption of pressure balance between the two components as

$$n_{\rm c}T_{\rm c} = n_{\rm h}T_{\rm h}, \tag{5.19}$$

Equation (5.18) yields

$$\eta = [1 + (\frac{T_{\rm h}}{T_{\rm c}})^2(\frac{EI_{\rm h}}{EI_{\rm c}})]^{-1}. \tag{5.20}$$

In Figure 5.17, we present the temperature, density, and pressure profiles obtained with the two temperature free model. We also show the volume filling factor as a function of radius. Except for the very inner region within 20 kpc, the volume filling factor of the cool component is lower than 0.1 %. We consider that there is no cool component in the outer region of $r > 20$ kpc. The temperatures of the hot and cool components within the radius of 20 kpc are 1.48 ± 0.02 keV and 0.76 ± 0.01 keV, respectively. The temperature in the outer region is ~ 4 keV, which is consistent with the value of $T_{\rm h}$ provided in Ikebe et al. (1999). Sanders & Fabian (2002) applied a similar two temperature model to one of the *Chandra* observations of the Centaurus cluster (the observation ID is 504). Although they applied this model for the projected spectra, the parameters they derived for the two components are similar to ours.

The total mass profile is obtained from the profiles shown in Figure 5.17 through Equation (5.5). We used the averaged gas density defined as $n_g = n_{\rm c}\eta + n_{\rm h}(1-\eta)$ in the calculation of the gas density. In Figure 5.18, we compare the mass profiles derived from the single temperature model and the two temperature free model. The mass of the innermost shell increases from $1.9 \pm \times 10^{11} M_\odot$ with the single temperature model to $3.1 \pm \times 10^{11} M_\odot$ with the two temperature model. However, the values of inner slope α_0 are consistent within the error (2.26 ± 0.46 for the single temperature model, and that of 1.79 ± 0.48 for the two temperature model), where α_0 is defined at $r_0 = 45$ kpc for the

Centaurus cluster. Therefore, we concluded that adopting either of the single temperature model or the two temperature model did not, at least for this cluster, significantly affect the resultant α_0.

The origin of a central cool component such as that observed in the Centaurus cluster remains an open question. However, the location and size of the central plume-like structure shown in the X-ray image of the Centaurus cluster (see Appendix G) implies that the structure might correspond to the cool component. Hydra A cluster and A1795, for which the two temperature model was required in the spectral analysis of the *ASCA* and *ROSAT* data, also showed the presence of a central structure as described in §5.6.3. If these central structures have a close connection with the cool component, we should not find a cool component in clusters in which such a central structure is not observed. PKS0745-191, in which remarkable central structures are not found, is such a cluster and has a long exposure time (see Table 4.1). We applied the two temperature free model to this cluster. Figure 5.19 shows the spectra and the temperature, density, and pressure profiles obtained with the two temperature free model. The value of χ^2/dof was 3800.1/3007, whereas that for the single temperature model was 3766.6/3014. The cool component is required only in the innermost region of $r < 40$ kpc with the volume filling factor of 0.2 %. We therefore concluded that the additional cool component is not required for PKS0745-191, supporting the connection between the central structure and the cool component. Further study is needed to clarify this point. In fact, Ikebe et al. (1995) concluded that the cool component in the Centaurus cluster is the hot inter-stellar medium associated with the cD galaxies. Application of the two temperature model to clusters other than the Centaurus cluster to derive the mass profile is a future task.

5.6.5 Comparison to the literature

Several previous authors have investigated the inner slope of the mass profiles using various methods. In this section we compare the inner slope we measured with those reported in recent works.

- A1060

  Tamura (1998, 2000) measured the mass profile in the central region of A1060 using the data from *ASCA* and *ROSAT*. They found that the total mass distribution was better described by the NFW model than by the King-type model. They also fitted the mass profile with the general form of the density profile given by Equation (5.11) (they call this the NFW′ model) and constrained the inner slope as $1.42 < \alpha < 1.65$, where they fixed r_s to 1 Mpc. Using Equation (5.13), it corresponds

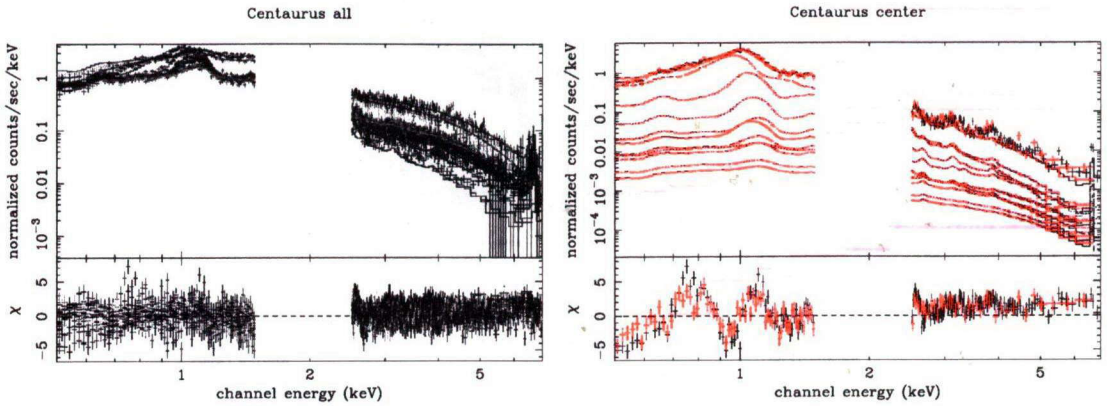

Figure 5.15: (**left**) Spectra of the all annuli of the Centaurus cluster, fitted with a single temperature model. We excluded 1.5–2.5 keV because the calibration uncertainty is significant. (**right**) Spectra of the innermost annuli for two data sets (Obs. IDs are 504 and 505). Large residuals remain below 1.5 keV.

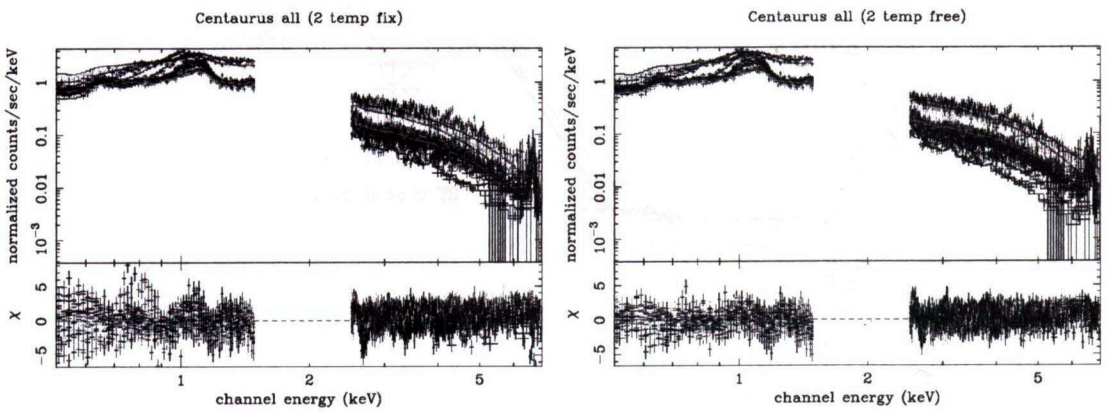

Figure 5.16: (**left**) Spectra fitted with the two temperature fixed model (see text). (**right**) Spectra fitted with the two temperature free model.

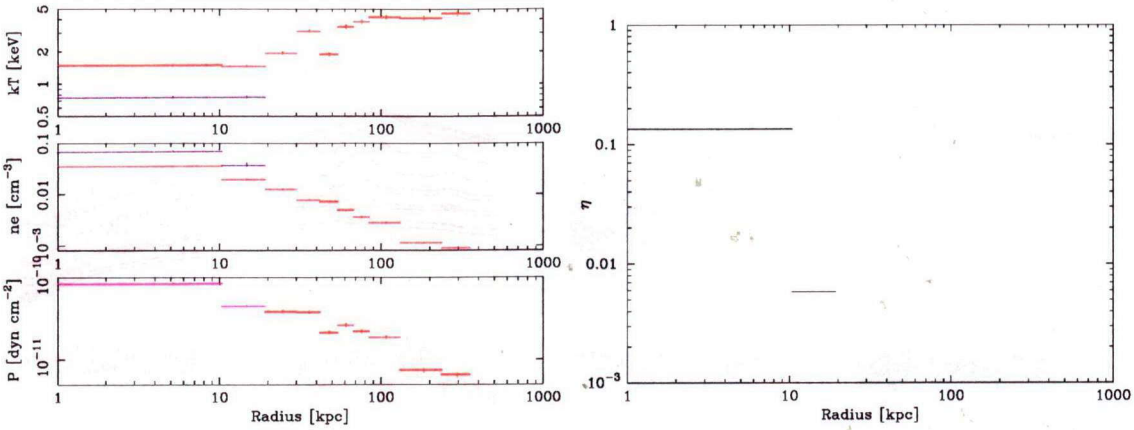

Figure 5.17: (**left**) Temperature, density, and pressure profiles of the Centaurus cluster obtained with the two temperature free model. The red and blue marks represent the hot and cool components, respectively.(**right**) Volume filling factor of the cool component as a function of radius.

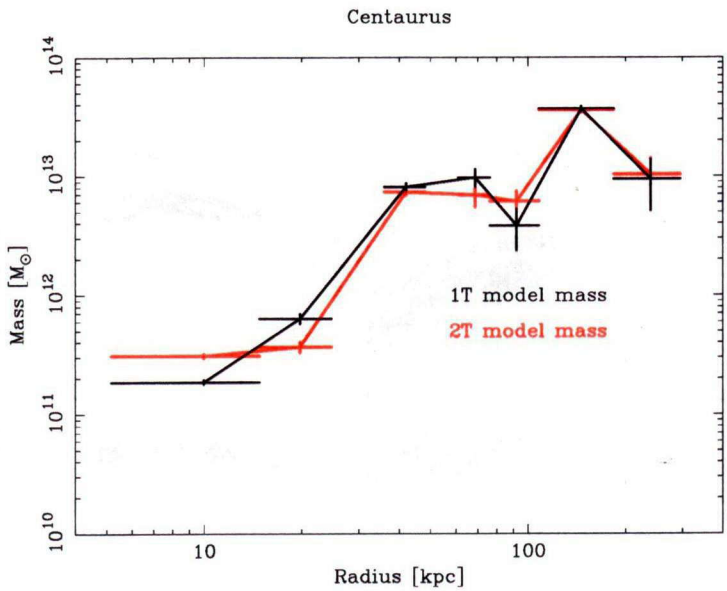

Figure 5.18: Comparison of mass profiles of the Centaurus cluster derived from the single temperature model (black) and the two temperature model (red).

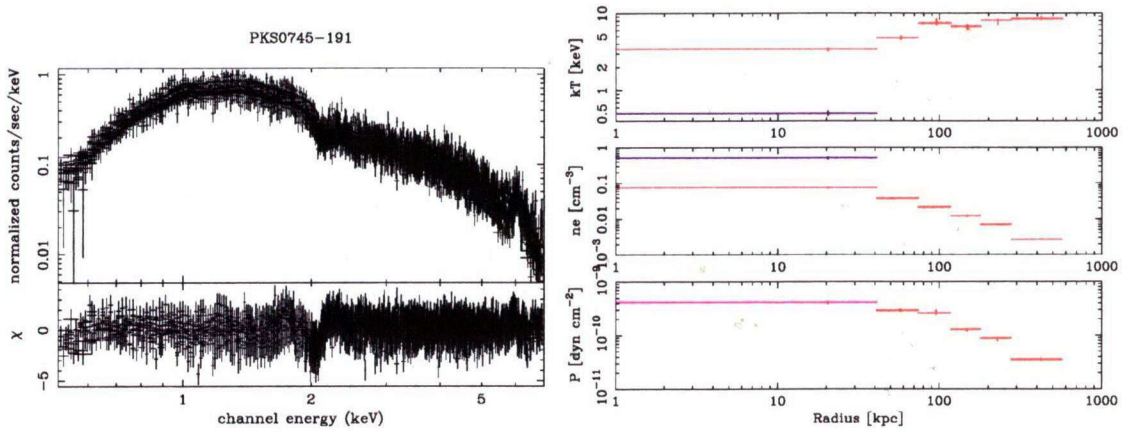

Figure 5.19: (**left**) Spectra of PKS0745-191 fitted with the two temperature free model. (**right**) Temperature, density, and pressure profiles of PKS0745-191 obtained with the two temperature free model. The red and blue marks represent the hot and cool components, respectively.

to $1.46 < \alpha_0 < 1.69$, which is consistent with our result of $\alpha_0 = 1.20 \pm 0.32$.

- A1795

  Ettori, Fabian, Allen, & Johnstone (2002) analyzed the *Chandra* data of A1795 and obtained a mass profile using a deprojection technique different from ours. They fitted the mass profile between 10 and 100 kpc with the power-law model given by Equation (5.9), providing $\alpha = 0.59$ (in the range 0.27–0.81 at a 90 % confidence level). This value is significantly smaller (flatter) than ours of $\alpha_0 = 1.32 \pm 0.41$, which is defined at $r_0 \sim 50$ kpc. However, if we look at their mass profile itself, it is consistent with ours at $r > 40$ kpc. There is, however, a difference in the innermost bin of the mass profiles by Ettori et al. (see Figure 10 in Ettori, Fabian, Allen, & Johnstone 2002), for which we did not get a data point.

- A2029

  Lewis, Buote, & Stocke (2002) obtained the deprojected mass profile of A2029 using the *Chandra* data. They applied the simple power-law fit in the region of $r < 260 h_{60}^{-1} kpc$ and obtained a slope of the density profile of 1.19 ± 0.04. This nicely agrees with our result of $\alpha_0 = 1.20 \pm 0.36$ defined at $r_0 = 60$ kpc.

- A2199

  Kelson et al. (2002) evaluated the density profile of A2199 from the velocity dispersion profile of NGC6166, the cD galaxy in A2199. According to their analysis, under the assumption of isotropy, the observed velocity dispersion profile can be reproduced only when the density profile has a soft core (i.e., $\alpha < 1$). Their result

is consistent with our measurement of the inner slope, $\alpha_0 = 0.64 \pm 0.50$, at $r_0 = 48$ kpc. Findings by two independent methods support the presence of the soft core.

- Hydra A
  David et al. (2001) obtained the deprojected mass profile of Hydra A with the *Chandra* data. They presented that the mass profile within the central 30–200 kpc region scales as $\rho \propto r^{-1.3}$. This result is lower than ours of $\alpha_0 = 1.86 \pm 0.50$ at r_0= 41 kpc, though they did not show the error of α.

5.6.6 Summary of this section

In this section, we discuss the validity of our measurements of the inner slope from various aspects. The center position does not significantly affect our results. We could not find any evidence of the dependence of the results on the deviation from the spherical symmetry. The two temperature model was applied to the Centaurus cluster, and we found that the resultant inner slope is not significantly altered from that by the single temperature model. Further applications of this model lie beyond the scope of this paper, and our results should therefore be regarded as the single temperature case. On the other hand, there was a hint that presence or absence of central structures may affect the distribution of the inner slope. Further study is needed to clarify this point. Consistencies with previous reports listed in §5.6.5 also imply potential problems in our analysis is small.

5.7 Relations between inner slope and other observational parameters

As shown in §5.5, the inner slope α_0 of the density profiles spans a wider range than that estimated from their errors. Even if we neglect the three clusters in which central structures might affect the results, α_0 ranges from 0 to 1.2 and spreads toward a flatter side than expected based on CDM simulations. If this spread of the distribution is intrinsic, what is it that determines the inner slope of the density profile? In this section, we explore observational parameters that primarily determine the inner slope α_0, by examining their correlations.

5.7.1 Redshift vs. α_0

We first show the relation between the redshift and the central slope α_0 in Figure 5.20. The correlation coefficient is -0.25 for this relation. This result suggests that the mass

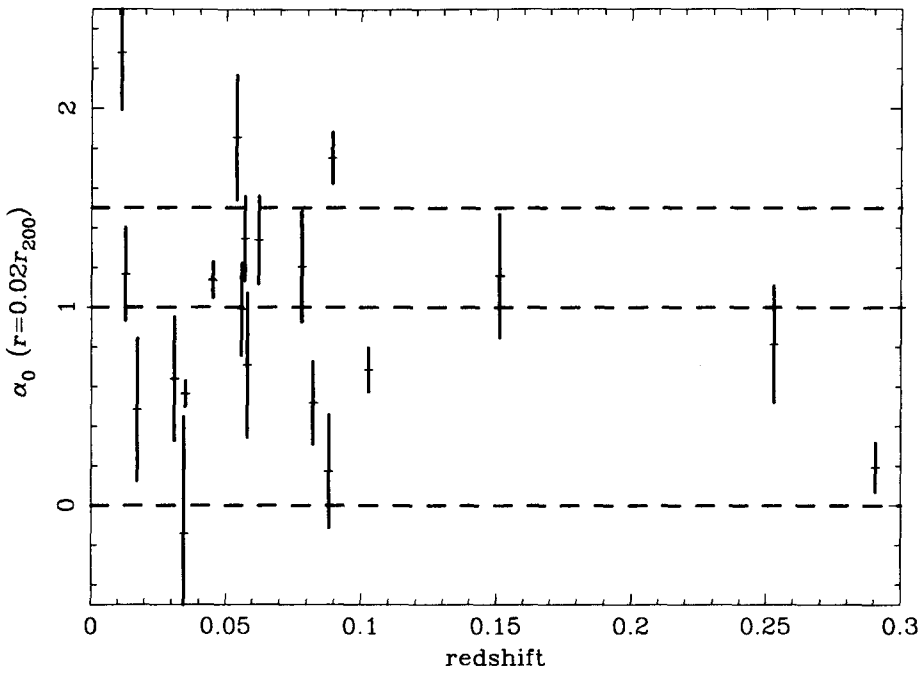

Figure 5.20: Redshft vs. central slope α_0.

profiles do not flatten in the course of cluster evolution.

5.7.2 Temperature vs. α_0

We plot the averaged temperature $kT_{\rm average}$ shown in Table 5.1 against the central slope α_0 in Figure 5.21. The correlation coefficient is 0.01. Simple arguments based on virial theorem suggest that the mass of a cluster is simply related to the cluster temperature as $M \propto T^{3/2}$. This relation implies that the central slope α_0 is not related to the scale of the cluster.

We also examined the relation between variation in the temperature profile $T(r)$ and the central slope α_0. To examine this relation, we defined the variation in temperature as

$$\frac{\Delta T}{T_{\rm avarage}} \equiv \frac{T_{\rm max} - T_{min}}{T_{\rm avarage}}, \tag{5.21}$$

where $T_{\rm max}$ and $T_{\rm min}$ are the maximum and minimum temperatures of the temperature profiles shown in Appendix B, respectively. We show the relation between the variation in temperature profile and the central slope α_0 in Figure 5.22. No correlation was observed in this relation (the correlation coefficient is 0.03.). Most of our sample clusters were of the cooling flow type. Thus, this result suggests that a cooling flow is not associated with the central slope α_0.

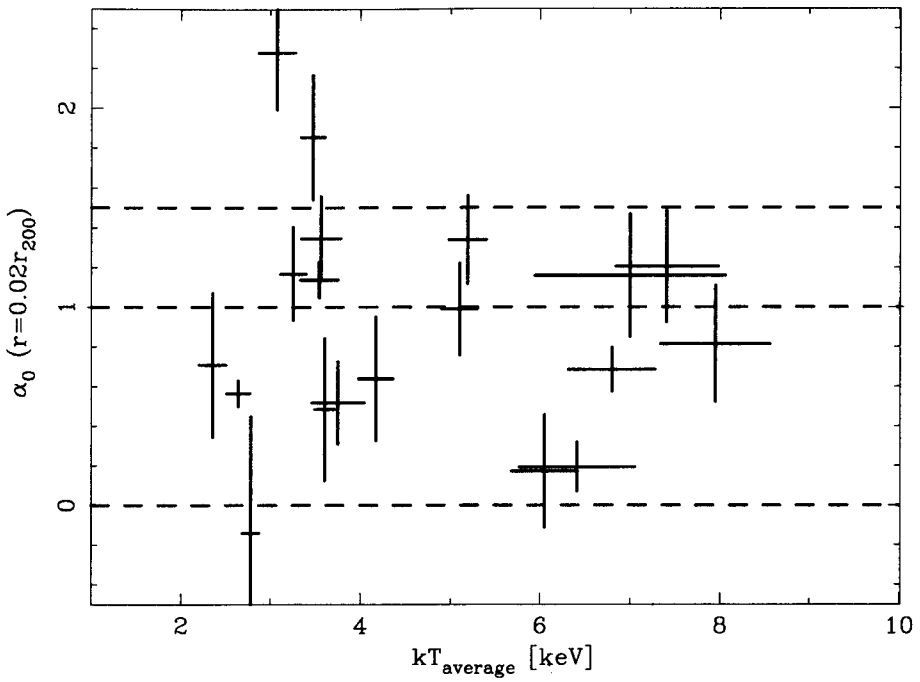

Figure 5.21: Temperature vs. central slope α_0.

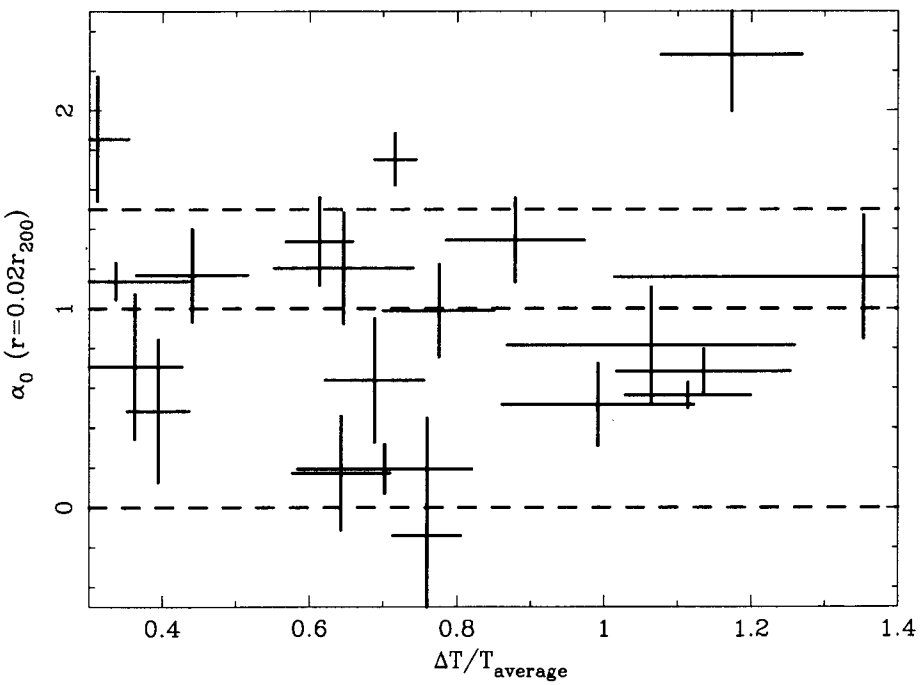

Figure 5.22: Variation in the temperature profile vs. α_0.

5.7.3 Gas fraction vs. α_0

We next investigated the relation between the gas fraction and the inner slope α_0. The gas fraction is the ratio of the hot gas mass to the total mass, and is defined as a function of radius. The integrated gas mass profile $M_{\rm gas}(< r)$ is given by

$$\begin{aligned} M_{\rm gas}(< r) &= \int_0^r 4\pi r'^2 \rho_{\rm gas}(r) dr' \\ &= 4\pi\mu m_p \int_0^r 4\pi r'^2 n_{\rm gas}(r) dr', \end{aligned} \tag{5.22}$$

where $n_{\rm gas}(r)$ is the total number density of electrons and ions, $\mu(= 0.6)$ is the mean molecular weight, and m_p is the proton mass. This gas mass profile is obtained with the observed gas density profile shown in Appendix B. The gas fraction is defined as

$$f_{\rm gas}(r) \equiv \frac{M_{\rm gas}(< r)}{M(< r)}. \tag{5.23}$$

In Appendix H, we present the profiles of total mass, gas mass, and gas fraction for 23 sample clusters. It was found that the gas fraction increases toward the center for some clusters. This is consistent with the result shown in §5.4 that the gas is more concentrated than the total mass or dark matter.

In Figure 5.23, the gas fractions at the radius of $r = 0.05 r_{200}$ are plotted against the inner slope α_0. A negative correlation was observed with the correlation coefficient of -0.51, for which case, at a significance level of about 3%, the hypothesis of no correlation is rejected. This correlation might be a kind of artifact in the analysis, since we derive both the total mass profile and the gas mass profile from the same gas density profile and gas temperature profile. However, it is unlikely that the observed correlation is due to correlated errors between the two parameters, considering the size of the errors.

In order to confirm this correlation is artifact or not, we took M_{200}, which is determined solely from the gas temperature and redshift, instead of the integrated mass profile. We redefined the gas fraction as

$$f'_{\rm gas}(r) \equiv \frac{M_{\rm gas}(< r)}{M_{200}}. \tag{5.24}$$

We plot $f'_{\rm gas}$ at the radius of $r = 0.05 r_{200}$ against the inner slope α_0 in Figure 5.24. Although the correlation coefficient of -0.40 is smaller than that for $f_{\rm gas}$, the no correlation hypothesis is rejected at a significance level of less than 10%.

Correlations between the inner slope α_0 and the gas fraction according indicate that gas-rich clusters in the central region tend to have a flat core: $\alpha < 1$. We discuss this relation in §6.3.3.

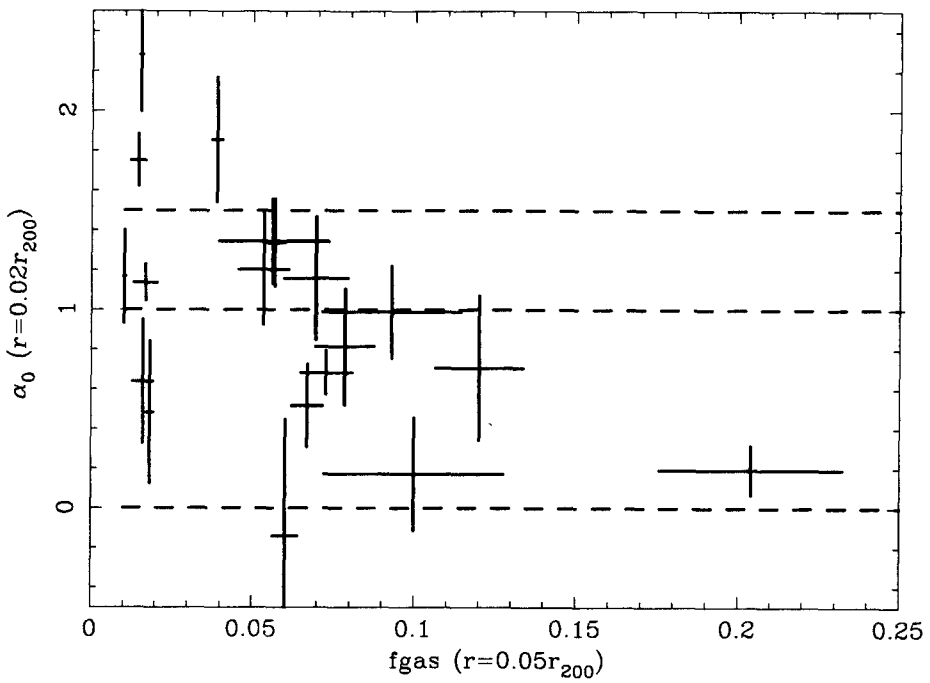

Figure 5.23: Gas fraction at the radius of $r = 0.05r_{200}$ vs. central slope α_0.

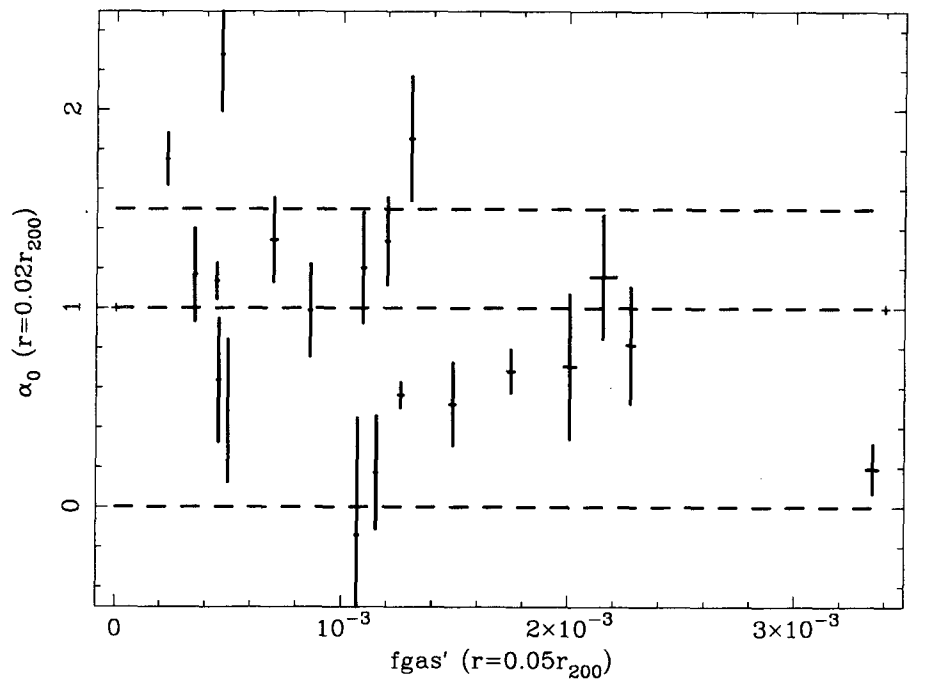

Figure 5.24: Gas fraction redefined in Equation (5.24) ($f'_{\rm gas}$) vs. central slope α_0.

Chapter 6

Discussion and Conclusions

We have analyzed the *Chandra* data of 23 clusters of galaxies in order to investigate central mass distribution. The high spatial resolution imaging spectroscopy of *Chandra* and a new deprojection technique enable us to measure the temperatures and gas densities in the very central region of sample clusters without assuming any particular models. Under the assumptions of hydrostatic equilibrium and spherical symmetry, we obtained the deprojected mass profiles. Our major results are as follows.

1. The mass profiles scaled with r_{200} and M_{200} agree each other on the large scale $r > 0.1r_{200}$. In contrast, the central ($r < 0.1r_{200}$) mass profiles show a large scatter.

2. We fitted the mass profiles with the King profile and the NFW profile. Some clusters showed a flatter slope than that with the NFW profile. It was found that the core (or scale) radii of mass profiles are systematically larger than those of gas profiles, suggesting that gas is more concentrated than dark matter.

3. The inner slope α_0 of the density profile was derived by fitting the mass profile with a general form of dark matter density profile for 20 clusters. The values of α_0 span a wide range (from 0 to 2.3). For 6 out of 20 clusters, α_0 are lower than unity at a 90 % confidence level.

4. We investigated several features that might influence the results of the inner slope, including center position, ellipticity, central structure of a cluster, and the central cool component within the framework of the two temperature model. We found that the systematic effects of these features are not significant except in the case of the central structure, which may broaden the distribution of the inner slope α_0. However, even if we excluded the clusters in which central structures were seen, the inner slope α_0 distributes widely in the range from 0 to 1.2.

5. We examined the relationships between the inner slope α_0 and other observational parameters. Although redshift, averaged temperature, and variation in the temperature profile are not correlated with the inner slope α_0, gas fraction near the center of a cluster has a negative correlation with α_0.

Among these results, the fact that α_0 distributes below 1 (i.e., in some clusters in which the density profile is flatter than r^{-1}), is most important. The correlation between gas fraction and α_0 is second-most important. We discuss these points in the following sections.

6.1 Central baryonic component

As described in §5.3, the inner slope α_0 we derived is for the density profile of total mass, and the slope provided by simulations is usually that for dark matter. Masses other than dark matter, namely baryonic components, surely present at the center of clusters. As shown in §5.6.1, BCGs, which are typically massive elliptical galaxies, are located at the central region of all sample clusters. Further, we showed that the gas fraction increases toward the center for some clusters. Considering the contribution of these baryonic components, the inner slope for the density profile of dark matter might be smaller (flatter) than that of α_0, which we derived for the total mass profile. This point should be borne in mind in the following section, where a comparison with simulations is made.

6.2 Core problem of dark matter density profile

The values of α_0 span a wide range of 0 to 2.3 for 20 clusters. Among these, 6 clusters have α_0 values lower than unity at a 90 % confidence level. As shown in Chapter 1 and Chapter 2, CDM simulations predict that the inner slope α is in the range $1 < \alpha < 2$. Therefore, our results are inconsistent with the CDM simulations. Our observations provide flatter slopes, at least for some clusters, than those expected from the CDM simulations. This is true even if we neglect the clusters showing central structures ($0 < \alpha_0 < 1.2$).

A similar claim has been presented by authors who are investigating the rotation curve of galaxies and clusters. Firmani et al. (2001) examined the observed rotation curves of dwarf and low surface brightness (LSB) galaxies, and two clusters of galaxies, and found that all of those objects have soft cores: $\alpha < 1$. Swaters et al. (2002) observed the rotation curve of 15 dwarf and LSB galaxies and found inner slopes in the range of

$0 \lesssim \alpha \lesssim 1$ in the majority. This inconsistency between observations and simulations in terms of the dark matter distribution at the center of galaxies or clusters is called the core problem. Our results indicate that the core problem exists in a significant fraction of clusters observed through X-ray observations. Several models to resolve the core problem have been proposed. In §6.3, we discuss alternative theories to resolve the core problem.

6.3 Alternative theories to resolve the core problem

6.3.1 Modified Newtonian Dynamics (MOND)

Milgrom (1983) proposed Modified Newtonian Dynamics (MOND) , which accounts for the so-called dark matter problem not by introducing dark matter but by modifying Newtonian dynamics. The basic assumption of MOND is that Newtonian dynamics breaks down below an acceleration threshold of $a_0 \sim 10^{-8}$ cm s^{-2}. MOND has successfully accounted for the rotation curves of galaxies with various luminosities (Sanders & Verheijen 1998).

The MOND acceleration of a particle at distance r from a mass M satisfies

$$a = \sqrt{a_0 \frac{MG}{r^2}} \tag{6.1}$$

when $\frac{MG}{r^2} \ll a_0$, where $a_0 \sim 1.2 \times 10^{-8}$ cm s^{-2} is a constant of the dimensions of an acceleration. In MOND, the hydrostatic equilibrium equation can be written as

$$\frac{d\ln T(r)}{d\ln r} + \frac{d\ln \rho(r)}{d\ln r} = -\frac{\mu m_p}{kT}\sqrt{a_0 \frac{M(<r)G}{r^2}} \tag{6.2}$$

for $\frac{M(<r)G}{r^2} \ll a_0$. If the density profile $\rho(r)$ and the total mass profile $M(<r)$ are given, the latter is calculated from the former since no dark matter is assumed, and the temperature profile $T(r)$ is predicted.

Aguirre, Schaye, & Quataert (2001) compared the temperature profiles predicted in this way with observations (*ASCA*, *BeppoSAX*, and *XMM-Newton*) for the Virgo cluster, Coma cluster, and A2199. They concluded that predictions with MOND were inconsistent with the observations. In Figure 6.1, we compare the temperature profile predicted with MOND by Aguirre et al. with the observed profile we obtained with *Chandra* for A2199. The observed temperature, which is consistent with *ASCA* measurements by Markevitch, Vikhlinin, Forman, & Sarazin (1999), is 2–3 times higher than that predicted with MOND. This finding suggests that dark matter is required to describe the mass profiles of clusters, and that MOND cannot solve the core problem.

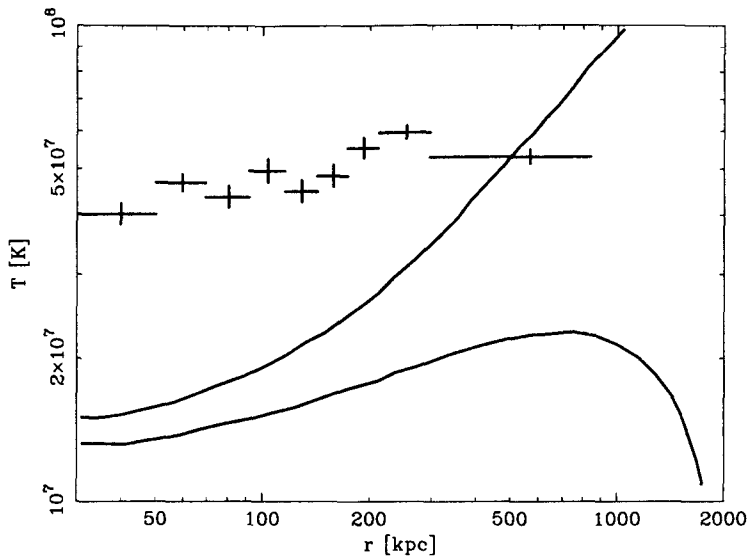

Figure 6.1: The temperature profile of A2199 predicted with MOND by Aguirre, Schaye, & Quataert (2001) (solid lines) compared with that measured with *Chandra*.

6.3.2 Self-Interacting Dark Matter (SIDM)

Many authors have proposed new kinds of dark matter alternative to CDM (e.g.,decaying dark matter (Cen 2001), fluid dark matter (Peebles 2000), and so on) to account for the core problem. Self-Interacting Dark Matter (SIDM) proposed by Spergel & Steinhardt (2000) is one of a possible candidate. SIDM assumes that dark matter particles have weak interactions (other than the gravitational one) with each other and with other kinds of particles. Since the CDM model successfully reproduces the large scale structure of the universe ($r \gg 1$ Mpc), the possible collision of SIDM dark matter should be effective only at scales below 1 Mpc. The required collision cross section σ_{XX} for a SIDM particle of mass m_X is obtained by assuming $(m_X n_X)(\sigma_{XX}/m_X)l \sim 1$ where n_X is the number density of dark matter particle and $l \sim 1$ Mpc is the cluster size. This is written as

$$(\frac{\sigma_{XX}}{m_X}) \approx 1.6h^{-1} \text{ cm}^2 \text{ g}^{-1} \, (\frac{10^4 \rho_{\text{crit}}}{\rho_c})(\frac{1h^{-1}\text{Mpc}}{l}), \tag{6.3}$$

where ρ_c is the central density of the cluster. The corresponding mean collision time-scale is

$$\Delta t \approx \frac{l}{v} \approx 10^9(\frac{1000\text{km/s}}{v})(\frac{l}{1h^{-1}\text{Mpc}})h^{-1} \text{ year}. \tag{6.4}$$

Therefore, a cross section of the order ~ 1 cm^2 g^{-1} will affect the central portion of the dark matter profile. Yoshida et al. (2000) and Davé, Spergel, Steinhardt, & Wandelt (2001) conducted such simulations and found that SIDM dark matter models with $\frac{\sigma_{XX}}{m_X} \sim 1$ cm^2 g^{-1} lead to the formation of a flat central profile rather than a cusp. Their models

simultaneously produce a spherical dark matter halo by the self-interaction of dark matter.

According to Yoshida et al. (2000), the core radii of the simulated dark matter profile are in the range of 40 kpc to 160 kpc for the collision cross section 0.1–10 cm^2 g^{-1}. The core radii we derived with the King profile are comparable to this range if we neglect some clusters with central structures. However, not all of our results are in agreement with the SIDM model. Yoshida et al. (2000) mentioned that the SIDM core size agreed with observations only if $\sigma_{XX} \propto v^{-1}$. This means that self-interactions diminish in hot clusters. The lack of a correlation between the inner slope α_0 and the temperature (Figure 5.21) we observed is not qualitatively consistent with this prediction. Further quantitative tests are needed to adopt or reject the SIDM scenario as a solution of the core problem. The origin of SIDM also remains a question.

6.3.3 Effect of the dynamical friction between dark matter and gas

In the central region of clusters, the baryonic components such as hot gas and stars in a galaxy are not negligible, as discussed in §6.1. These baryonic components are usually considered to follow the gravitational potential, which is predominantly determined by dark matter distribution. However, there is a way in which the baryonic components affect the dark matter distribution. El-Zant, Shlosman, & Hoffman (2001) argued that the core problem can be resolved within the framework of the standard CDM model by considering the dynamical friction (DF) between dark matter and gas. El-zant et al. assumed that the gas is not initially smoothly distributed but is, rather, concentrated in clumps. Such gas clumps move through smooth dark matter particles, lose energy to the central dark halo, and heat it up. This leads to the puffing up of the central regions and to the flattening of the density profile. Monte Carlo simulation by El-zant et al. successfully reproduced the observed flat density profile.

This DF model well accounts for our observational results (i.e., the negative correlation between the inner slope α_0 and the gas fraction, and the higher concentration of the gas than of dark matter toward the center). In the DF model, the baryonic (gas) component is more centrally concentrated than dark matter, because gas gives its energy to dark matter and shrinks toward the center.

The key to this model is the fragmentation of gas, which causes the gas to clump into superparticles among smoothly distributed dark matter particles. El-zant et al. assumed the mass of gas clumps to be 10^8–10^9 $M_\odot$ for large galaxies. The size of such clumps is about 5–10 kpc in the central region of clusters, assuming the central gas density

$\rho_{c,gas} = 10^{-25}$ g cm^{-3} and $M \sim \rho_{c,gas} r^3$. As described in §5.6.3 (see also Appendix G), 10/23 our sample clusters showed a remarkable structure in the central region. Those structures might be the remnants of the clumps of gas.

In addition to these central structures, X-ray structures associated with the radio lobes have been found in several clusters and are considered to be hot bubbles in the ICM (see, e.g., Fabian et al. 2000; McNamara et al. 2000; Fujita et al. 2002). Such hot bubbles are buoyant, and are considered to be moving outward in the cluster gravitational potential. For example, the speed of a bubble in A133 is estimated to be $v \sim 700$ km/s (Fujita et al. 2002). The rate of energy loss via DF is given by $\dot{E} = M(dv/dt)v$. Although these bubbles are slightly different from the gas clumps assumed in the simulation by El-zant et al., at such a high speed and a massive bubble might effectively give its energy to dark matter. If we adopt this model, the scatter in the inner slope α_0 may be explained by the different status of the gas in the central region. If the turbulence of the gas is predominantly caused by the central radio source, and it results in a flat dark matter profile, the inner slope α_0 can be considered to depend on the activity of the central radio source, including the past activity.

As described above, there are several favorable aspects of the DF model, the most important of which is that this model solves the core problem within the framework of the standard CDM model.

6.4 Distribution of dark matter and gas in hydrostatic equilibrium

In §5.7, we found a correlation between the inner slope and the gas fraction. The DF model described above provides one of the possible origins of this correlation. We attempted to account for this correlation from a different point of view, focusing on the hydrostatic equilibrium.

Let us simplify that both the dark matter density profile and the gas density profile are the power laws, $\rho_d = \rho_{d0} r^{-\alpha_d}$ and $\rho_g = \rho_{g0} r^{-\alpha_g}$, respectively. Substituting these into the equation of hydrostatic equilibrium (Equation (2.9)) and making a further assumption that gas is an isothermal yield, we obtain

$$\frac{kT\alpha_g}{\mu m_p} r^{-1} = 4\pi G\left[\frac{\rho_{d0} r^{-\alpha_d+1}}{3-\alpha_d} + \frac{\rho_{g0} r^{-\alpha_g+1}}{3-\alpha_g}\right]. \tag{6.5}$$

It is apparent that this equation exactly holds only when each of the slopes α_g and α_d equals 2. If the slope α_d is smaller than 2, the α_g should be larger than 2, and the gas

fraction at the inner scale should be high. Although the slope we obtained is α_0 for the total mass and not α_d for dark matter, α_0 should be closer to α_d than to α_g when the dark matter is predominant among several forms of mass.

The explanation above is too much simplified, but it is the bottom line of the correlation we found. Under the assumption of hydrostatic equilibrium, the high gas mass fraction and the flat slope of the density profile are consistent. On the other hand, if we can obtain the gas density profile and the dark matter profile independently (e.g.. the former from X-ray observations and the latter from lensing studies), they may enable us to check the validity of hydrostatic equilibrium.

6.5 Conclusion

The mass profiles derived from the deprojected temperature and gas density profiles show a large scatter on the small scale ($r < 0.1r_{200}$). We examined the inner slope of the density profiles. The inner slope α_0 of the dark matter density profile span a wide range (i.e., $0 \leq \alpha \leq 2.3$). Some clusters have a profile flatter than the NFW profile, and the cuspy dark matter density profiles with $\alpha > 1$ predicted by CDM simulations are ruled out for 6/20 clusters. In this work, we first showed that the core problem of the dark matter profile is common not only for dwarf galaxies but also for clusters.

We evaluated three alternative theories to resolve the core problem of dark matter: Modified Newtonian Dynamics (MOND), the Self-Interacting Dark Matter (SIDM) model, and the Dynamical Friction (DF) model. The MOND cannot reproduce the observed temperature profile, suggesting that the dark matter is required to describe the cluster mass distribution. The SIDM model appear to account for the observed core radii of the dark matter profile. However, a contradiction existed between the SIDM and our observational results. The DF model accounts not only for the flat slope but also for our observational results that the inner slope correlates with the central gas fraction and that gas is more concentrated than dark matter in the central region. The DF model is considered to be the most favorable of the three theories we evaluated.

Bibliography

Abell, G. O. 1958, ApJS, 3, 211

Abell, G. O., Corwin, H. G., & Olowin, R. P. 1989, ApJS, 70, 1

Aguirre, A., Schaye, J., & Quataert, E. 2001, ApJ, 561, 550

Allen, S. W., Fabian, A. C., Edge, A. C., Bautz, M. W., Furuzawa, A., & Tawara, Y. 1996, MNRAS, 283, 263

Allen, S. W. 2000, MNRAS, 315, 269

Arabadjis, J. S., Bautz, M. W., & Garmire, G. P. 2002, ApJ, 572, 66

Bertschinger, E. & Meiksin, A. 1986, ApJ, 306, L1

Blanton, E. L., Sarazin, C. L., McNamara, B. R., & Wise, M. W. 2001, ApJ, 558, L15

Brinkman, B. C. et al. 2000, Proc. SPIE, 4012, 81

Bullock, J. S., Kolatt, T. S., Sigad, Y., Somerville, R. S., Kravtsov, A. V., Klypin, A. A., Primack, J. R., & Dekel, A. 2001, MNRAS, 321, 559

Buote, D. A., Lewis, A. D., Brighenti, F., & Mathews, W. G. 2002, astro-ph/0205362

Burkert, A. 1995, ApJ, 447, L25

Byram, E. T., Chubb, T. A., & Friedman, H. 1966, Science, 152, 66

Canali, C., Martini, M., Ottaviani, G., and Quaranta, A. 1972, *IEEE Transactions of Nuclear Science*, NS-19, 4

Canizares, C. et al. 2001, in preparation

Carter, D. & Metcalfe, N. 1980, MNRAS, 191, 325

Cen, R. 2001, ApJ, 546, L77

David, L. P., Nulsen, P. E. J., McNamara, B. R., Forman, W., Jones, C., Ponman, T., Robertson, B., & Wise, M. 2001, ApJ, 557, 546

Davé, R., Spergel, D. N., Steinhardt, P. J., & Wandelt, B. D. 2001, ApJ, 547, 574

de Vaucouleurs, G., de Vaucouleurs, A., Corwin, H. G., Buta, R. J., Paturel, G., & Fouque, P. 1991, Volume 1-3, XII, 2069 pp. 7 figs.. Springer-Verlag Berlin Heidelberg New York,

El-Zant, A., Shlosman, I., & Hoffman, Y. 2001, ApJ, 560, 636

Ettori, S., Fabian, A. C., Allen, S. W., & Johnstone, R. M. 2002, MNRAS, 331, 635

Evrard, A. E., Metzler, C. A., & Navarro, J. F. 1996, ApJ, 469, 494

Fabian, A. C., Willingale, R., Pye, J. P., Murray, S. S., & Fabbiano, G. 1980, MNRAS, 193, 175

Fabian, A. C., Hu, E. M., Cowie, L. L., & Grindlay, J. 1981, ApJ, 248, 47

Fabian, A. C., Peres, C. B., & White, D. A. 1997, MNRAS, 285, L35

Fabian, A. C. et al. 2000, MNRAS, 318, L65

Fabian, A. C., Mushotzky, R. F., Nulsen, P. E. J., & Peterson, J. R. 2001, MNRAS, 321, L20

Fabian, A. C., Sanders, J. S., Ettori, S., Taylor, G. B., Allen, S. W., Crawford, C. S., Iwasawa, K., & Johnstone, R. M. 2001, MNRAS, 321, L33

Firmani, C., D'Onghia, E., Chincarini, G., Hernández, X., & Avila-Reese, V. 2001, MNRAS, 321, 713

Fritz, G., Davidsen, A., Meekins, J. F., & Friedman, H. 1971, ApJ, 164, L81

Fukazawa, Y., Ohashi, T., Fabian, A. C., Canizares, C. R., Ikebe, Y., Makishima, K., Mushotzky, R. F., & Yamashita, K. 1994, PASJ, 46, L55

Fukazawa, Y. 1997, Ph.D. thesis, Univ. Tokyo

Fukushige, T. & Makino, J. 1997, ApJ, 477, L9

Fujita, Y., Koyama, K., Tsuru, T., & Matsumoto, H. 1996, PASJ, 48, 191

Fujita, Y., Sarazin, C. L., Kempner, J. C., Rudnick, L., Slee, O. B., Roy, A. L., Andernach, H., & Ehle, M. 2002, ApJ, 575, 764

Fukushige, T. & Makino, J. 2001, ApJ, 557, 533

Garmire, G. P. et al. 2001, in preparation

Ghigna, S., Moore, B., Governato, F., Lake, G., Quinn, T., & Stadel, J. 2000, ApJ, 544, 616

Hashimotodani, K. 1999, PhD thesis, Osaka University

Heinz, S., Reynolds, C. S., & Begelman, M. C. 1998, ApJ, 501, 126

Henriksen, M. J. & Markevitch, M. L. 1996, ApJ, 466, L79

Hernquist, L. 1990, ApJ, 356, 359

Ikebe, Y. 1995, PhD thesis, University of Tokyo (RIKEN IPCR CR-87)

Ikebe, Y. et al. 1997, ApJ, 481, 660

Ikebe, Y., Makishima, K., Fukazawa, Y., Tamura, T., Xu, H., Ohashi, T., & Matsushita, K. 1999, ApJ, 525, 58

Jerius, D., Donnelly, R. H., Tibbetts, M. S., Edgar, R. J., Gaetz, T. J., Schwartz, D. A., Van Speybroeck, L. P., & Zhao, P. 2000, Proc. SPIE, 4012, 17

Johnstone, R. M., Allen, S. W., Fabian, A. C., & Sanders, J. S. 2002, MNRAS, 336, 299

Kaastra, J. S. & Mewe, R. 1993, A&AS, 97, 443

Katayama, H., Hayashida, K., Takahara, F., Fujita, Y. 2003, ApJ, 585, in printing

Kelson, D. D., Zabludoff, A. I., Williams, K. A., Trager, S. C., Mulchaey, J. S., & Bolte, M. 2002, ApJ, 576, 720

King, I. 1962, AJ, 67, 274

Lewis, A. D., Buote D. A., & Stocke, J. T. 2002, astro-ph/0209205

Liedahl, D. A., Osterheld, A. L., & Goldstein, W. H. 1995, ApJ, 438, L115

Makino, N., Sasaki, S., & Suto, Y. 1998, ApJ, 497, 555

Markevitch, M., Forman, W. R., Sarazin, C. L., & Vikhlinin, A. 1998, ApJ, 503, 77

Markevitch, M., Vikhlinin, A., Forman, W. R., & Sarazin, C. L. 1999, ApJ, 527, 545

Markevitch, M. 2001, http://cxc.harvard.edu/contrib/maxim/bg/index.html

Makishima, K. et al. 2001, PASJ, 53, 401

Mazzotta, P., Kaastra, J. S., Paerels, F. B., Ferrigno, C., Colafrancesco, S., Mewe, R., & Forman, W. R. 2002, ApJ, 567, L37

McNamara, B. R. et al. 2000, ApJ, 534, L135

McNamara, B. R. e t al. 2001, ApJ, 562, L149

Mewe, R., Gronenschild, E. H. B. M., & van den Oord, G. H. J. 1985, A&AS, 62, 197

Mewe, R., Lemen, J. R., & van den Oord, G. H. J. 1986, A&AS, 65, 511

Milgrom, M. 1983, ApJ, 270, 365

Mitchell, R. J., Culhane, J. L., Davison, P. J. N., & Ives, J. C. 1976, MNRAS, 175, 29P

Mohr, J. J., Mathiesen, B., & Evrard, A. E. 1999, ApJ, 517, 627

Moore, B., Governato, F., Quinn, T., Stadel, J., & Lake, G. 1998, ApJ, 499, L5

Moore, B., Quinn, T., Governato, F., Stadel, J., & Lake, G. 1999, MNRAS, 310, 1147

Morrison, R. & McCammon, D. 1983, ApJ, 270, 119

Murray, S. S., Chappell, J. H., Kenter, A. T., Kraft, R. P., Meehan, G. R., & Zombeck, M. V. 1998, Proc. SPIE, 3356, 974

Navarro, J. F., Frenk, C. S., & White, S. D. M. 1995, MNRAS, 275, 56

Navarro, J. F., Frenk, C. S., & White, S. D. M. 1996, ApJ, 462, 563

Navarro, J. F., Frenk, C. S., & White, S. D. M. 1997, ApJ, 490, 493

Norman, C. & Meiksin, A. 1996, ApJ, 468, 97

Ota, N. 2000, PhD thesis, University of Tokyo

Peterson, J. R. et al. 2001, A&A, 365, L104

Raymond, J. C. & Smith, B. W. 1977, ApJS, 35, 419

Peebles, P. J. E. 2000, ApJ, 534, L127

Reiprich, T. H. & Böhringer, H. 2002, ApJ, 567, 716

Rybicki, G. B. & Lightman, A. P. 1979, New York, Wiley-Interscience, 1979. 393 p.,

Sand, D. J., Treu, T., & Ellis, R. S. 2002, ApJ, 574, L129

Sanders, R. H. & Verheijen, M. A. W. 1998, ApJ, 503, 97

Sanders, J. S. & Fabian, A. C. 2002, MNRAS, 331, 273

Sarazin, C. L., 1988, " X-ray emissions from clusters of galaxies", Cambridge University Press

Sarazin, C. L., Baum, S. A., & O'Dea, C. P. 1995, ApJ, 451, 125

Schmidt, R. W., Allen, S. W., & Fabian, A. C. 2001, MNRAS, 327, 1057

Spergel, D. N. & Steinhardt, P. J. 2000, Physical Review Letters, Volume 84, Issue 17, April 24, 2000, pp.3760-3763, 84, 3760

Suto, Y., Sasaki, S., & Makino, N. 1998, ApJ, 509, 544

Swaters, R. A., Madore, B.F., van den Bosch, F.C., Balcells, M. 2002, astro-ph/0210152

Tamura, T. 1998, Ph.D. thesis, University of Tokyo

Tamura, T., Makishima, K., Fukazawa, Y., Ikebe, Y., & Xu, H. 2000, ApJ, 535, 602

Tamura, T. et al. 2001, A&A, 365, L87

Taylor, G. B., Fabian, A. C., & Allen, S. W. 2002, MNRAS, 334, 769

Tsunemi, H., Hiraga, J., Mori, K., Yoshita, K., & Miyata, E. 1999, Nuclear Instruments and Methods in Physics Research A, 436, 32

van Speybroeck, L. P., Jerius, D., Edgar, R. J., Gaetz, T. J., Zhao, P., & Reid, P. B. 1997, Proc. SPIE, 3113, 89

Voges, W. et al. 1999, A&A, 349, 389

Weisskopf, M. C. & O'dell, S. L. 1997, Proc. SPIE, 3113, 2

Weisskopf, M. C., Tananbaum, H. D., Van Speybroeck, L. P., and O'Dell, S. L. 2000, In *Proc. SPIE, X-Ray Optics, Instruments, and Missions III, Joachim E. Truemper; Bernd Aschenbach; Eds.*, 4012, 2

White, D. A., Jones, C., & Forman, W. 1997, MNRAS, 292, 419

White, D. A. & Buote, D. A. 2000, MNRAS, 312, 649

Xu, H., Makishima, K., Fukazawa, Y., Ikebe, Y., Kikuchi, K., Ohashi, T., & Tamura, T. 1998, ApJ, 500, 738

Yoshida, N., Springel, V., White, S. D. M., & Tormen, G. 2000, ApJ, 535, L103

Zhao, P., Cohen, L. M., & van Speybroeck, L. P. 1997, Proc. SPIE, 3113, 106

Zwicky, F. E., Herzog, P., Wild, M. K., & Kowal, C. T., 1961-1968, *Catalogues of Galaxies and Clusters of Galaxies,* Vol. 1-6., Pasadena, Caltech.

Appendix A

All cluster images

We show the 0.3–10 keV raw *Chandra* images of the 23 sample clusters. The images are binned with bin size of about 2″ (4 pixels). All observations are added into one image, but the exposure is not corrected. The overlaid contours are *ROSAT*/PSPC or *ROSAT*/HRI (for A963) image. The contour levels correspond to n times the 1-σ background for n = 4, 8, 12, 18, 36, 72, 144, and 200.

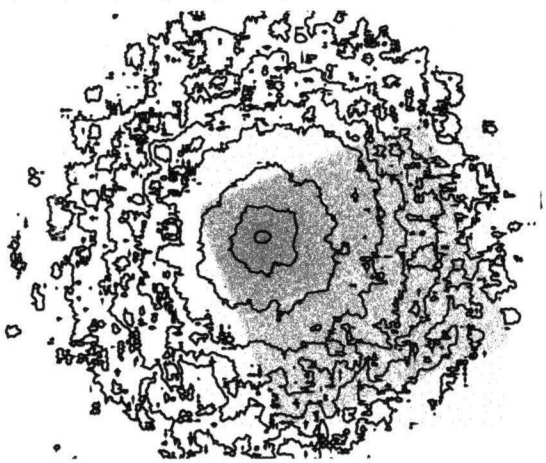

A1060 $z = 0.0126$

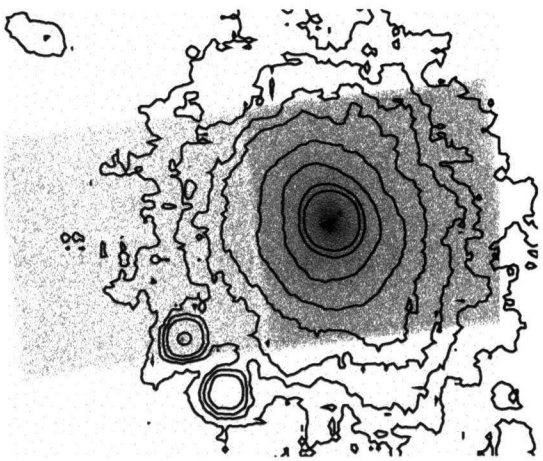

A133 $z = 0.0570$

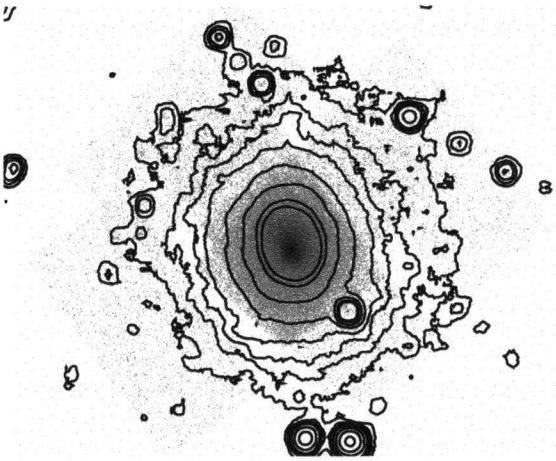

A1795 $z = 0.0622$

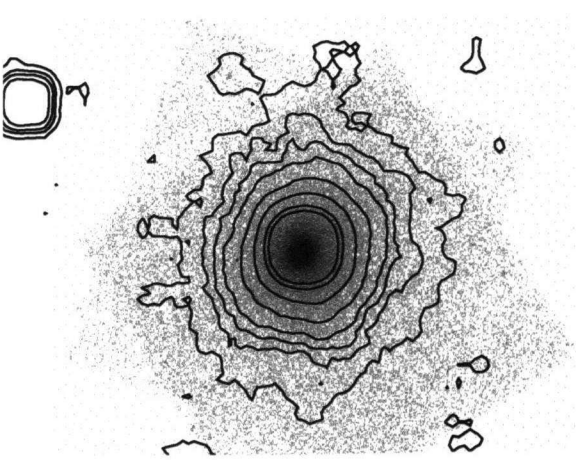

A1835 $z = 0.2530$

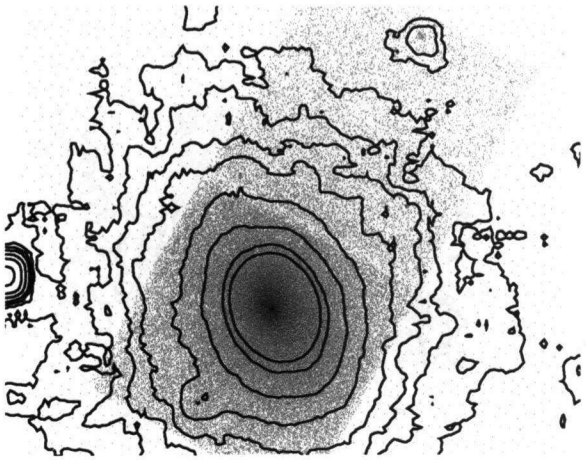

A2029 $z = 0.0780$

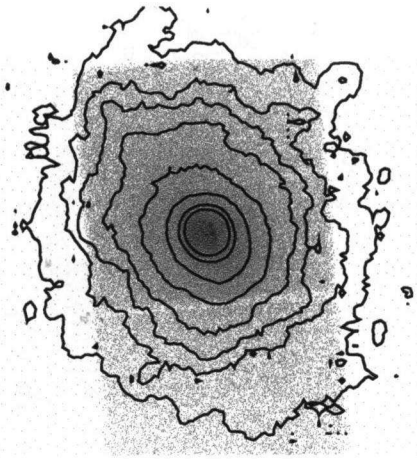

A2052 $z = 0.0345$

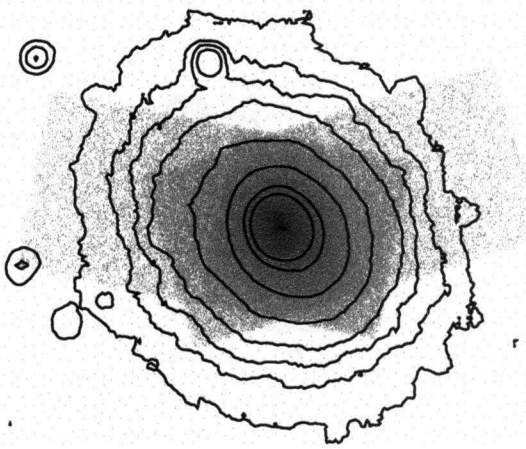

A2199 $z = 0.0310$

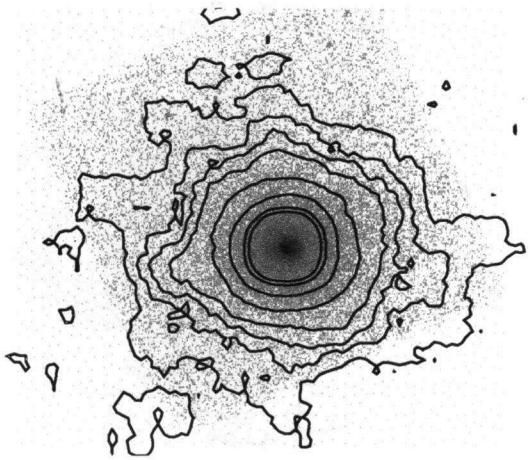

A2204 $z = 0.1511$

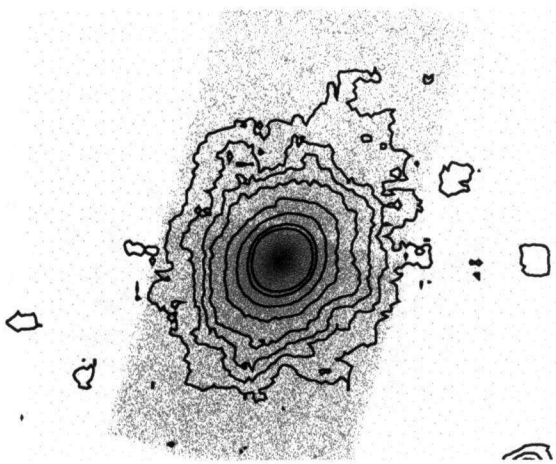

A2597 $z = 0.0822$

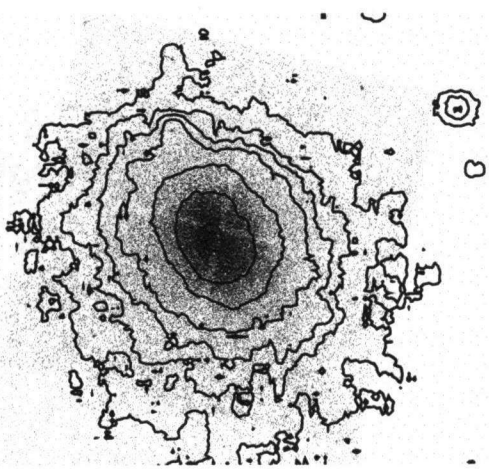

A401 $z = 0.0748$

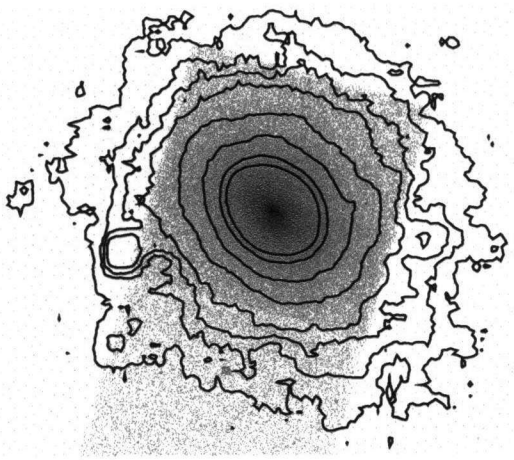

A478 $z = 0.0881$

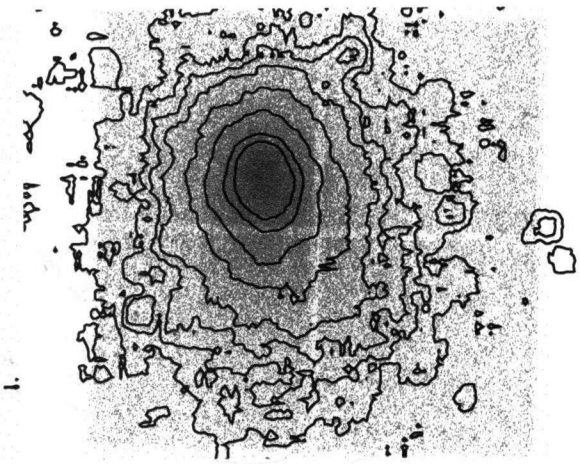

A644 $z = 0.0704$

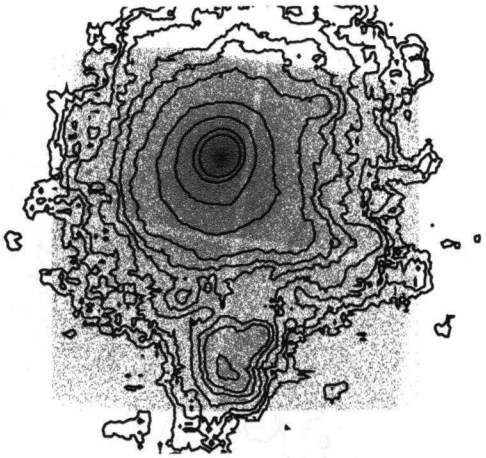

A85 $z = 0.0557$

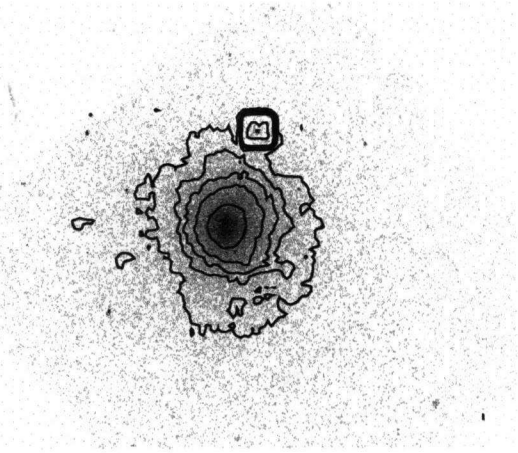

A963 $z = 0.2057$

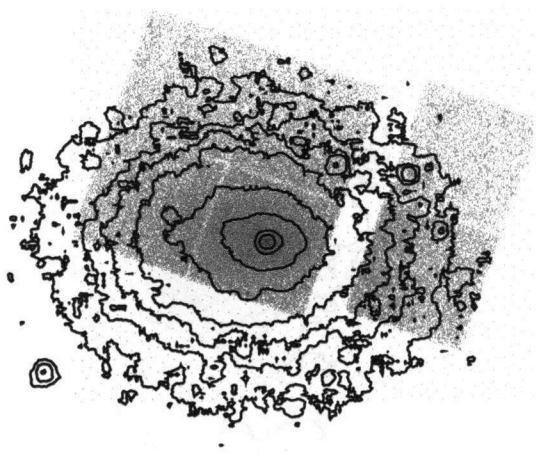

AWM7 $z = 0.0172$

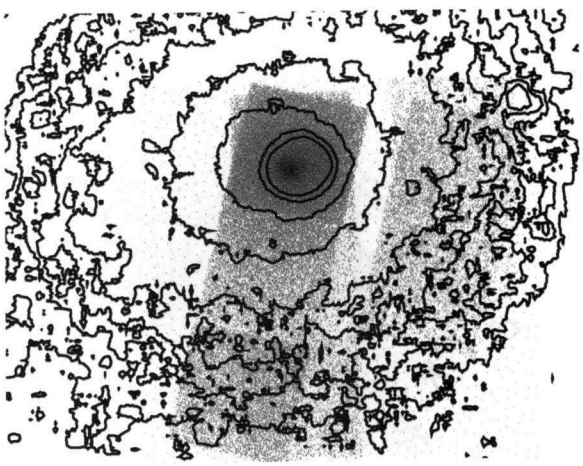

Centaurus cluster $z = 0.0110$

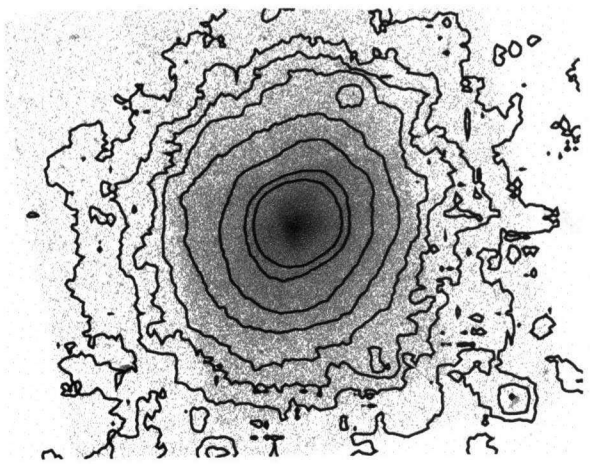

Hydra A $z = 0.0538$

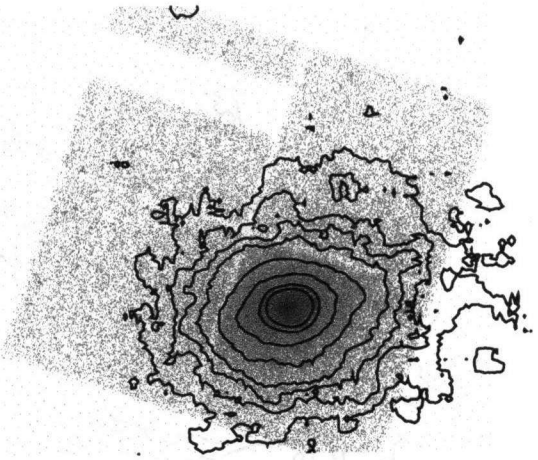

MKW3S $z = 0.0450$

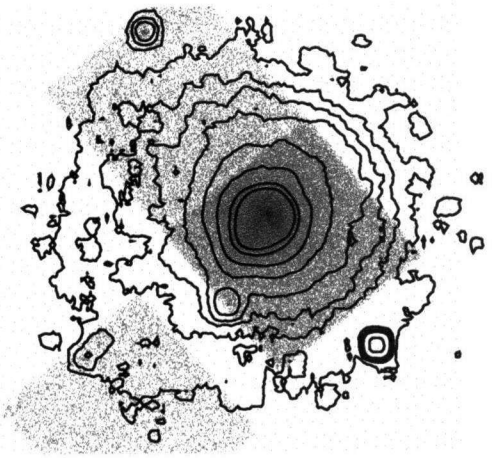

NGC5044 $z = 0.0892$

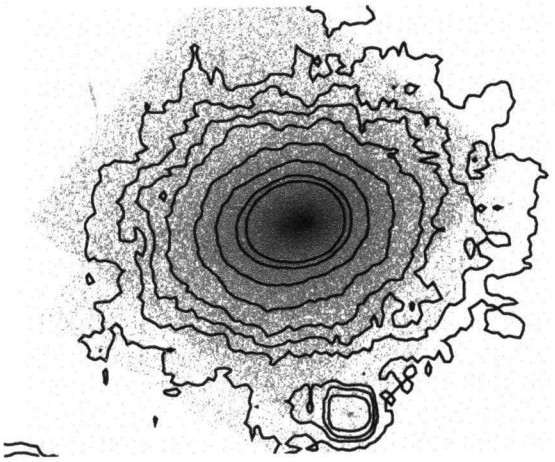

PKS0745-191 $z = 0.1028$

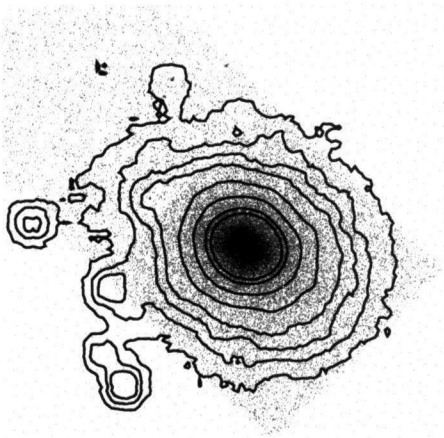

Sersic159-03 $z = 0.0580$

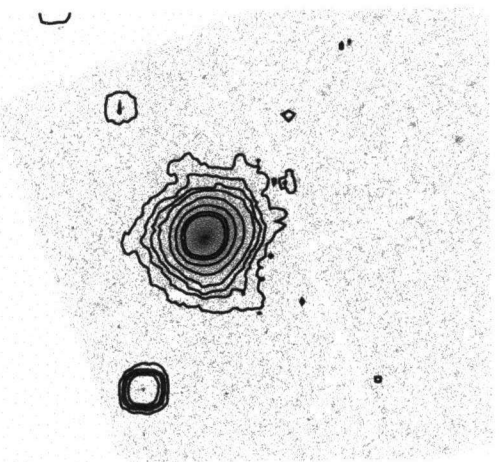

ZW3146 $z = 0.2906$

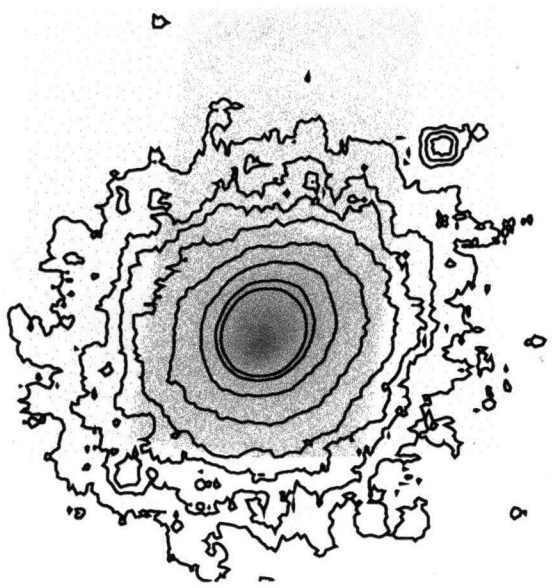

2A0335+096 $z = 0.0349$

Appendix B

Temperature, density, and pressure profiles of the sample clusters

The temperature, electron density, and pressure profiles of the 23 sample clusters are shown in this Appendix. The solid lines represent best-fit profiles with analytical functions (Equation (5.2) and Equation (2.26)). The pressure is simply derived from the temperature and gas density with the equation of state of the ideal gas: $P = n_e kT$.

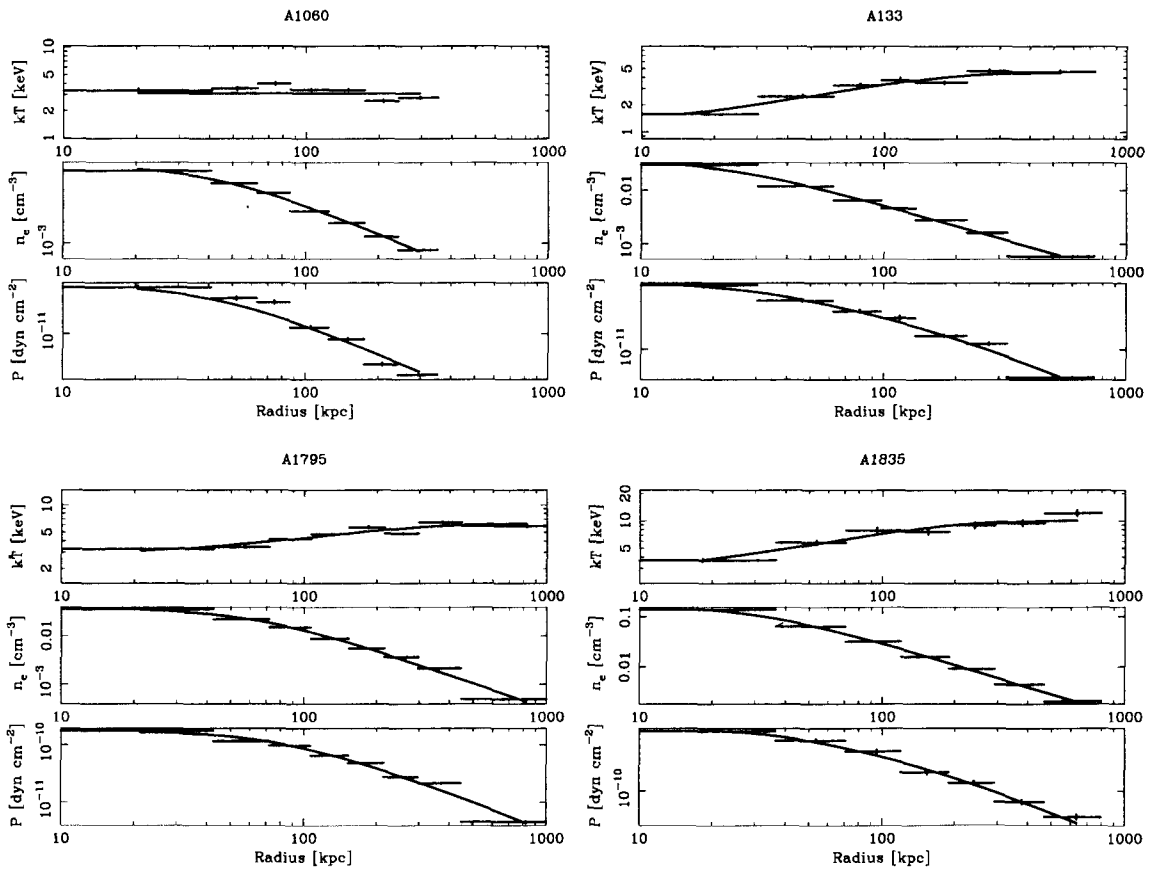

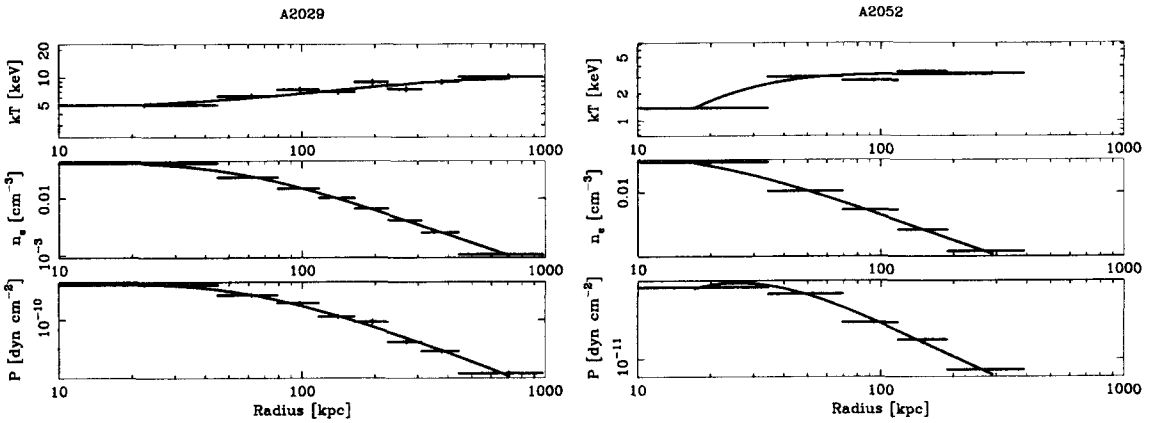
A2029
kT [keV]
n_e [cm^{-3}]
P [dyn cm^{-2}]
Radius [kpc]

A2052
kT [keV]
n_e [cm^{-3}]
P [dyn cm^{-2}]
Radius [kpc]

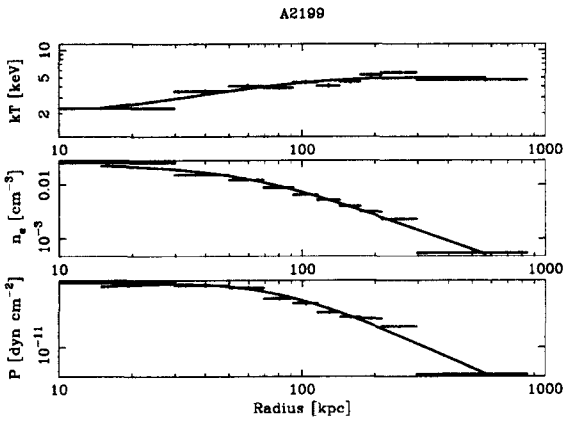
A2199
kT [keV]
n_e [cm^{-3}]
P [dyn cm^{-2}]
Radius [kpc]

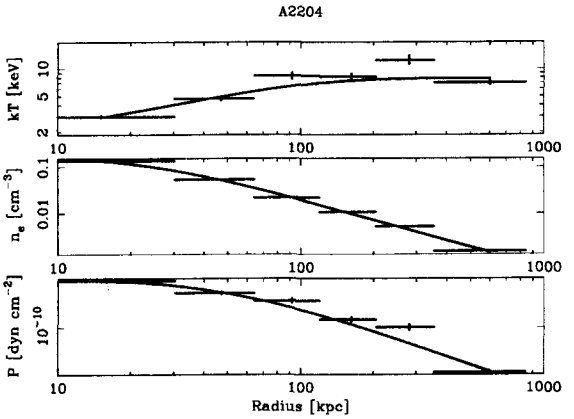
A2204
kT [keV]
n_e [cm^{-3}]
P [dyn cm^{-2}]
Radius [kpc]

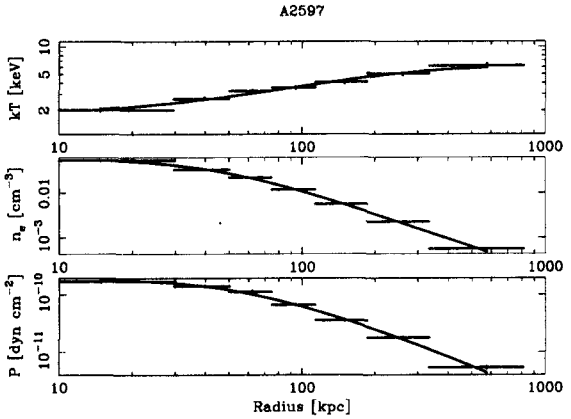
A2597
kT [keV]
n_e [cm^{-3}]
P [dyn cm^{-2}]
Radius [kpc]

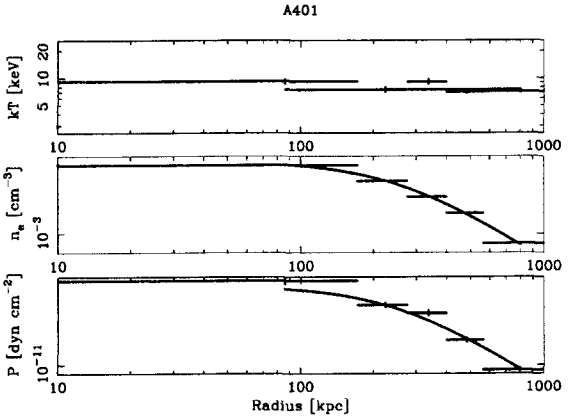
A401
kT [keV]
n_e [cm^{-3}]
P [dyn cm^{-2}]
Radius [kpc]

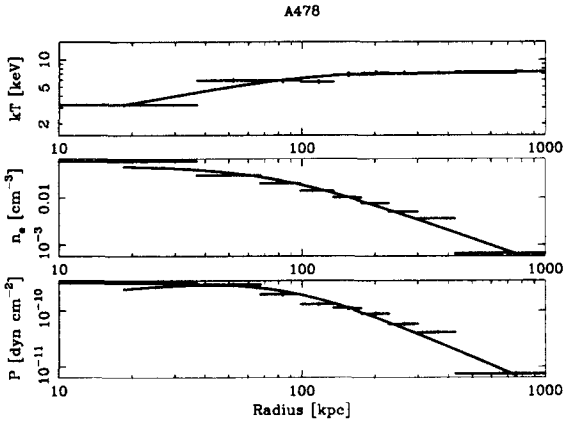
A478
kT [keV]
n_e [cm^{-3}]
P [dyn cm^{-2}]
Radius [kpc]

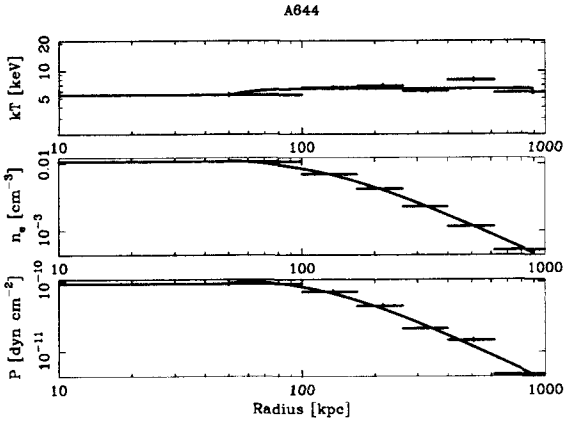
A644
kT [keV]
n_e [cm^{-3}]
P [dyn cm^{-2}]
Radius [kpc]

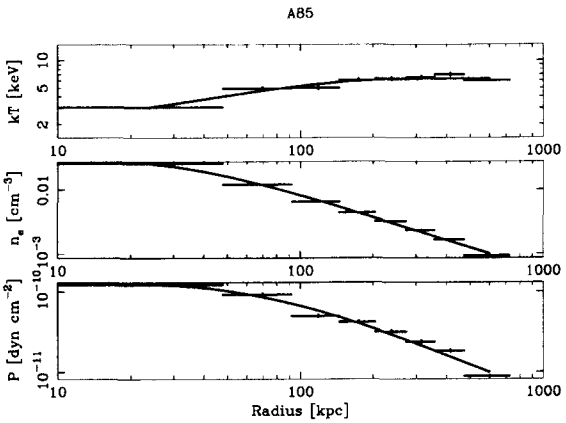
A85
kT [keV]
n_e [cm^{-3}]
P [dyn cm^{-2}]
Radius [kpc]

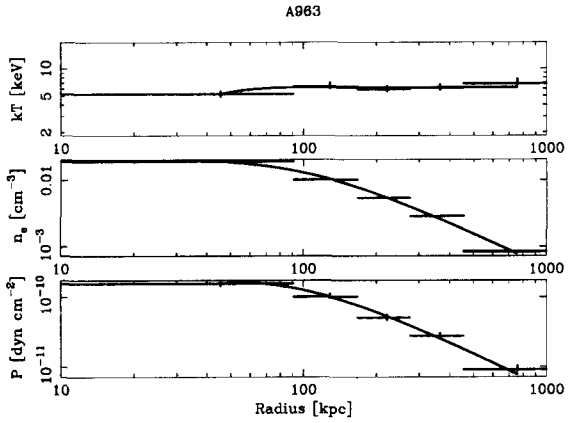
A963
kT [keV]
n_e [cm^{-3}]
P [dyn cm^{-2}]
Radius [kpc]

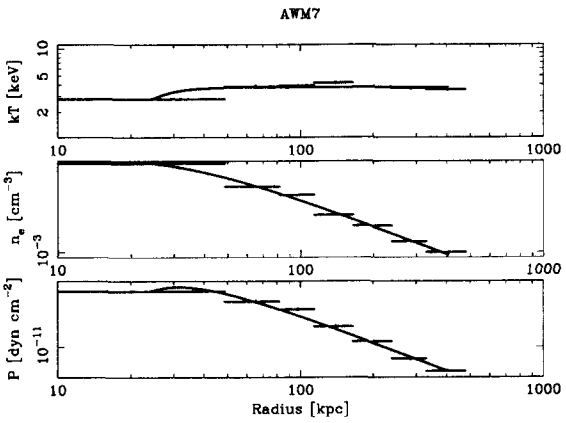
AWM7
kT [keV]
n_e [cm^{-3}]
P [dyn cm^{-2}]
Radius [kpc]

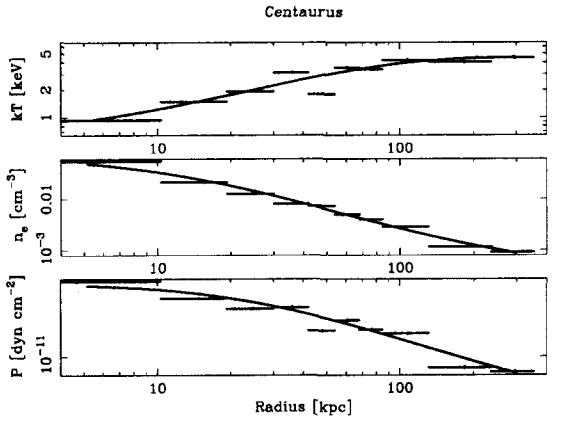
Centaurus
kT [keV]
n_e [cm^{-3}]
P [dyn cm^{-2}]
Radius [kpc]

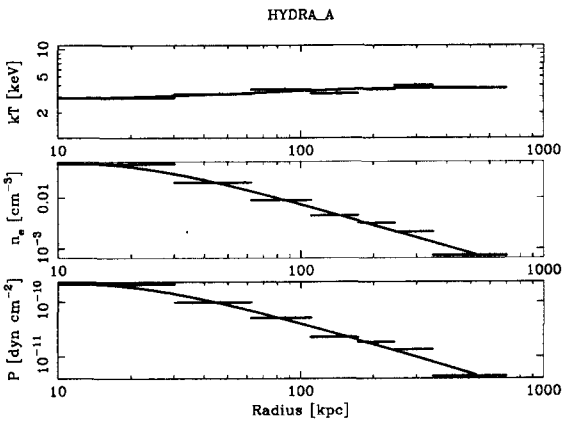
HYDRA_A
kT [keV]
n_e [cm^{-3}]
P [dyn cm^{-2}]
Radius [kpc]

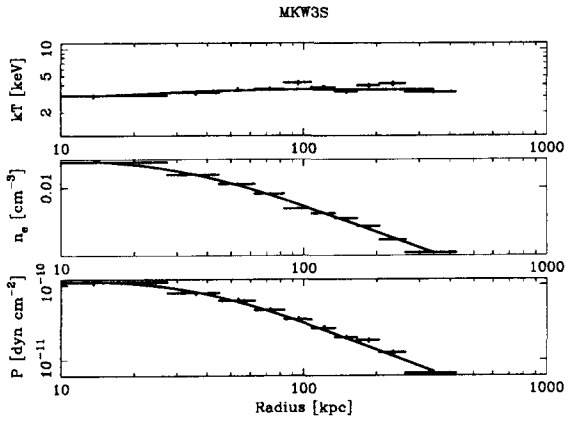
MKW3S
kT [keV]
n_e [cm^{-3}]
P [dyn cm^{-2}]
Radius [kpc]

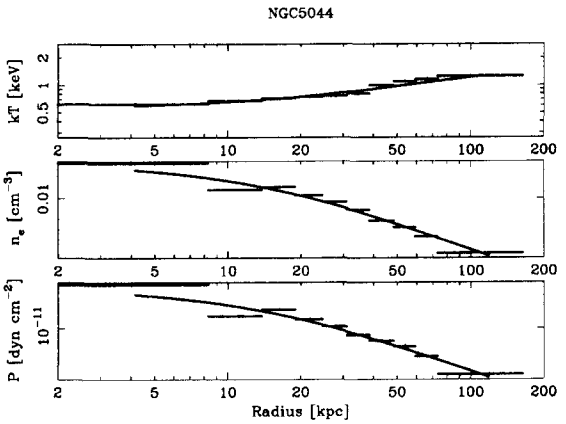
NGC5044
kT [keV]
n_e [cm^{-3}]
P [dyn cm^{-2}]
Radius [kpc]

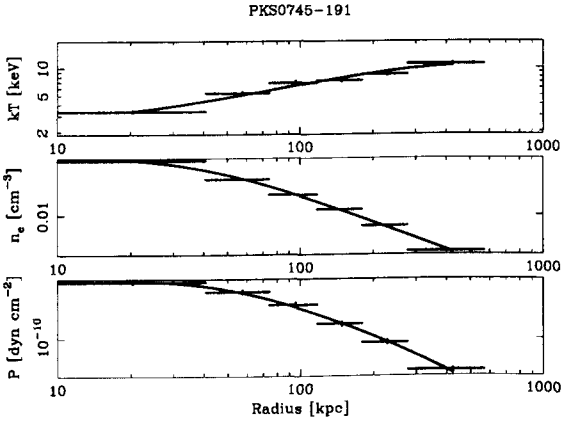
PKS0745-191
kT [keV]
n_e [cm^{-3}]
P [dyn cm^{-2}]
Radius [kpc]

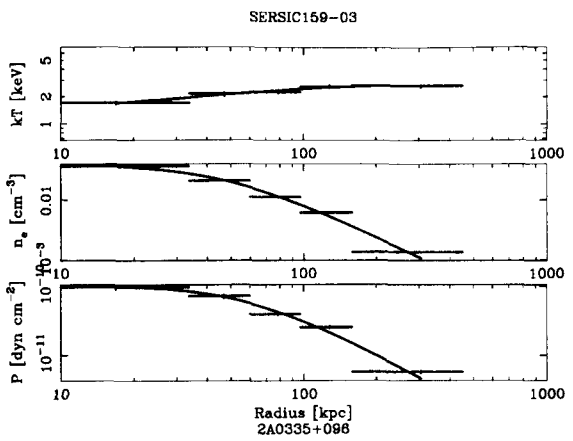
SERSIC159-03
kT [keV]
1
2
5
10
100
1000
n_e [cm^{-3}]
0.1
0.01
10^{-3}
P [dyn cm^{-2}]
10^{-10}
10^{-11}
Radius [kpc]

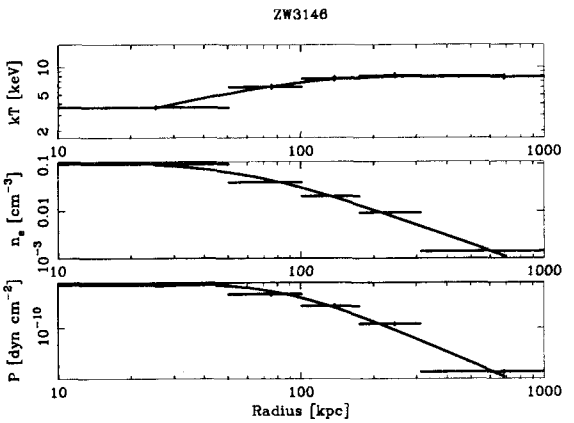
ZW3146
kT [keV]
2
5
10
100
1000
n_e [cm^{-3}]
0.1
0.01
10^{-3}
P [dyn cm^{-2}]
10^{-10}
Radius [kpc]

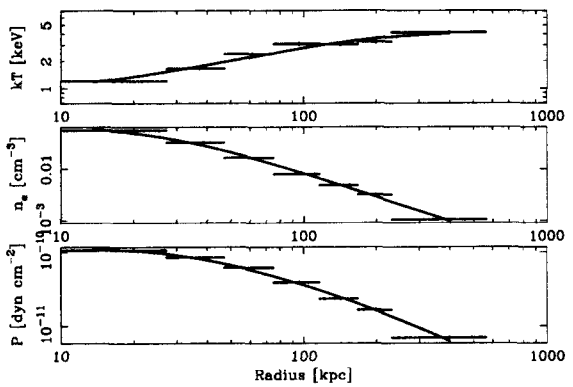
2A0335+096
kT [keV]
1
2
5
10
100
1000
n_e [cm^{-3}]
0.01
10^{-3}
P [dyn cm^{-2}]
10^{-10}
10^{-11}
Radius [kpc]

Appendix C

Mass profiles of the sample clusters

The mass profiles of the 23 sample clusters are shown in this Appendix. The solid curves represent the mass profile derived from the best-fit parameters of Equation (5.2) and Equation (2.26). The dashed lines are a confidence level of 68 %. The discrete data with error bars represent the mass profile calculated using approximate expression given by 5.5.

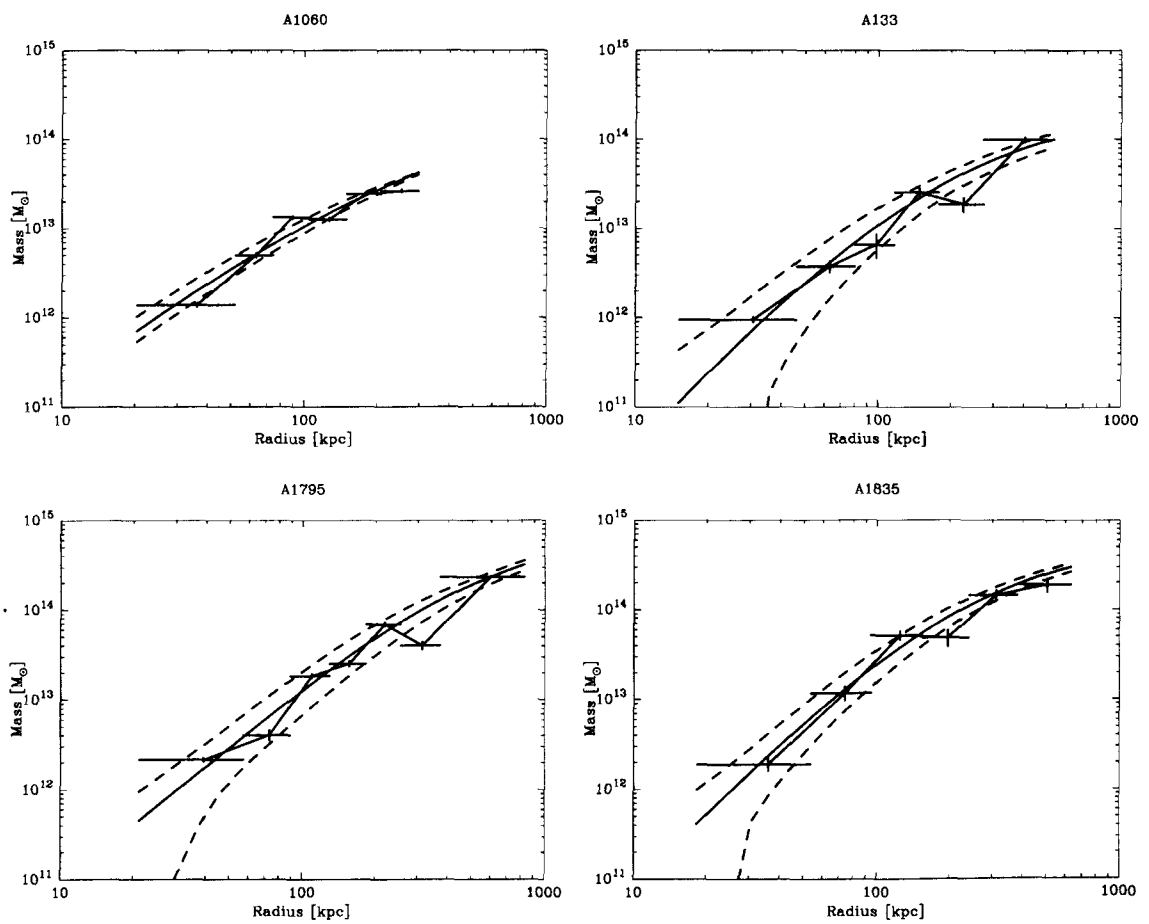

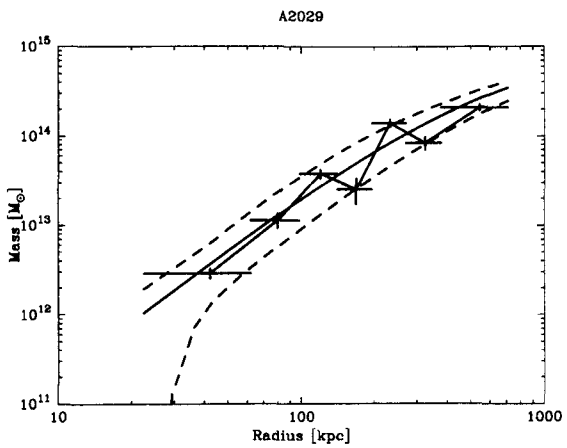
A2029
Mass [M⊙]
Radius [kpc]

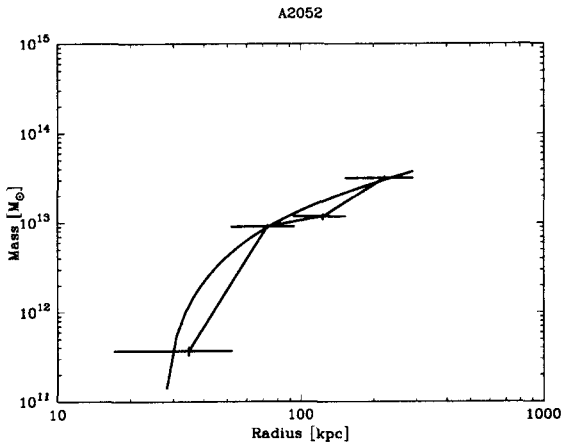
A2052
Mass [M⊙]
Radius [kpc]

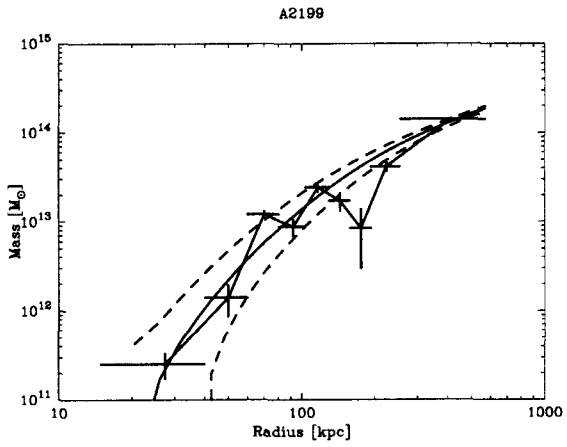
A2199
Mass [M⊙]
Radius [kpc]

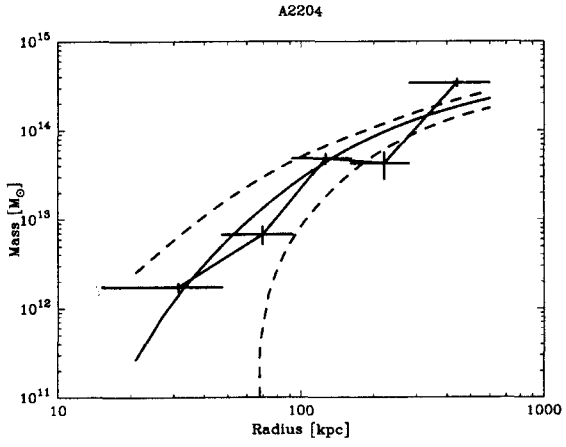
A2204
Mass [M⊙]
Radius [kpc]

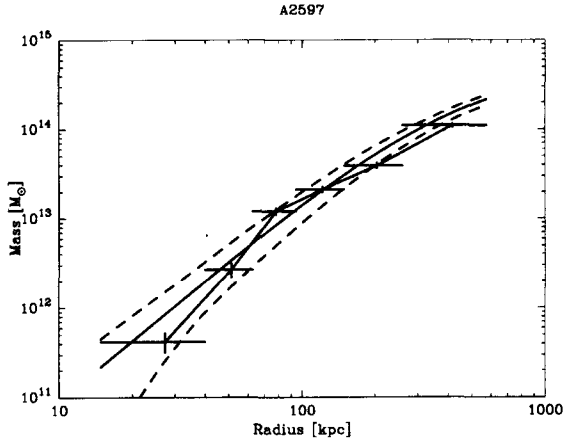
A2597
Mass [M⊙]
Radius [kpc]

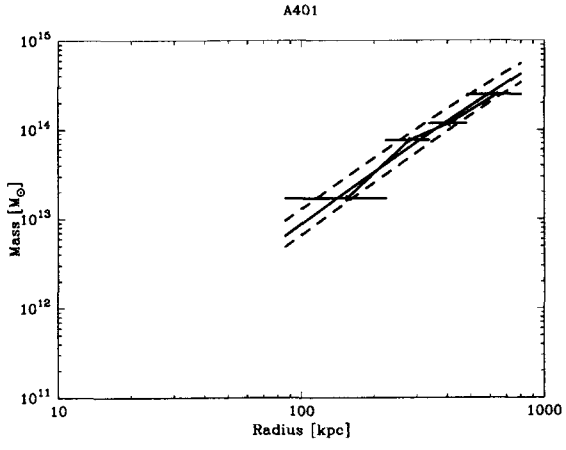
A401
Mass [M⊙]
Radius [kpc]

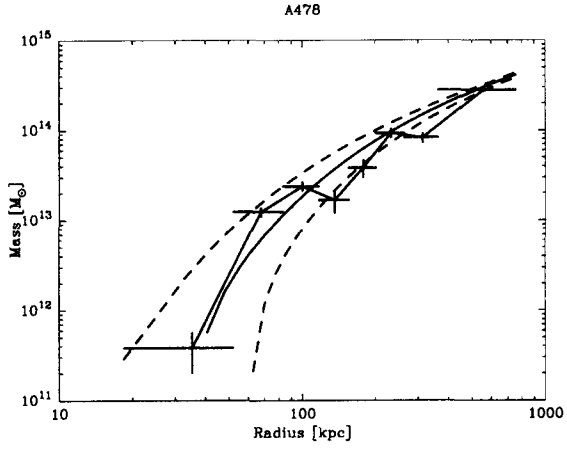
A478
Mass [M⊙]
Radius [kpc]

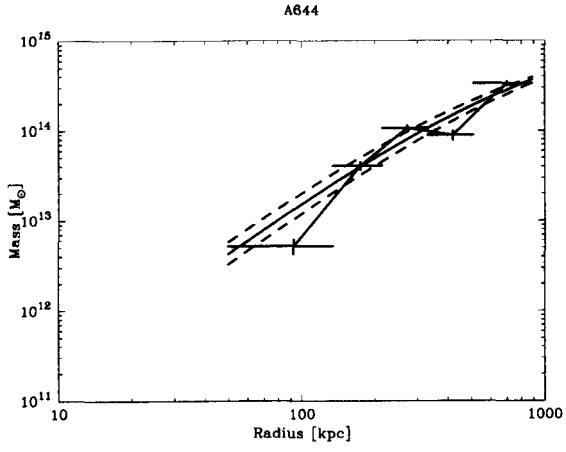
A644
Mass [M⊙]
Radius [kpc]

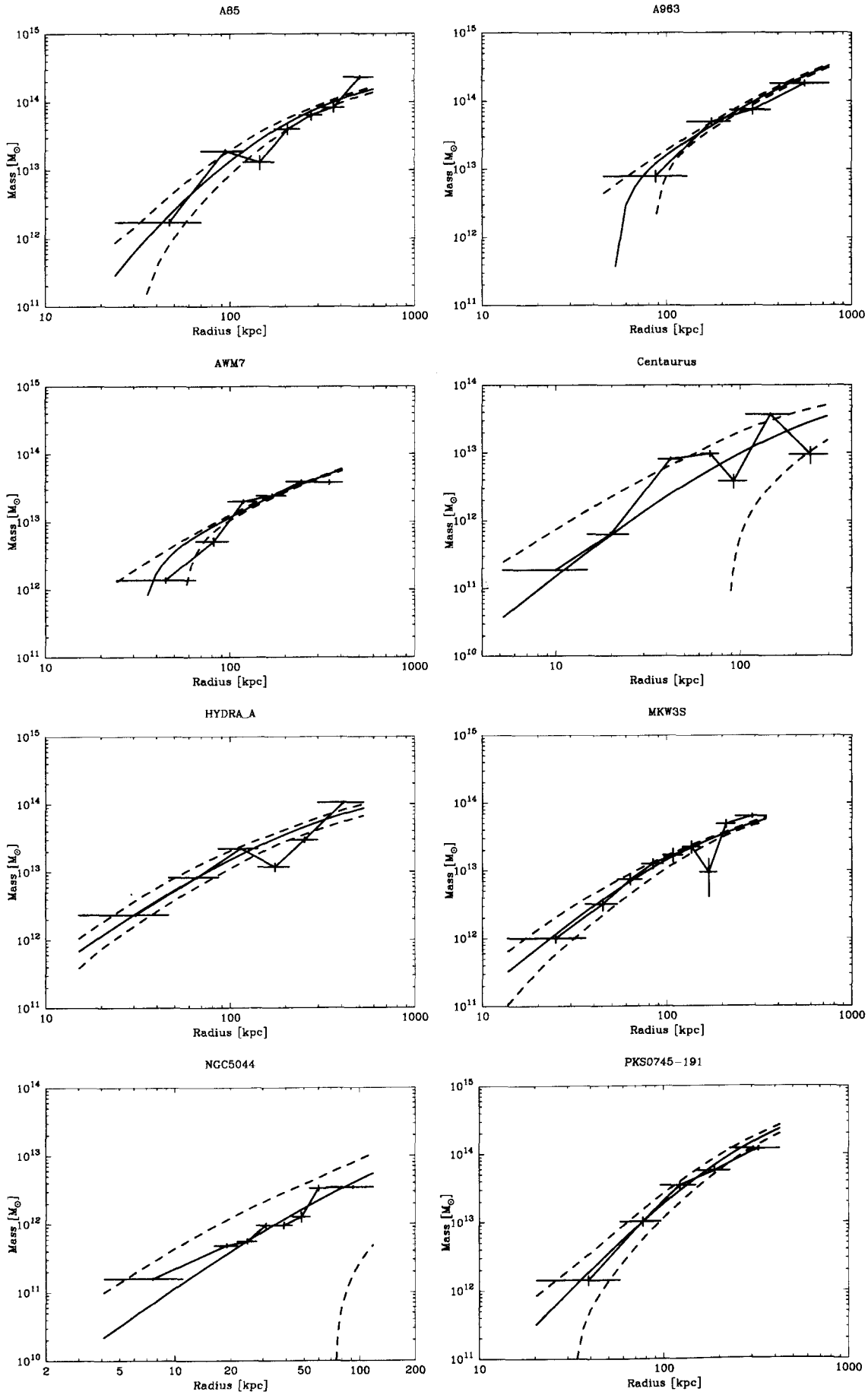
A85
A963
AWM7
Centaurus
HYDRA_A
MKW3S
NGC5044
PKS0745−191
Mass [M⊙]
Radius [kpc]

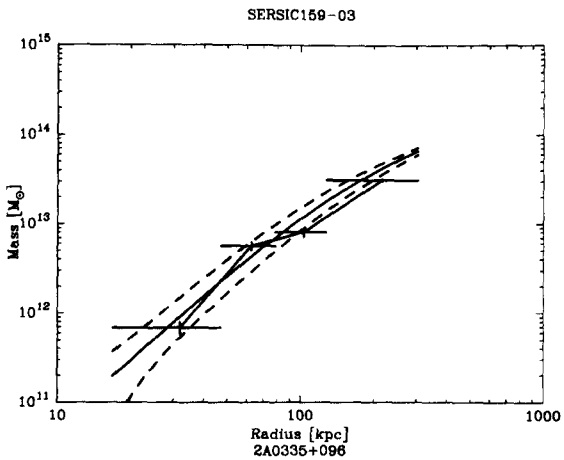
SERSIC159-03
Mass [M⊙]
Radius [kpc]

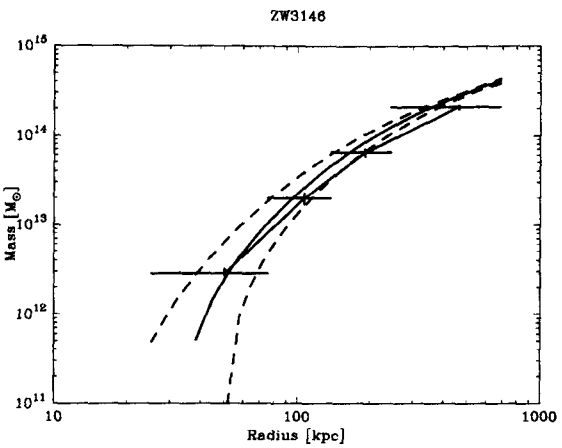
ZW3146
Mass [M⊙]
Radius [kpc]

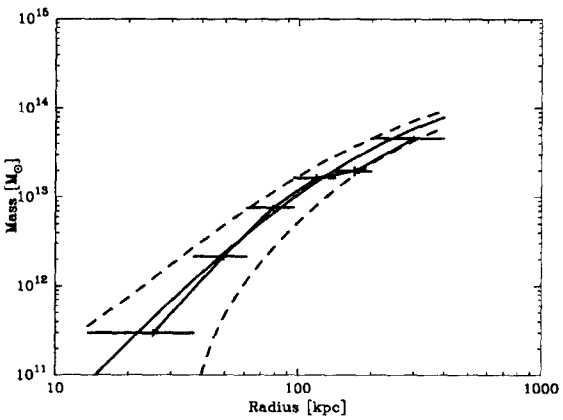
2A0335+096
Mass [M⊙]
Radius [kpc]

Appendix D

Fitting results of the mass profiles with the King model and NFW model

In this appendix, we show the best-fit King profiles (solid lines) and NFW profiles (dashed lines) to the mass profiles of the 23 sample cluster.

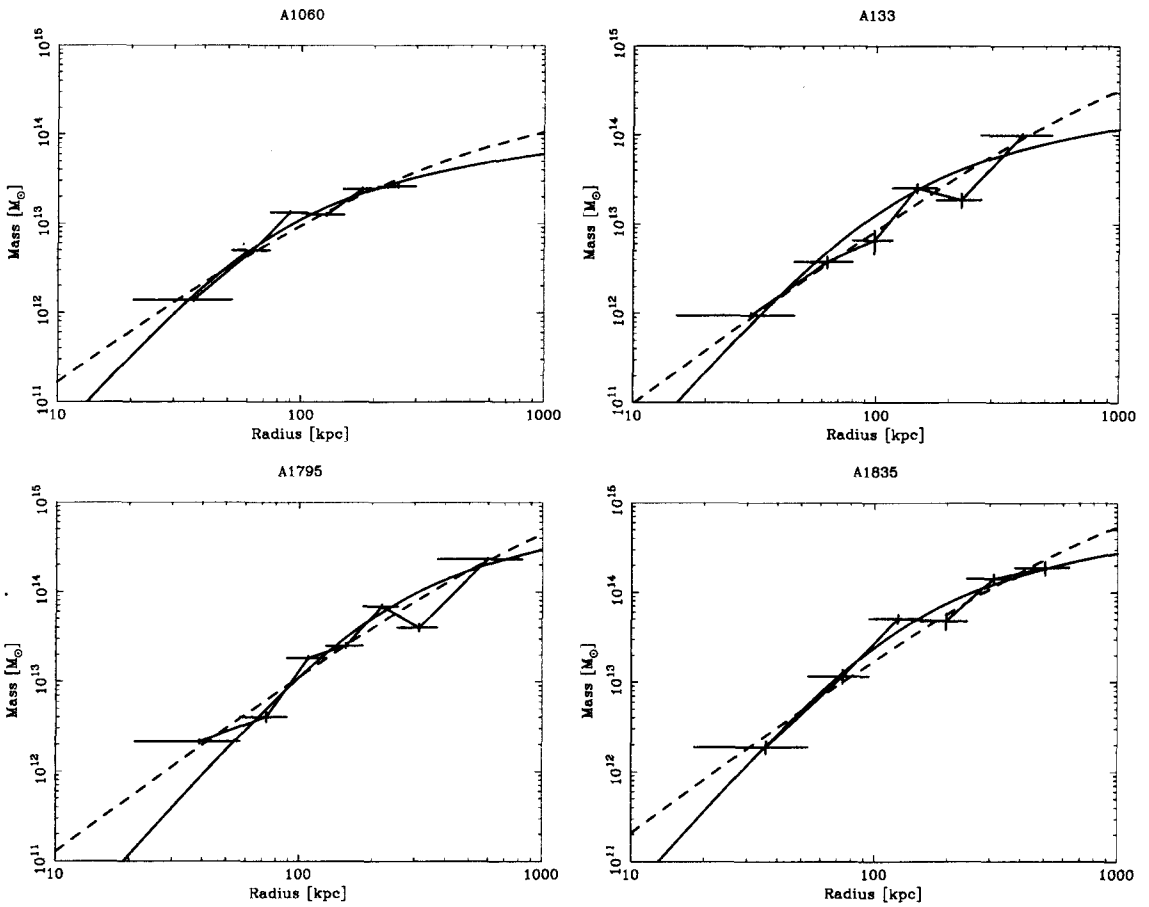

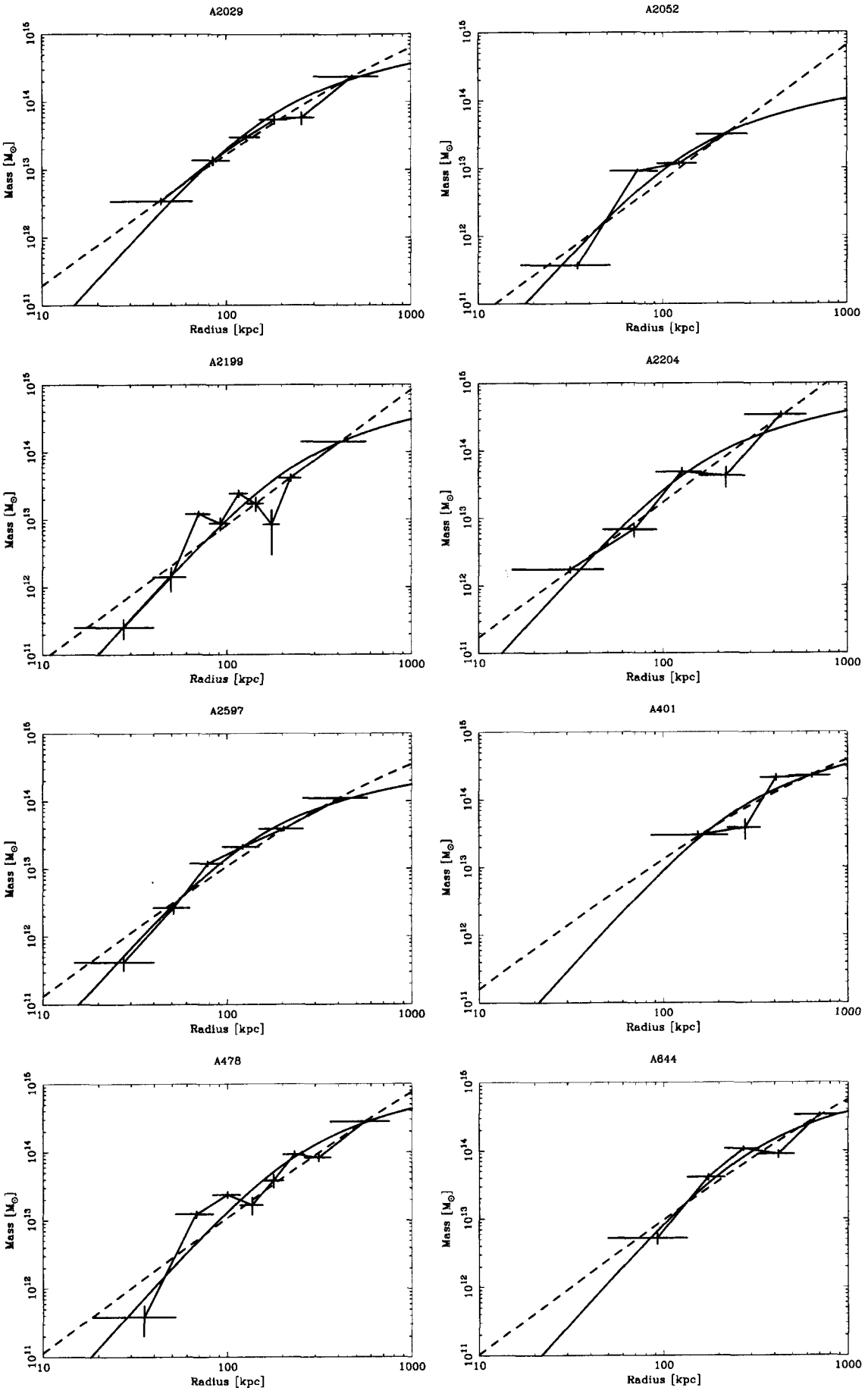
A2029
A2052
A2199
A2204
A2597
A401
A478
A644
Mass [M⊙]
Radius [kpc]
10
100
1000
10^11
10^12
10^13
10^14
10^15

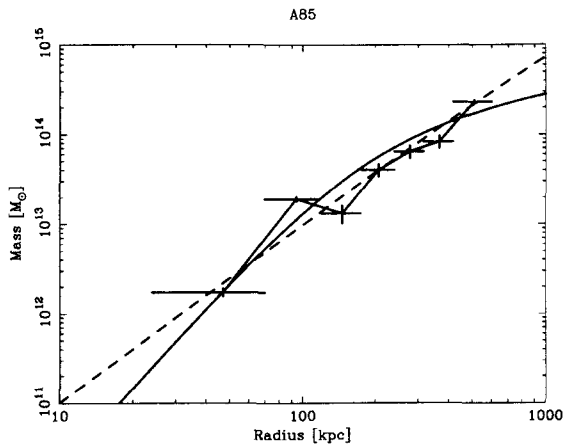
A85
Mass [M⊙]
Radius [kpc]

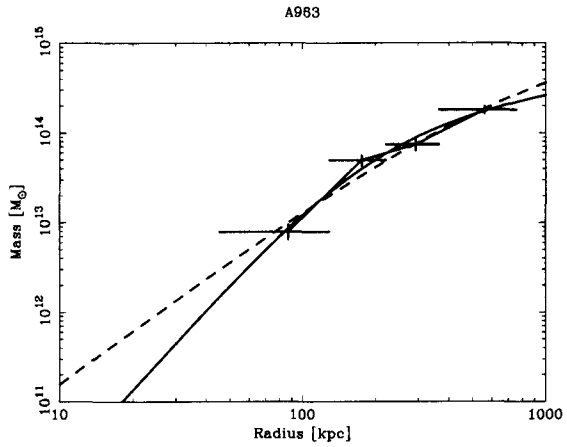
A963
Mass [M⊙]
Radius [kpc]

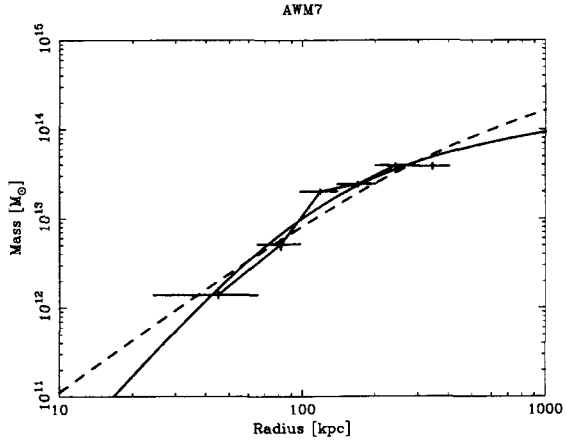
AWM7
Mass [M⊙]
Radius [kpc]

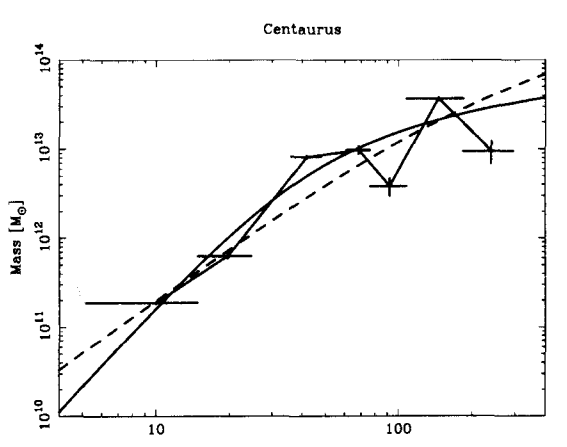
Centaurus
Mass [M⊙]

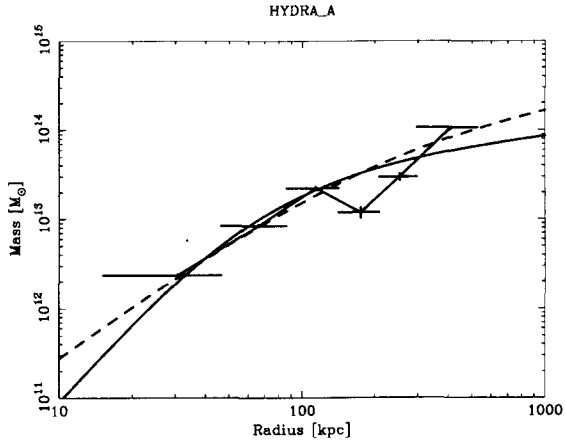
HYDRA_A
Mass [M⊙]
Radius [kpc]

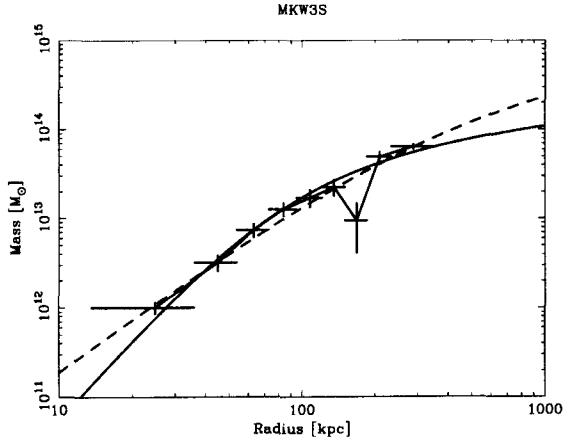
MKW3S
Mass [M⊙]
Radius [kpc]

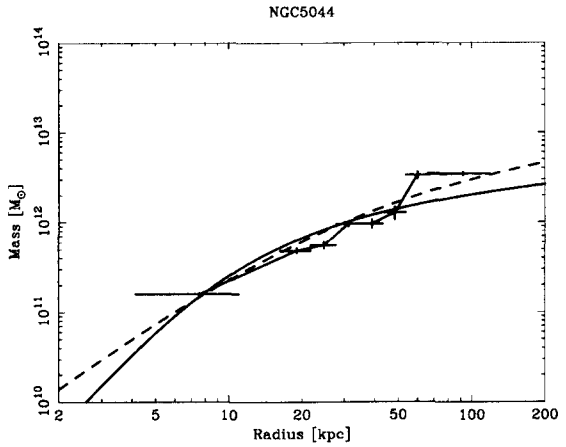
NGC5044
Mass [M⊙]
Radius [kpc]

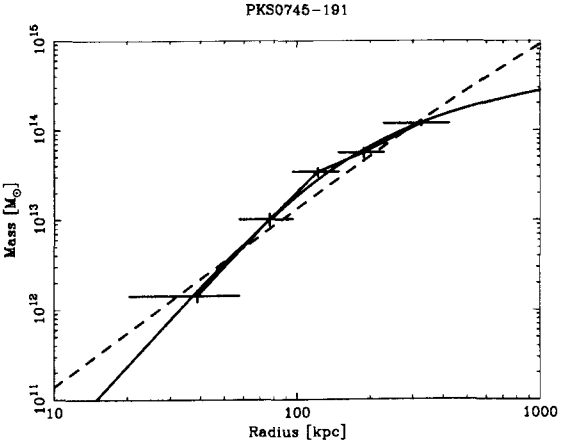
PKS0745-191
Mass [M⊙]
Radius [kpc]

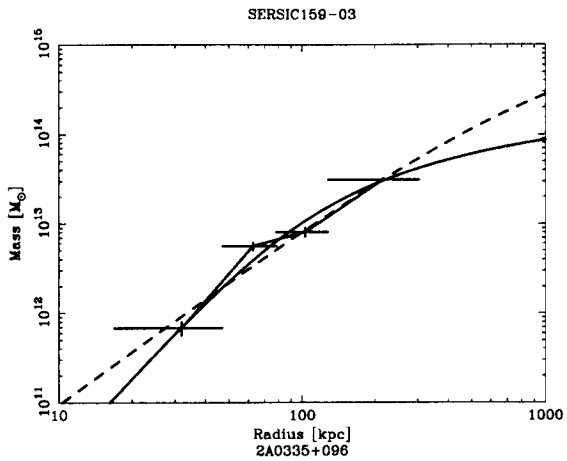
SERSIC159-03
Mass [M⊙]
Radius [kpc]

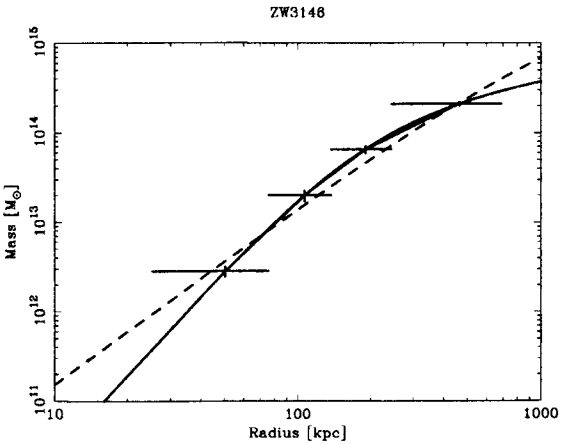
ZW3146
Mass [M⊙]
Radius [kpc]

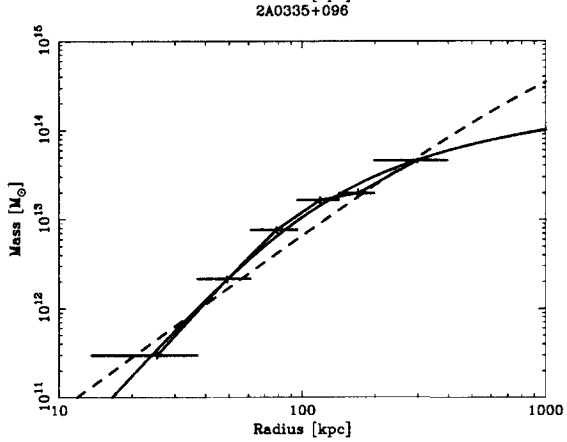
2A0335+096
Mass [M⊙]
Radius [kpc]

Appendix E

Fitting results of the mass profiles with the general form of the density profile

In this appendix, we show the best-fit mass models using the general form of the density profile. The horizontal dashed lines represent the radius of $r_0 = 0.02r_{200}$. The red lines represent the best-fit slope ($M \propto r^{3-\alpha_0}$ at the radius r_0. A401, A644, and A963 are removed because of the lack of the data within $0.02r_{200}$.

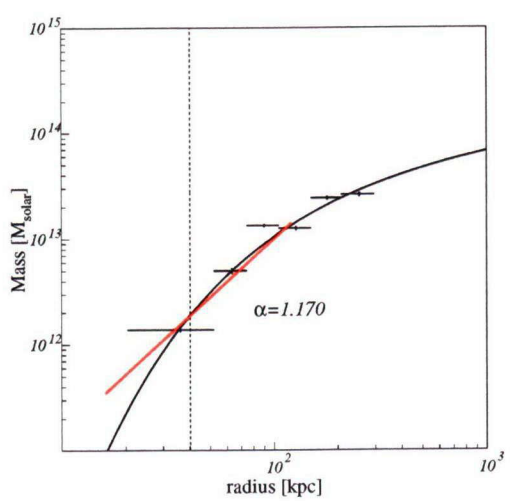

A1060 $0.02r_{200} = 40.2$ kpc

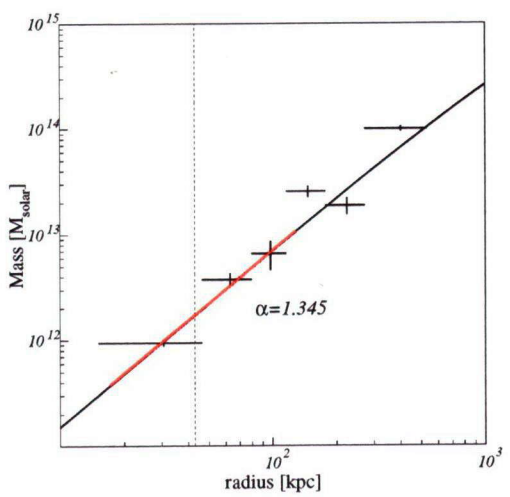

A133 $0.02r_{200} = 42.9$ kpc

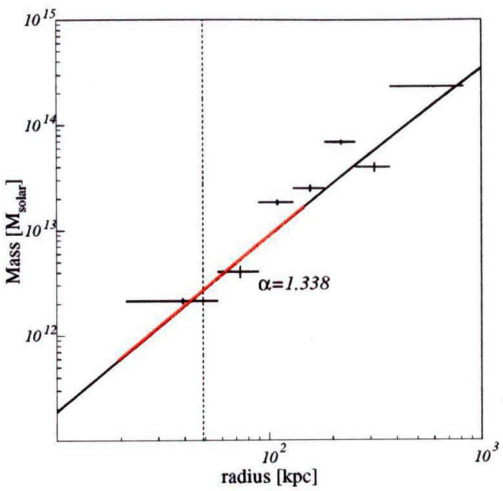

A1795 $0.02r_{200} = 48.8$ kpc

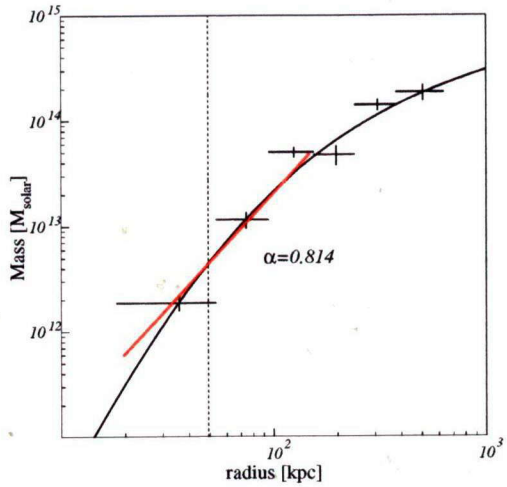

A1835 $0.02r_{200} = 49.2$ kpc

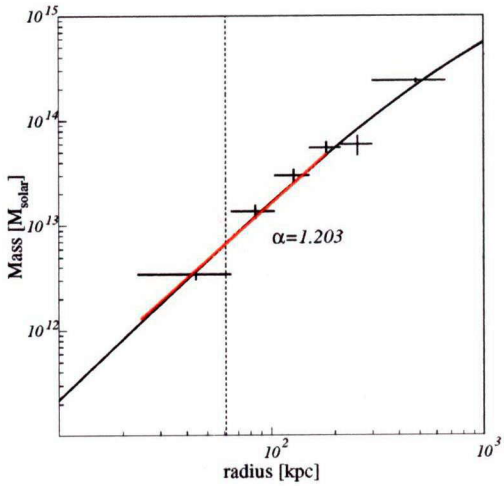

A2029 $0.02r_{200} = 61.0$ kpc

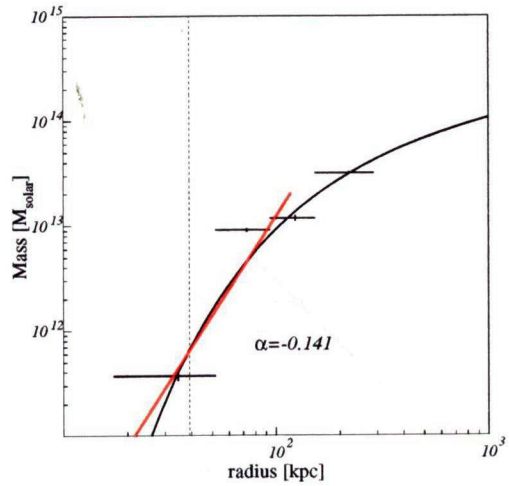

A2052 $0.02r_{200} = 39.2$ kpc

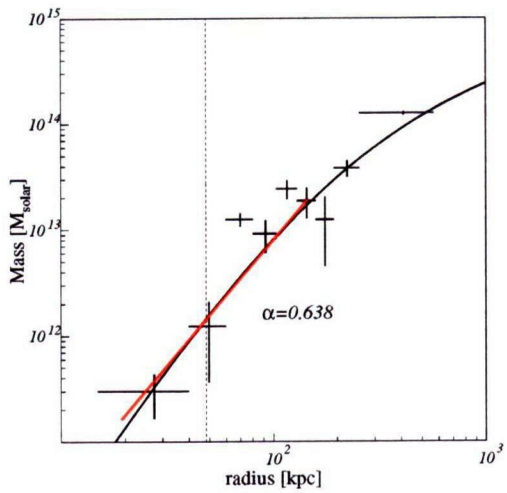

A2199 $0.02r_{200} = 48.2$ kpc

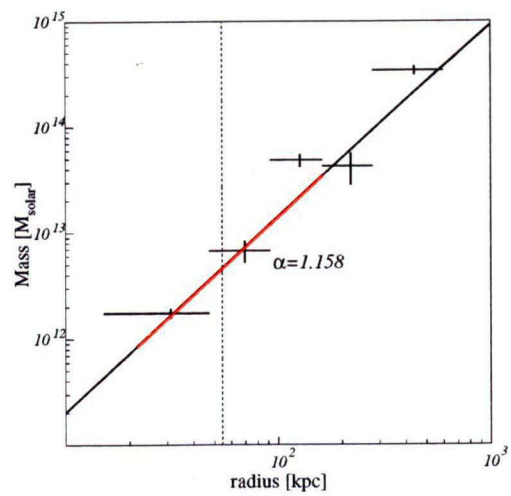

A2204 $0.02r_{200} = 54.4$ kpc

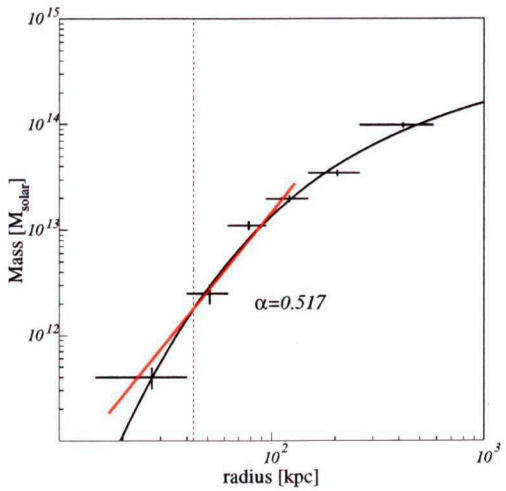

A2597 $0.02r_{200} = 42.9$ kpc

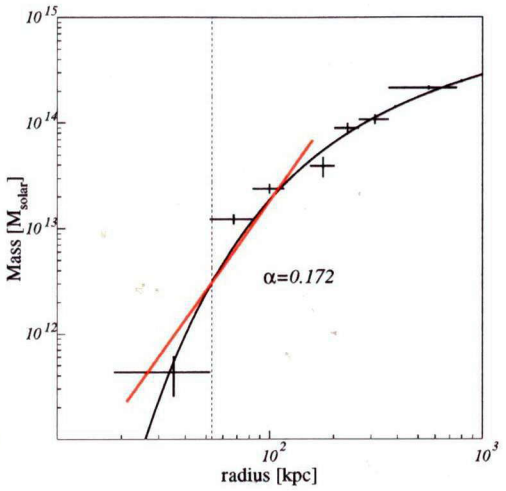

A478 $0.02r_{200} = 53.1$ kpc

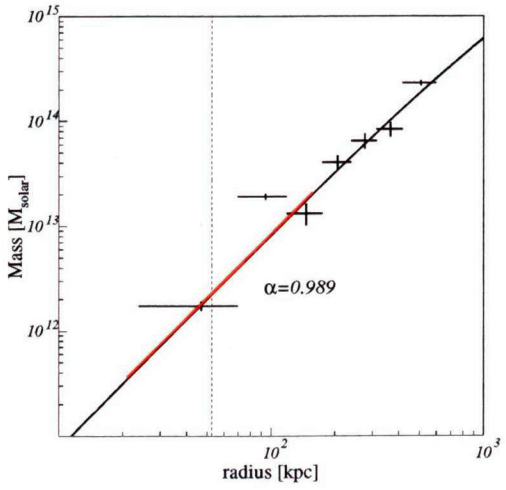

A85 $0.02r_{200} = 52.6$ kpc

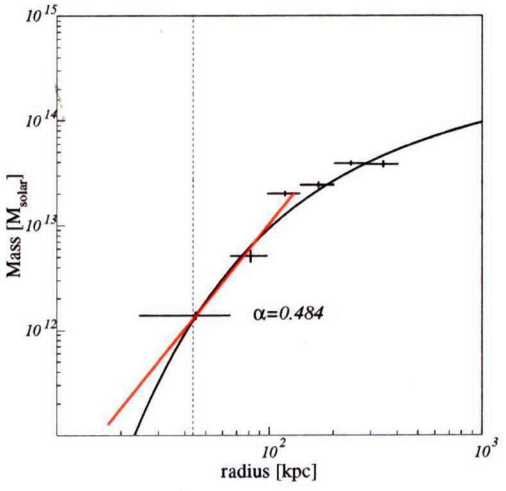

AWM7 $0.02r_{200} = 43.6$ kpc

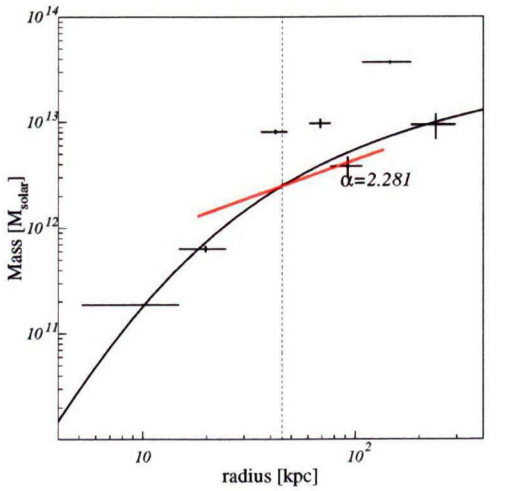

Centaurus cluster $0.02r_{200} = 45.3$ kpc

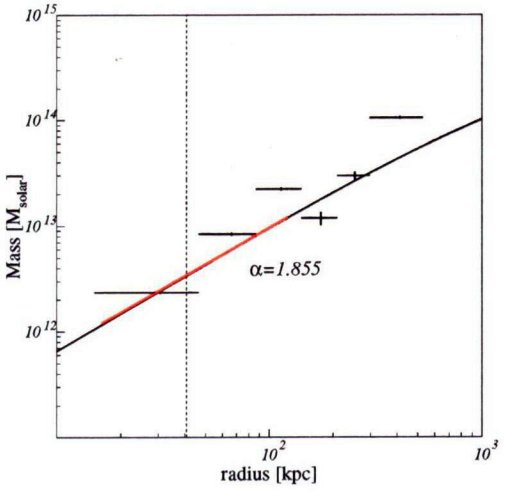

Hydra A $0.02r_{200} = 40.8$ kpc

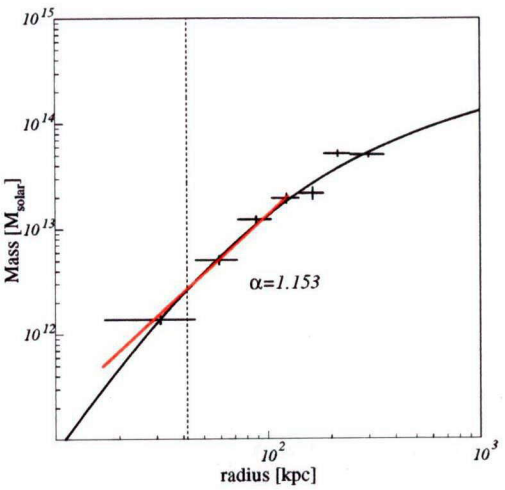

MKW3S $0.02r_{200} = 41.6$ kpc

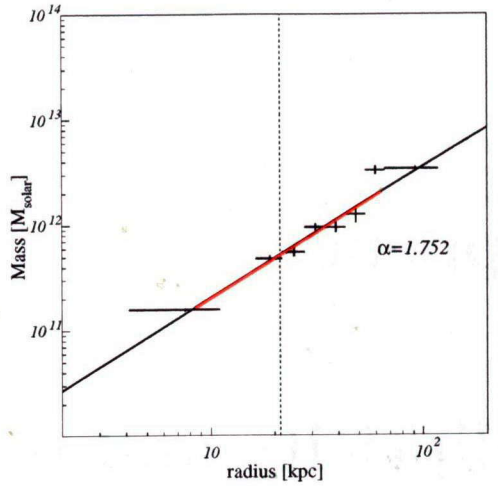

NGC5044 $0.02r_{200} = 21.2$ kpc

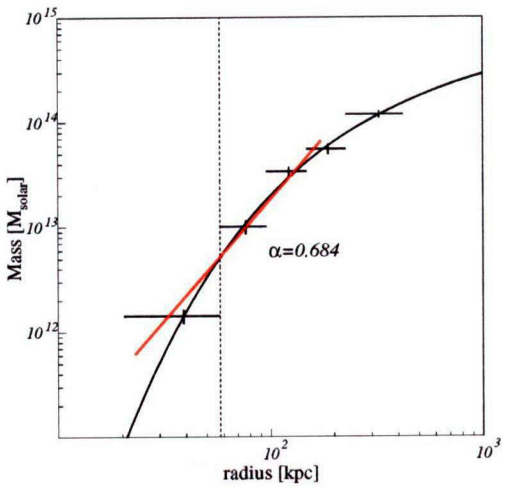

PKS0745-191 $0.02r_{200} = 57.7$ kpc

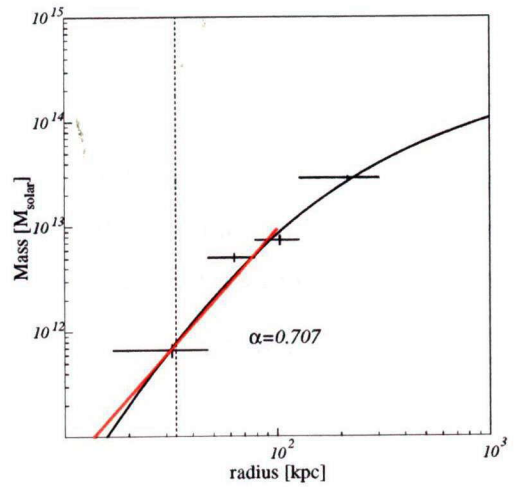

Sersic159-03 $0.02r_{200} = 33.4$ kpc

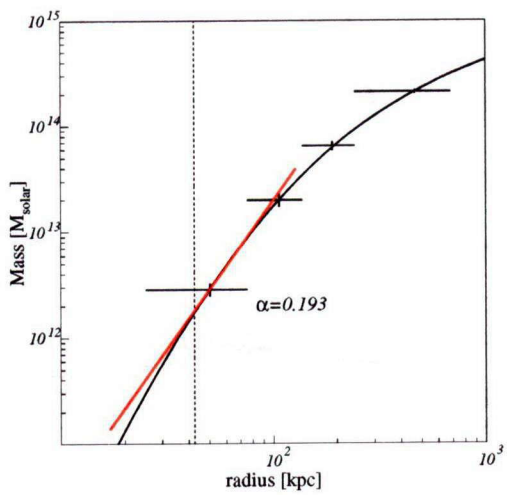

ZW3146 $0.02r_{200} = 42.6$ kpc

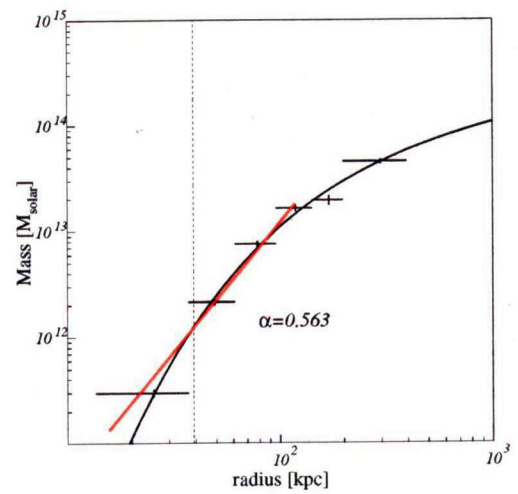

2A0335+096 $0.02r_{200} = 39.2$ kpc

Appendix F

Ellipticity and position angle of the sample clusters

In this appendix, we show the ellipticity and position profiles angle of the sample clusters as a function of radius computed from the source-free *Chandra* image (black) and *ROSAT* image (red). The definition of the ellipticity and position angle are shown in §5.6.2.

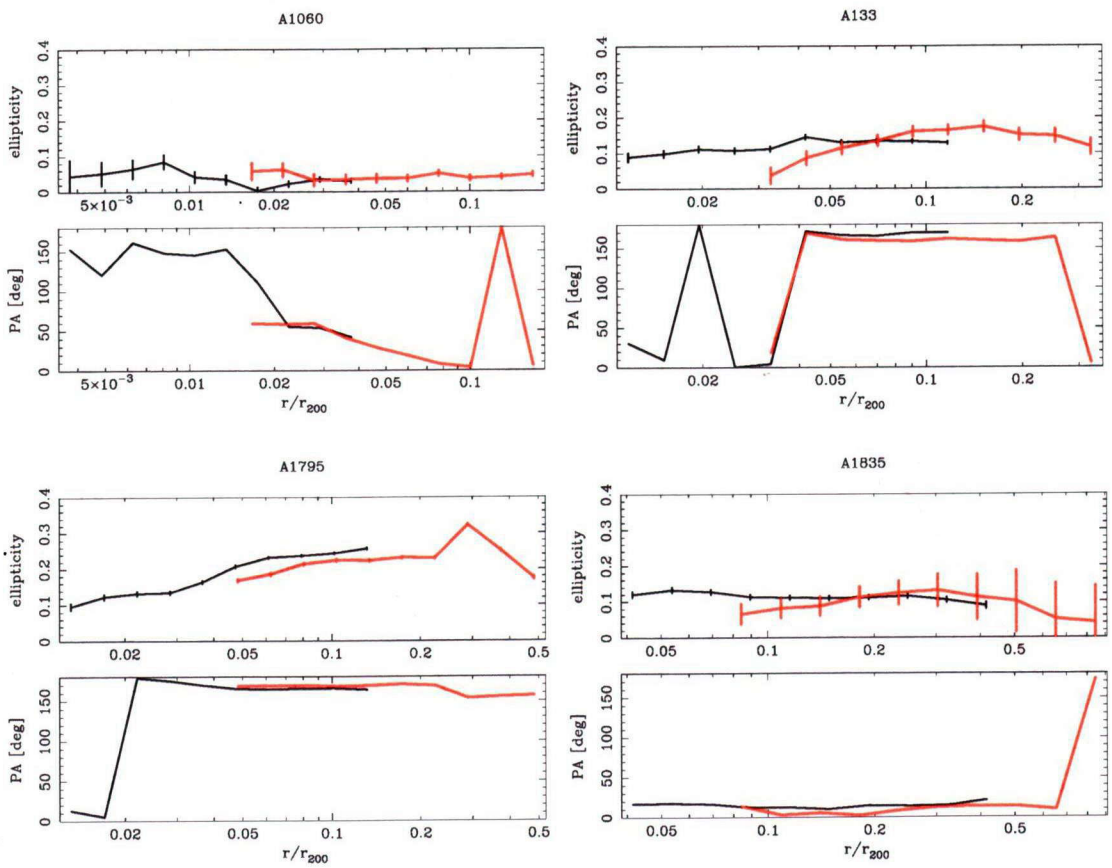

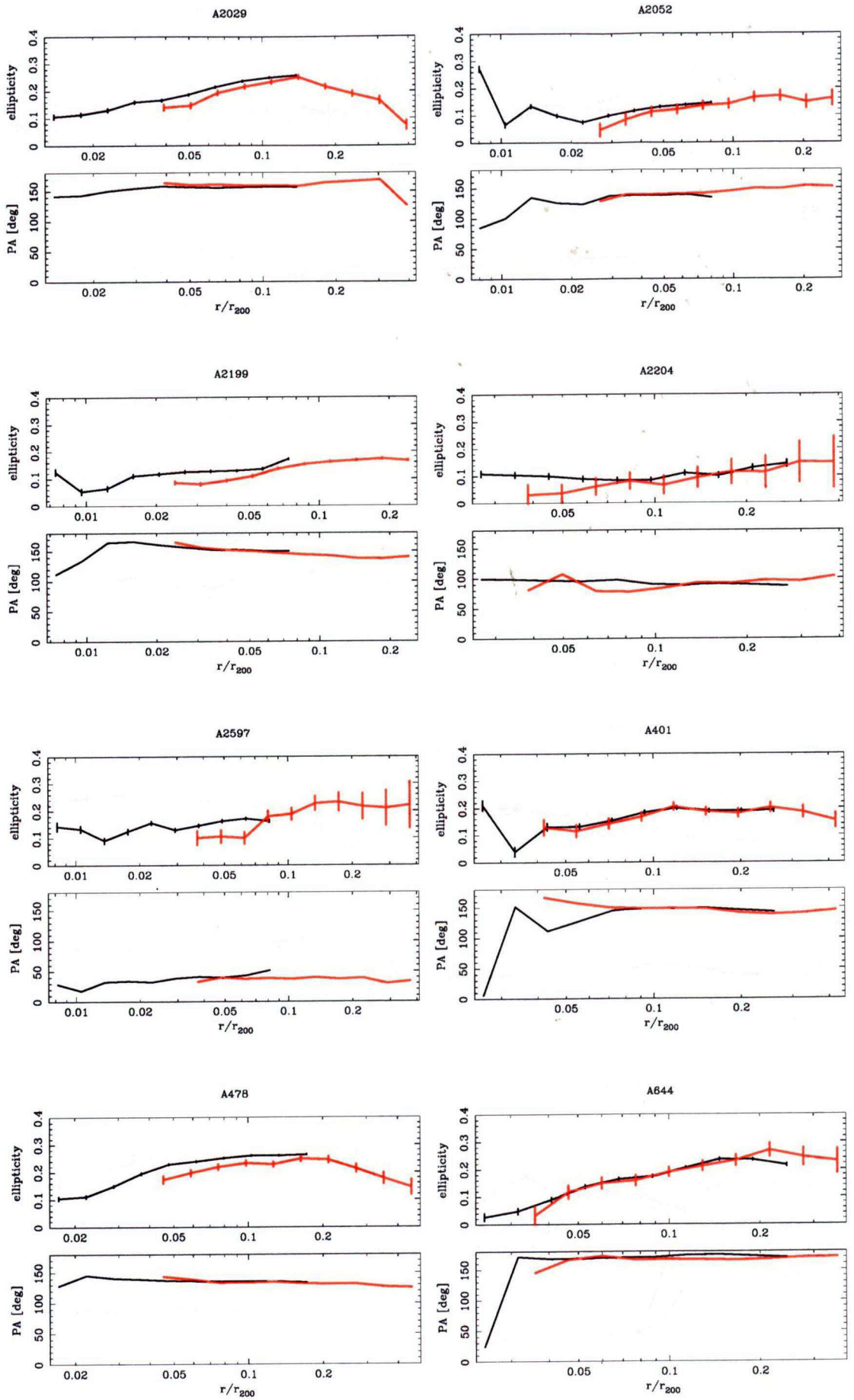
A2029
A2052
A2199
A2204
A2597
A401
A478
A644
ellipticity
PA [deg]
r/r200

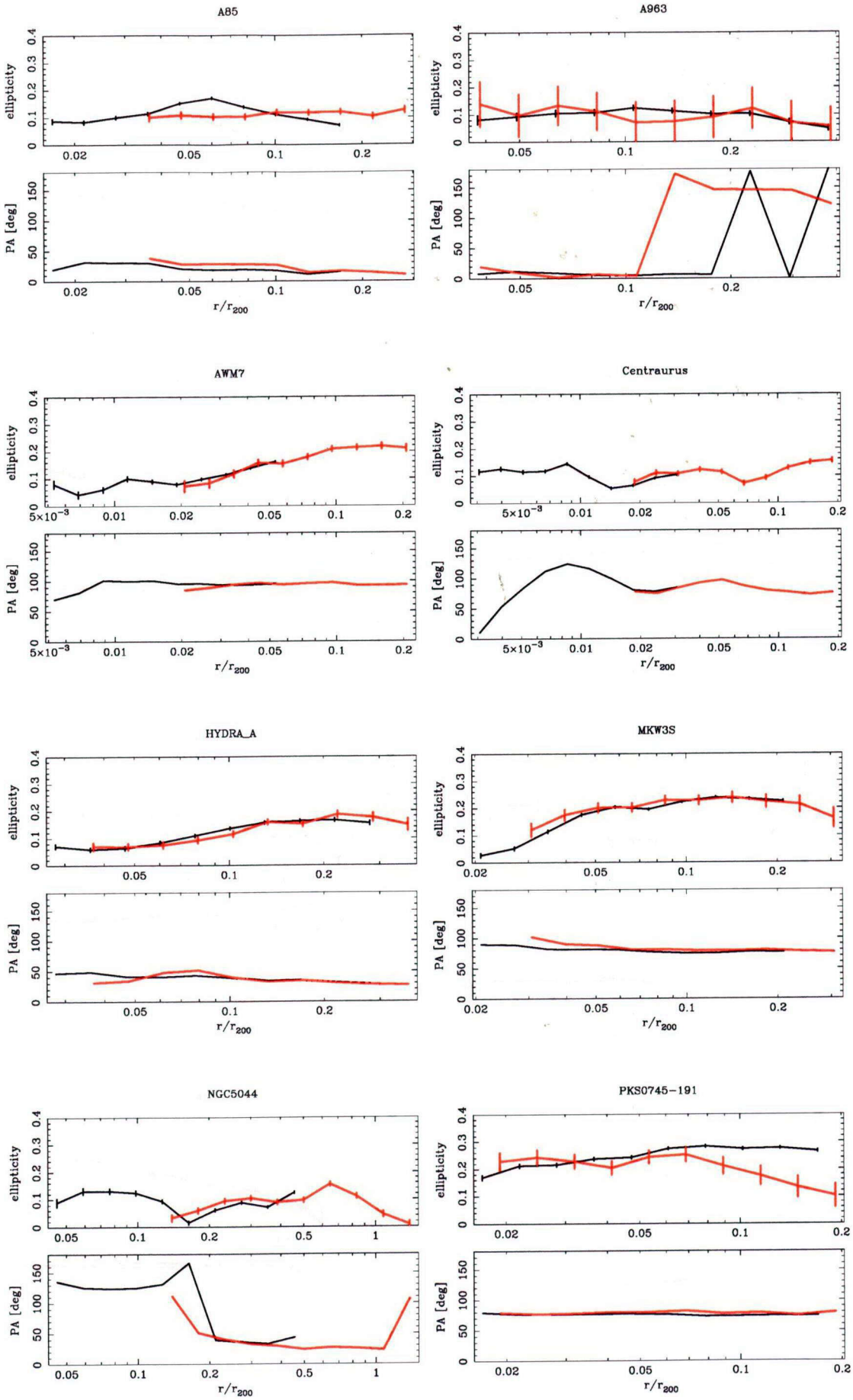
A85
A963
AWM7
Centraurus
HYDRA_A
MKW3S
NGC5044
PKS0745−191
ellipticity
PA [deg]
r/r200

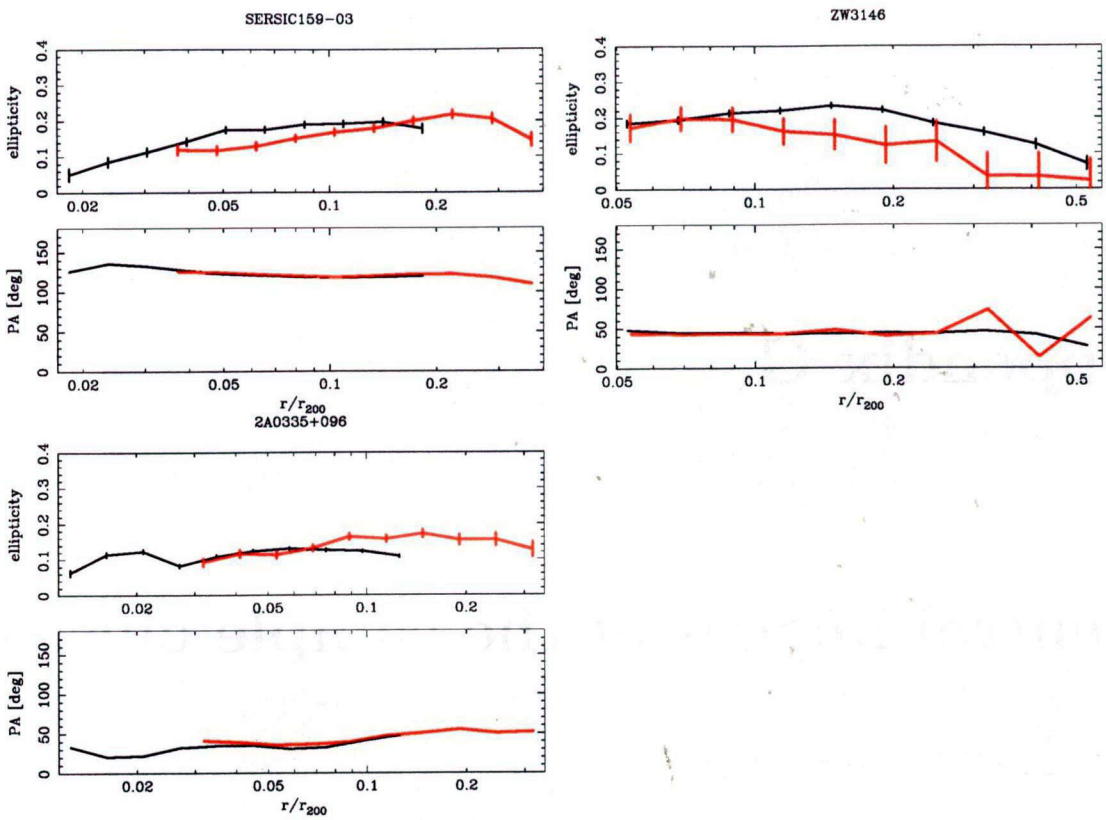
SERSIC159-03
ZW3146
2A0335+096
ellipticity
PA [deg]
r/r200

Appendix G

Central images of the sample clusters

We show the 0.5–7 keV adoptively smoothed *Chandra* images of the 23 sample clusters. The image sizes are $5' \times 5'$. The images are binned with bin size of about $1''$ (2 pixels), and corrected for the exposure. The white solid line represents a scale of 50 kpc. In some clusters (A2597, A401, and A644), the detector structure is not fully removed (see also Appendix A).

A1060 $z = 0.0126$

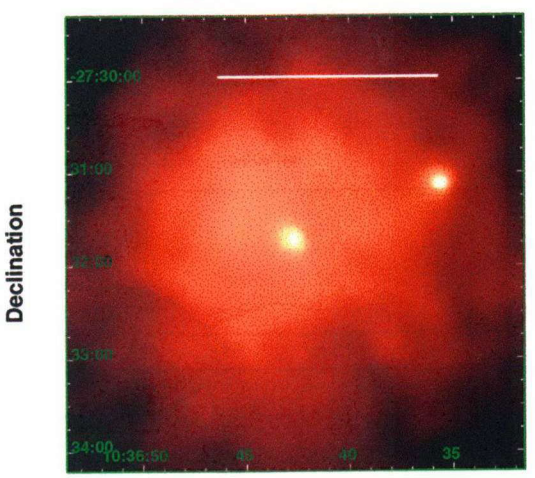

A133 $z = 0.0570$

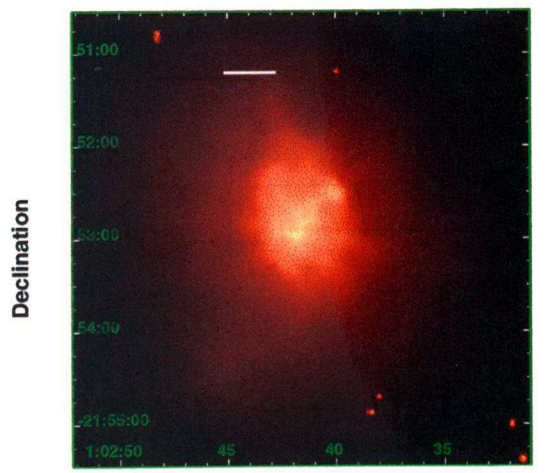

A1795 $z = 0.0622$

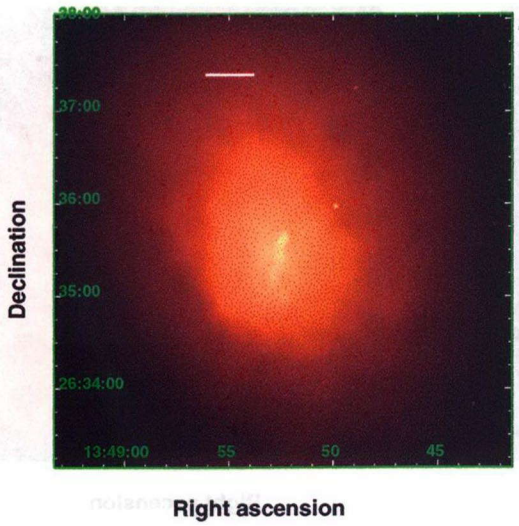

A1835 $z = 0.2530$

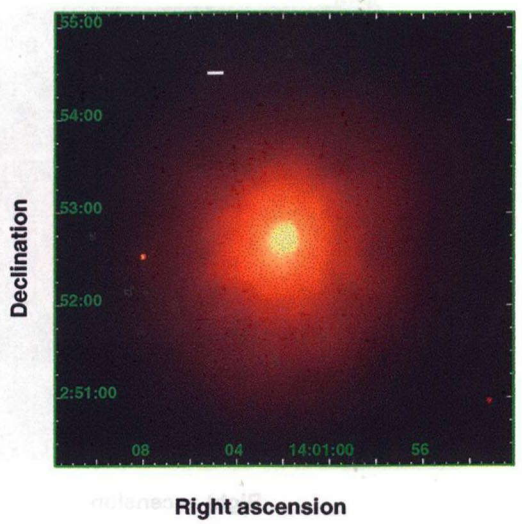

A2029 $z = 0.0780$

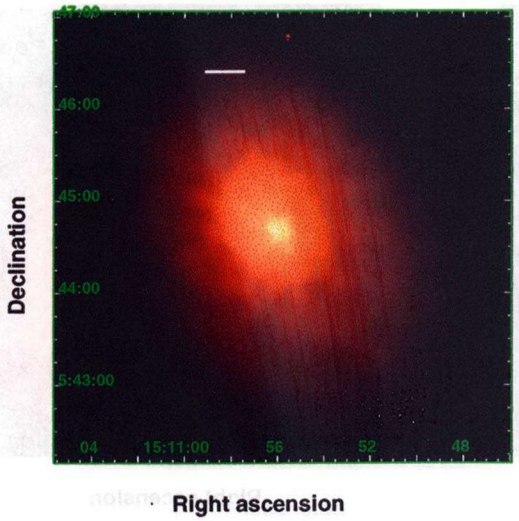

A2052 $z = 0.0345$

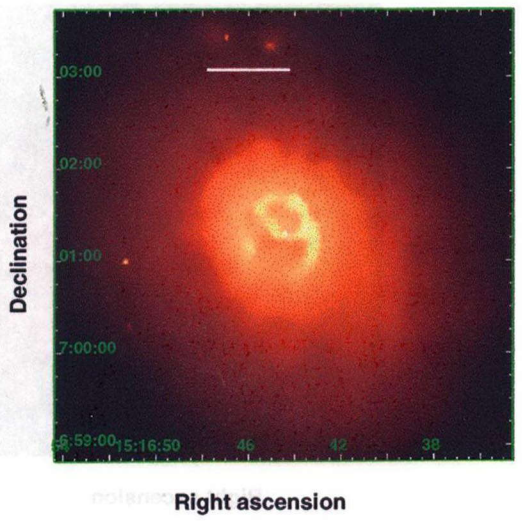

A2199 $z = 0.0310$

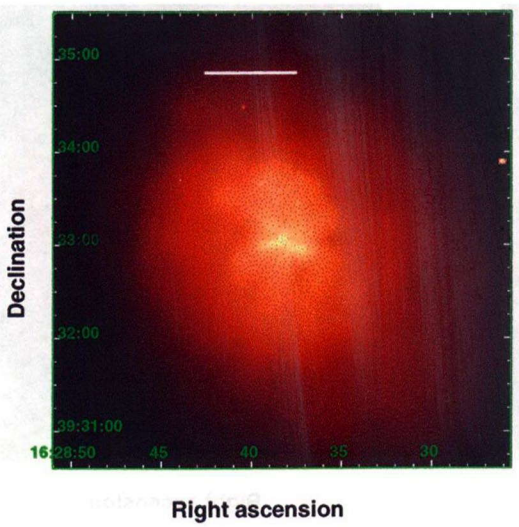

A2204 $z = 0.1511$

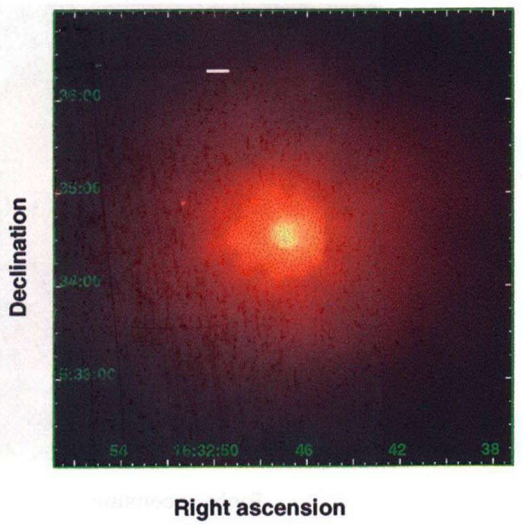

A2597 $z = 0.0822$

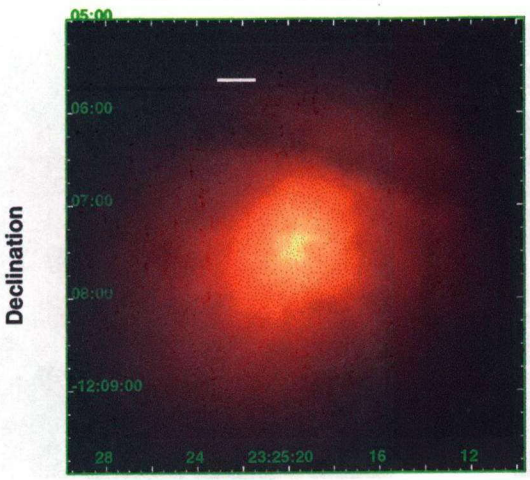

A401 $z = 0.0748$

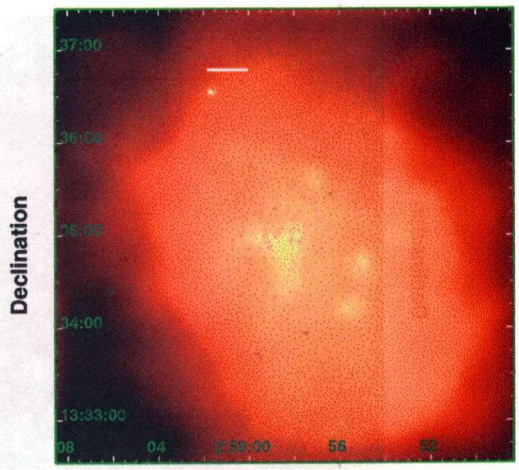

A478 $z = 0.0881$

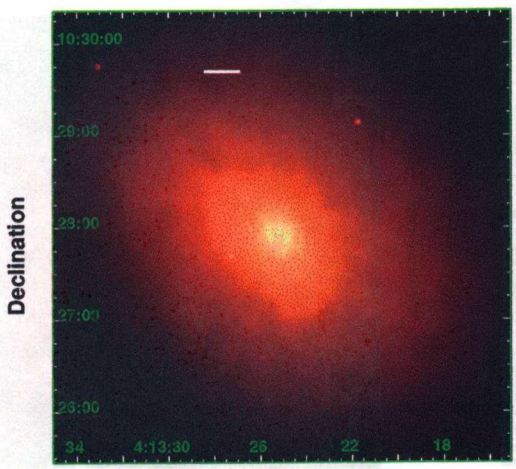

A644 $z = 0.0704$

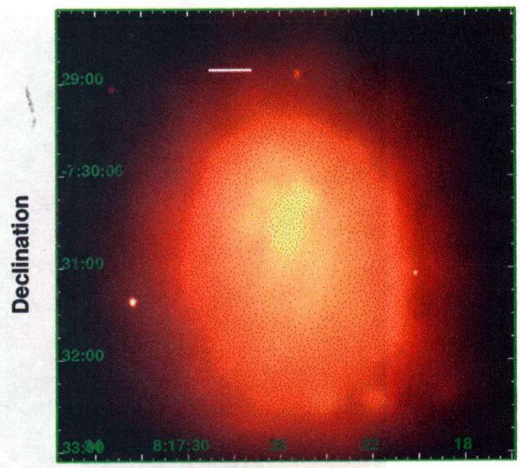

A85 $z = 0.0557$

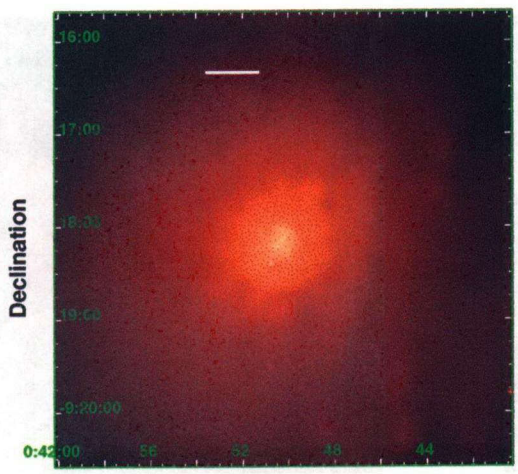

A963 $z = 0.2057$

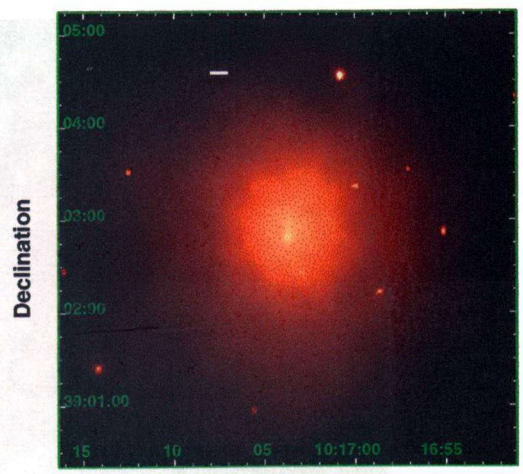

AWM7 $z = 0.0172$

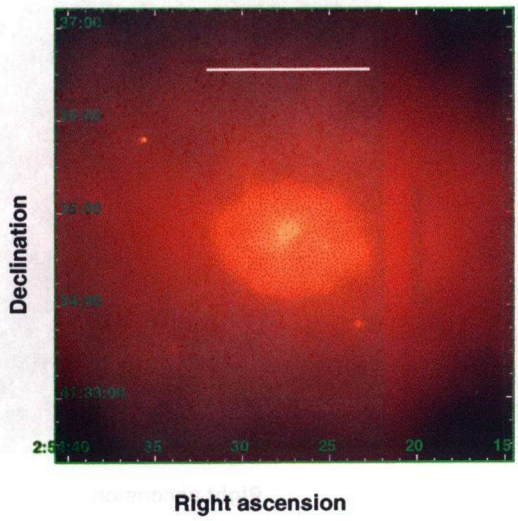

Centaurus cluster $z = 0.0110$

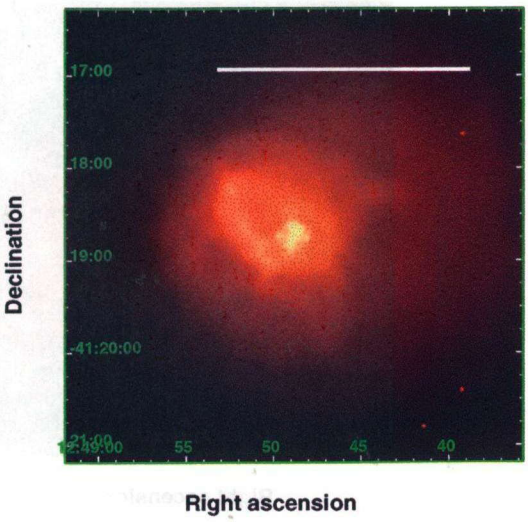

Hydra A $z = 0.0538$

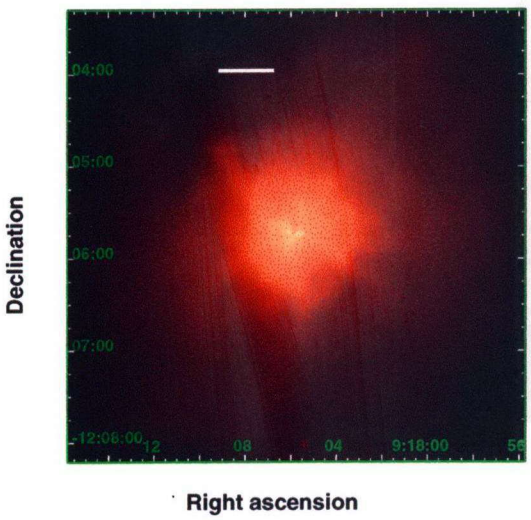

MKW3S $z = 0.0450$

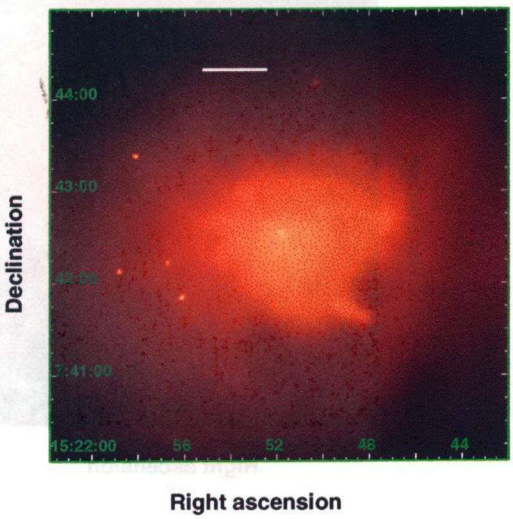

NGC5044 $z = 0.0892$

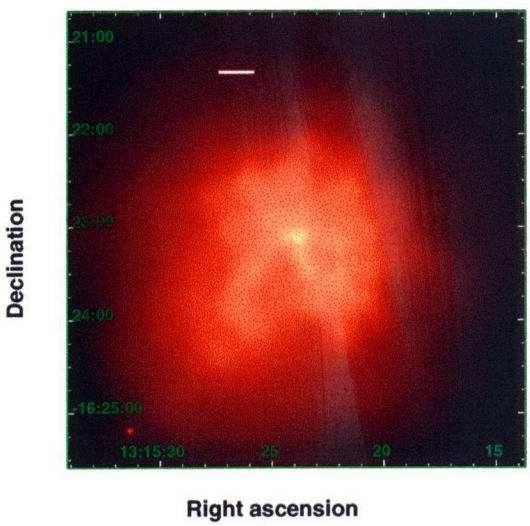

PKS0745-191 $z = 0.1028$

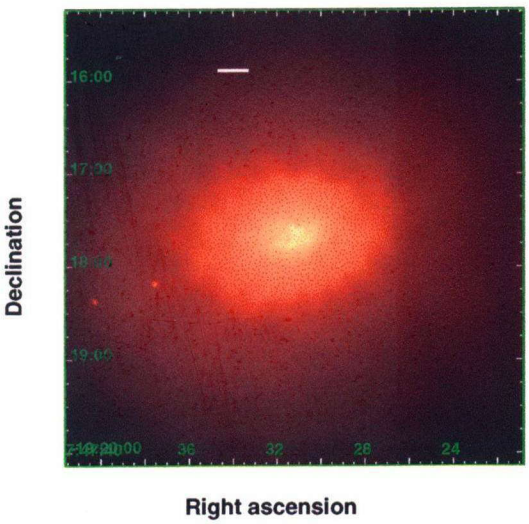

Sersic159-03 $z = 0.0580$

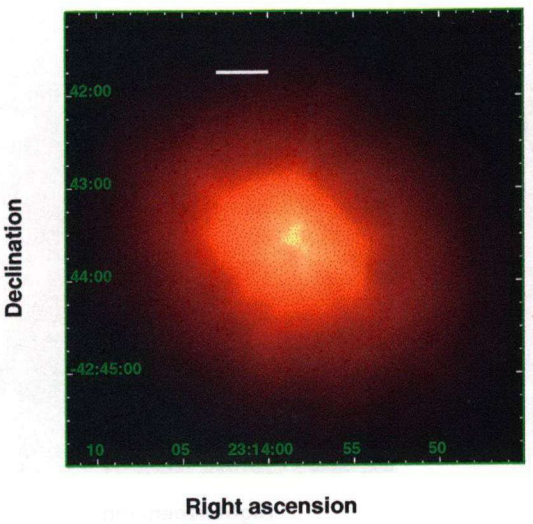

ZW3146 $z = 0.2906$

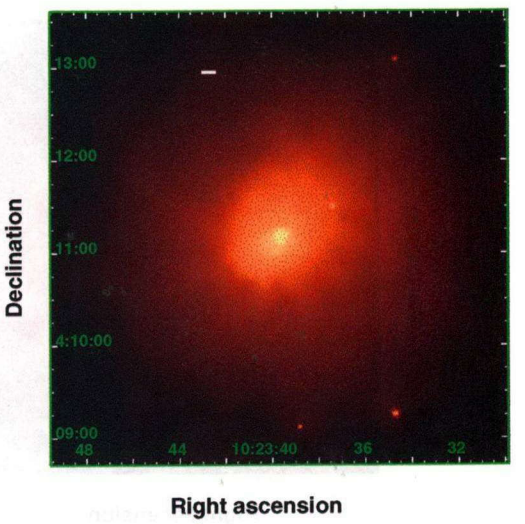

2A0335+096 $z = 0.0349$

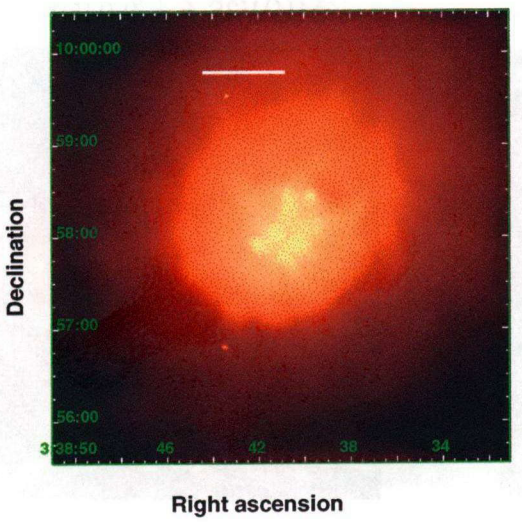

Appendix H

Total mass, gas mass, and gas fraction profiles of the sample clusters

In this appendix, we show the total integrated mass, gas mass, and gas fraction profiles of the 23 sample clusters. The radius is scaled with r_{200}. We show the total integrated mass and gas mass profiles in the upper panel, and the gas fraction profile in lower panel.

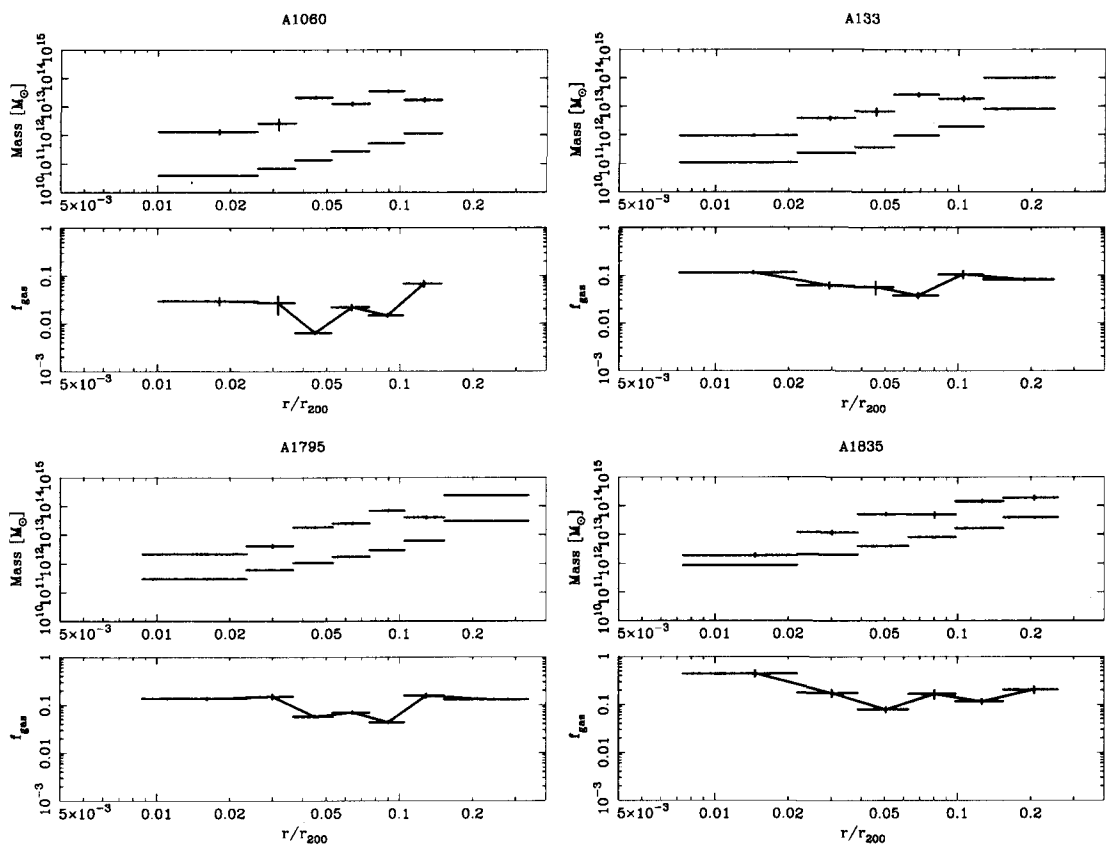

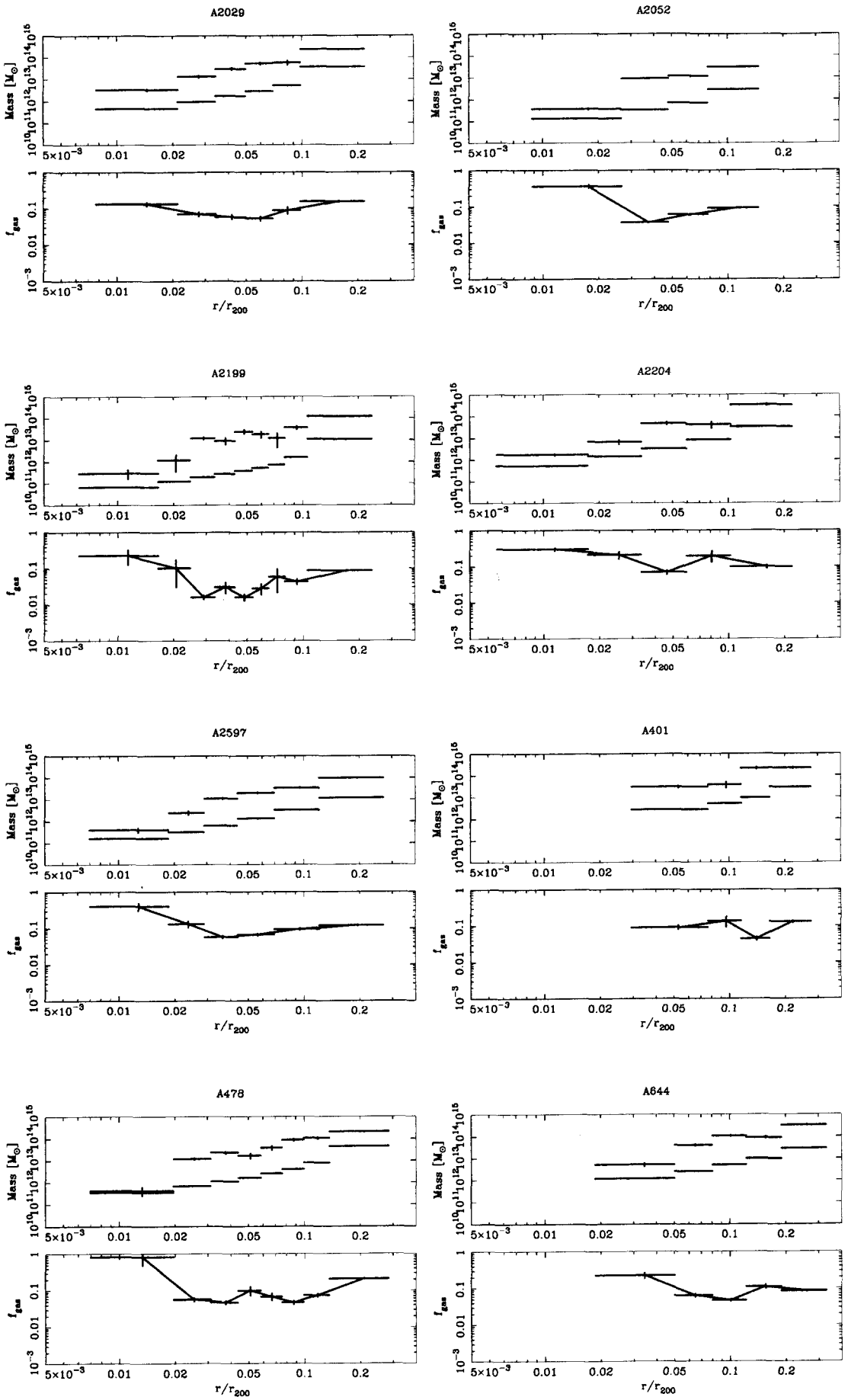
A2029
A2052
A2199
A2204
A2597
A401
A478
A644
Mass [M⊙]
f_gas
r/r_200

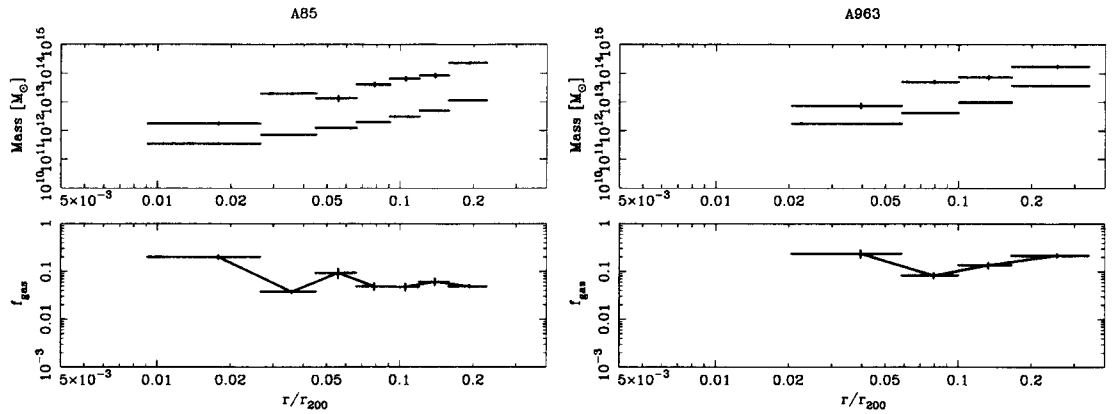
A85
Mass [M⊙]
f_gas
r/r200

A963
Mass [M⊙]
f_gas
r/r200

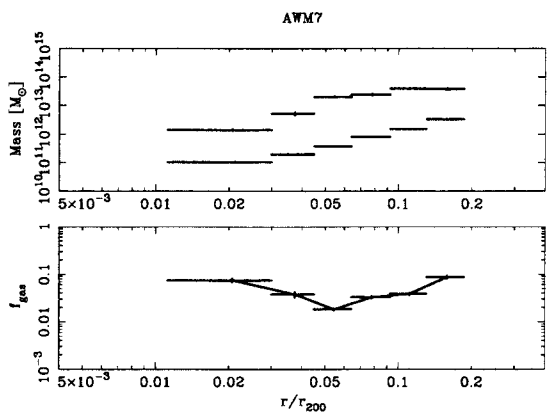
AWM7
Mass [M⊙]
f_gas
r/r200

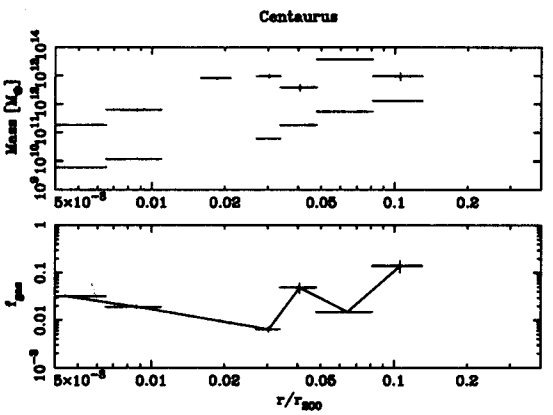
Centaurus
Mass [M⊙]
f_gas
r/r200

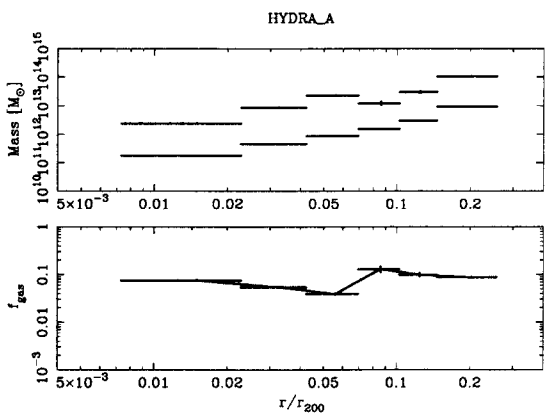
HYDRA_A
Mass [M⊙]
f_gas
r/r200

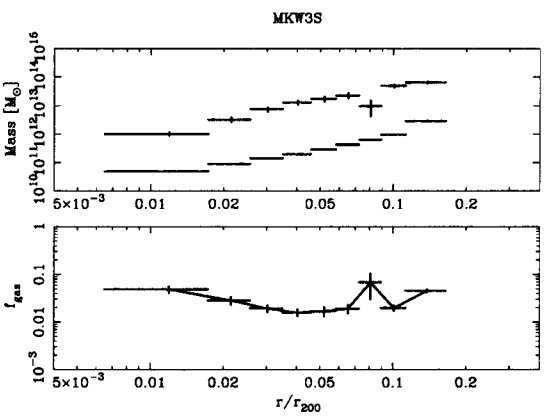
MKW3S
Mass [M⊙]
f_gas
r/r200

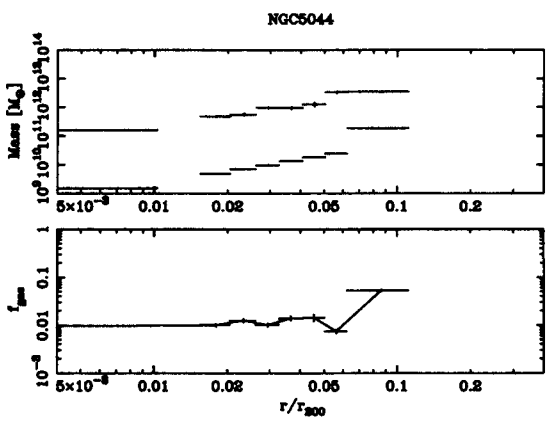
NGC5044
Mass [M⊙]
f_gas
r/r200

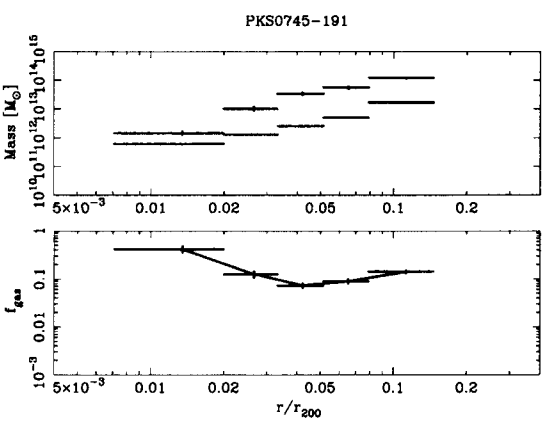
PKS0745-191
Mass [M⊙]
f_gas
r/r200

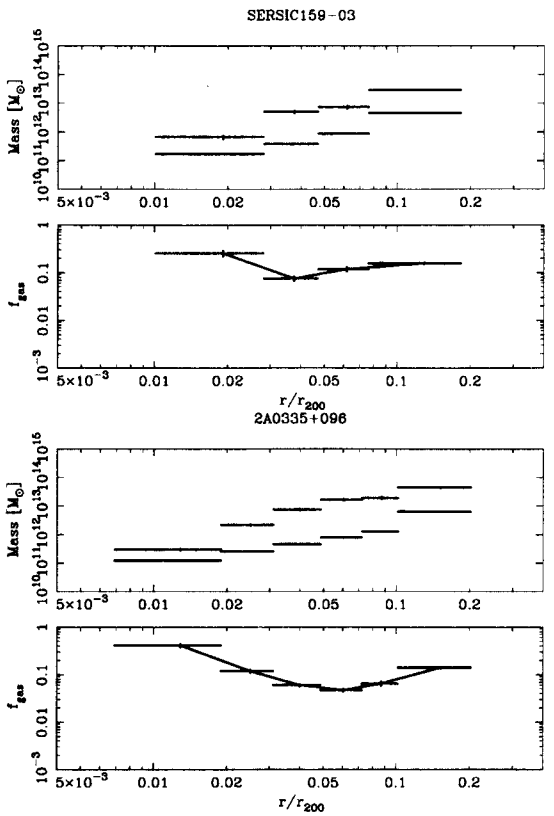
SERSIC159-03
Mass [M⊙]
10^{10} 10^{11} 10^{12} 10^{13} 10^{14} 10^{15}
f_{gas}
1
0.1
0.01
10^{-3}
5×10^{-3} 0.01 0.02 0.05 0.1 0.2
r/r_{200}

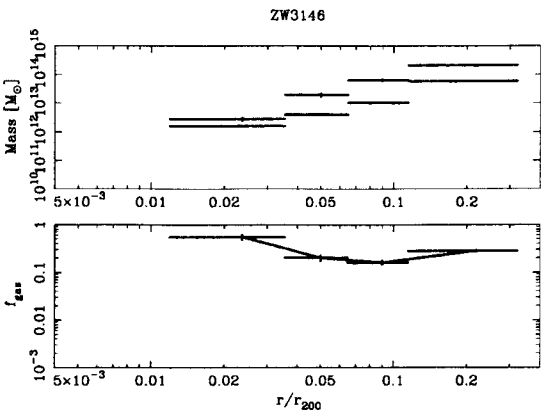
ZW3146
Mass [M⊙]
10^{10} 10^{11} 10^{12} 10^{13} 10^{14} 10^{15}
f_{gas}
1
0.1
0.01
10^{-3}
5×10^{-3} 0.01 0.02 0.05 0.1 0.2
r/r_{200}

2A0335+096
Mass [M⊙]
10^{10} 10^{11} 10^{12} 10^{13} 10^{14} 10^{15}
f_{gas}
1
0.1
0.01
10^{-3}
5×10^{-3} 0.01 0.02 0.05 0.1 0.2
r/r_{200}

Acknowledgments

I am grateful to my supervisor Prof. T. Tsunemi for his support and guidance throughout my graduate school period for five years. I also wish to express my best gratitude to Prof. K. Hayashida. He supported and encouraged me for this thesis. I appreciate Prof. S. Kitamoto and Dr. E. Miyata for their valuable comments on the astrophysics. I am grateful to Prof. T. Ohashi, Prof. F. Takahara, and Prof. H. Kawamura for referees and valuable comments.

I thank Dr. Y. Ikebe, Dr. J. Arabadjis, and Dr. M. Bautz for their support on the deprojection technique and their useful comments. I would like to thank all the staff members involved in the *Chandra* project.

I wish to acknowledge all the members, past and present, of the X-ray astronomy group in Osaka University, particularly to Dr. K. Hashimotodani, Dr. J. Hiraga, Dr. K. Mori, and Dr. T. Kohmura.

This work is supported by JSPS Research Fellowship for Young Scientists.

Finally, I thank my family for their support and encouragement throughout my graduate school life.